國立交通大學
電信工程學系
博士論文

超寬頻及高整合模組應用之縮小化天線

Miniaturized Antennas for Ultra-Wideband and High Integration Module Applications

研 究 生：凌菁偉
Ching-Wei Ling

指導教授：鍾世忠　博士
Dr. Shyh-Jong Chung

中華民國九十七年十一月

超寬頻及高整合模組應用之縮小化天線

Miniaturized Antennas for Ultra-Wideband and High Integration Module Applications

研究生：凌菁偉
指導教授：鍾世忠　博士

Student: Ching-Wei Ling
Advisor: Dr. Shyh-Jong Chung

國立交通大學
電信工程學系
博士論文

A Dissertation
Submitted to Department of Communication Engineering
College of Electrical and Computer Engineering
National Chiao Tung University
in Partial Fulfillment of the Requirements
for the Degree of Doctor of Philosophy
in
Communication Engineering
Hsinchu, Taiwan

2008 年 11 月

摘　要

本論文旨在縮小化天線之研究，包含超寬頻天線以及高整合度模組兩方面的應用。本研究所提出的天線設計，均具備結構簡單、製作與積體化容易、成本低廉，以及良好的阻抗匹配與穩定的輻射場型等特性。

首先，就超寬頻應用方面，本論文提出一種具有二次多項式曲線之單極超寬頻天線設計。利用所提出的二次多項式方程式，並適當地選擇相關變數達成超寬頻天線的設計。此外，為了達成具有頻帶截止的功能，我們採用並聯 LC 電路架構，藉由調整電路中電感與電容值，能得到適當的截止頻率與截止頻寬。由實驗量測結果顯示，具有頻帶截止功能之超寬頻天線，在截止頻帶內之平均天線增益與全頻帶超寬頻天線相比約小 -18 dBi，而截止頻帶外的增益與輻射場型則與全頻帶超寬頻天線相似。

再者，本論文提出一種架構簡單、小型化單極似之印刷式超寬頻天線設計。此天線係由一單極天線支段與一類傳輸線支段所組成，訊號由天線饋入端饋入後，先通過類傳輸線支段後進入單極天線支段。此一類傳輸線支段在不同操作頻段具有不同的功能，不僅能提供阻抗匹配之外，同時也可成為主要的輻射體，進而達成超寬頻的特性。

此外，一具有垂直於水平面的強電場且低側高之超寬頻天線設計，也於本論文中提出與研究。於接地面上內埋兩個 L 形狹縫，不僅能提供額外的共振頻率，更可改善輸入阻抗匹配，進而得到寬頻的天線特性。再者，由於天線饋入端與短路端之電流方向，在操作頻帶下均相同的緣故，因此本天線與其他一般印刷式天線相比，在水平切面上具有更強的垂直電流。至於周圍金屬物體對天線特性的影響，同樣也於本論文中討論，本天線與金屬平面近距離平行擺放時，仍然維持良好的輻射特性，並且天線高度僅為 5mm。

最後，針對高整合模組應用方面，本研究提出一種一體成形並直接製作於電路屏蔽盒上之小型化系統封裝天線設計，其應用頻段為無線區域網路 IEEE

802.11b/g。於本研究中，對於天線與內埋於電路屏蔽盒之射頻元件之間的耦合效應做相關討論，並且也將此系統封裝天線與無線區域網路之前端電路相整合，進行相關電路特性的量測之外，更進一步將此整合後的天線與無線區域網卡上的基頻電路相連接，其量測之 EVM 在操作頻段內均大於-30dB，具備相當良好的特性。同時也可由系統封裝天線之優異輻射特性，再次證實此設計實際應用於無線區域網路通訊之可行性。本天線尺寸僅為 15 mm × 20 mm × 3.5 mm。

Abstract

This dissertation is focused on the miniaturized antenna development for ultra-wideband (UWB) and high integration module applications. These antenna designs have the merits of simple in geometry, easy for manufacture and integration, low-cost, and exhibits a good impedance matching in addition to have stable radiation patterns over the bandwidths.

Firstly, for UWB communication applications, a new binomial curved monopole UWB antenna is introduced. In this study, we propose a new edge curve, characterized by the binomial function and properly choose the parameters of the binomial function, for designing UWB antenna. Besides, to achieve the band notch function with a UWB antenna, the concept of the parallel LC circuit is applied. By adjusting the inductor and capacitor values, the suitable notch frequency and bandwidth can be achieved. The average gain is lower than -18 dBi in the stopband, while the patterns and the gains at frequencies other than in the stopband are similar to that of the antenna without the band-notched function.

Secondly, a simple and compact monopole-like printed ultra-wideband antenna is presented. The antenna is composed of a monopole section and a quasi-transmission line section. The input signal from the feed line first passes through the line section then enters the monopole. The quasi-transmission line section provides different functions as the operating frequency changes. It serves not only as an impedance matching circuit but also a main radiator, which leads to the ultra-wideband performance of the antenna.

Thirdly, a low-profile UWB antenna with strong vertically field has been proposed and investigated. Two L-shaped slits are embedded on the ground plane, which provide additional resonances and improve the input impedance matching thus wideband performance can be obtained. Besides, according to that the current direction on the feed and shorting strip are the same, hence, the proposed antenna has stronger vertical polarization field as compared to the conventional printed antenna in horizontal plane. Moreover, the metal body's effect on the antenna performance also analyzed. The proposed antenna maintains good radiation characteristics while a metal plane is placed parallel under the antenna closely. The proposed antenna has a low-profile of 5 mm.

Finally, a miniaturized antenna design, for the high integration module application has been proposed and demonstrated. This on-package planar inverted-F antenna (PIFA) made from a single folded metal plate and fabricate directly on the shielding package for IEEE 802.11b/g WLAN band applications. In this study, the coupling between the antenna and the RF component embedded inside the package is studied. Moreover, an on-package PIFA integrated with a WLAN front-end module (FEM) and a WLAN card containing the baseband/medium access control (MAC) circuitry is successfully implemented. The Error Vector Magnitude (EVM) in the operating band is better than -30 dB, indicating the good performance of the architecture. From the tested result, it seems that the on-package PIFA has good radiation characteristic and thus suitable for the WLAN communication applications. The prototype has a compact size of 15 mm × 20 mm × 3.5 mm.

致　謝

在博士班的求學過程中，首先要誠摯感謝我的指導教授鍾世忠博士，老師悉心的教導，使我得以熟知天線相關理論與實務領域的深奧，並不時的與我討論、修正研究方向，在我遇到瓶頸困難的時候，給予適當的協助，使得這些年獲益匪淺。並且，老師對於學問的嚴謹以及認真積極的處事態度更是我學習的典範。此外，也要特別感謝我的碩士班指導教授黃智裕博士，因為老師的栽培提攜，給予我鼓勵與信心，讓我能順利的進入交通大學就讀博士班，在此也要表示我內心由衷的感謝之意。至於本論文能得以完成，除感謝兩位恩師之外，亦得感謝陳俊雄教授、許博文教授、郭仁財教授、張志揚教授、陳富強教授以及林根煌教授，由於諸位口試委員給我的建議與評論，使得本論文能更加完善而嚴謹。

博士班四年多的日子裡，實驗室裡共同的生活點滴，不論是學術研究的討論、言不及意的閒聊、出遊玩樂的喜悅、分食食物的瘋狂…等等，都要感謝912的學長、同學、學弟妹們，也因為有你們的陪伴，讓這四年的研究生活變的絢麗多彩。在此特別要感謝的是文信、嘉祐、崇育、諭正給予我研究上相當大的幫助，譚博、侑信、靖凱、智祥不厭其煩的指出我研究上中的缺失，且總能在我迷惑時為我解惑，以及何博、佩宗、清標、肇堂、明達在學業與研究上的互相砥礪，而其他四年來實驗室的所有成員們當然也不能忘記，你們的幫助同樣銘感在心。

在此，也要感謝這四年來陪我一起成長的好姐妹們，珮華、淑君、淳齡、小龍、芝綺，謝謝你們一直都在我身邊，和我一起分享生命中的歡笑與淚水，不斷給我鼓勵與支持，讓我有繼續前進的動力。此外，感謝為我熬夜校稿的又正、連進與世興，因為你們的協助，讓論文文法錯誤少了許多。同時，更要感謝我摯愛的雙親，不只默默地支持我，任何時候也都會做我最溫暖而堅強的後盾，讓我能無後顧之憂的全心研究，進而完成博士班的學業。

最後，謹以此文獻給所有關心我與我關心的人！

Contents

List of Tables

List of Figures

Chapter 1 Introduction

Nowadays, with the rapid development of the wireless communications, mobile communication devices become more compact size and light weight. Due to the size reduction requirement, the antenna design trend to miniaturization and high integration module application for the space restriction. Hence, this dissertation focuses on the miniaturized antenna development for ultra-wideband (UWB) and high integration module applications. This chapter firstly describes the motivation of the research and discusses the related antenna design literatures. The contributions of this dissertation are presented next. Lastly, the outline of the following chapters is provided.

1.1 Motivation

The antenna is a key component for all wireless communication systems. With the rapid development of the wireless communications, many systems now operate in two or more frequency bands, requiring dual-band or multi-band functioned antennas. These systems include GSM (880-960 MHz), DCS (1700-1880 MHz), UMTS (1920-2170 MHz), WiBro (2300-2390 MHz), WLAN (2400-2483 MHz, 5150-5825 MHz), and combinations of them. The conventional antennas which are specified for a rather narrow bandwidth are insufficient for use. The ultra-wideband (UWB) antennas, which are usually designed to use single antenna structure with broadband operation, become attractive for the benefits of simpler structure than multi-band designs with several narrow-banded elements. Here, the UWB antennas mean those with a relative impedance bandwidth larger than 25% [1]. Besides, according to the regulations released by Federal Communications Commission (FCC) in February 2002, one of the

UWB systems has been allocated to the frequency band of 3.1 to 10.6 GHz [2] for the merits of high transmission rate, high capacity, and low power consumption. Thus, there is a growing demand on antenna design for a simple and compact structure with wideband operation, both for the integration usage of multi-mode multi-frequency systems and for an UWB system.

The UWB systems can be divided into two categories: Direct Sequence UWB (DS-UWB) and Multi-Band Orthogonal Frequency Division Multiplexing (MB-OFDM). The DS-UWB proposed that UWB system supports operation in two different bands: one band nominally occupying the spectrum from 3.1 to 4.85 GHz (the low band), and the second band nominally occupying the spectrum from 6.2 to 9.7 GHz (the high band). By the MB-OFDM format in 802.15.3a, the interval between 3.1 and 10.6 GHz is divided into 13 sub-intervals. Each sub-interval corresponds to one band of the MB-OFDM, with the width of 528 MHz. The MB-OFDM proposal foresees two different operating modes: a mandatory Mode 1 and an optional Mode 2. Mode 1 uses three operating bands: Band 1 (3.168-3.696 GHz), Band 2 (3.696-4.224 GHz), and Band 3 (4.224-4.752 GHz). Mode 2 uses seven bands: Band 1, 2, 3 (as in Mode 1), Band 6 (6.072-6.60 GHz), Band 7 (6.60-7.128 GHz), Band 8 (7.128-7.656 GHz), and Band 9 (7.656-8.184 GHz). The four unmentioned bands, i.e. Bands 10-13 (8.184-10.296 GHz), have been reserved for future use [3]-[4]. Therefore, there is a sparked attention on UWB antenna technology in the industry and academia for commercial use. And more and more researchers get involve in developing UWB antennas which satisfy the regulations. Besides, using the lower band operation can provide long-distance transmission and non-line of sight (NLOS) propagation is used for deliver broadband data to a wide range of users. Hence, much research is focus on the DS low band design.

However, despite the approval of the FCC for UWB to operate over 3.1 to 10.6 GHz, it may be necessary to notch-out portions of the band in order to avoid interference with the existing wireless networking technologies such as IEEE 802.11a in the U.S. (5.15-5.35 GHz, 5.725-5.825 GHz) and HIPERLAN/2 in Europe (5.15-5.35 GHz, 5.47-5.725 GHz). This is due to the fact that UWB transmitters should not cause any electromagnetic interference to nearby communication system like the Wireless Local Area Network (WLAN) applications. Hence, UWB antennas design with notched characteristics in the WLAN frequency band are required.

Besides, the other miniaturized antenna design for WLAN System-on-Package (SOP) application is investigated. WLAN has been one of the most important applications of wireless communication technology in recent years. The WLAN standards have been developed by the Institute of Electrical and Electronics Engineers (IEEE) and the 802.11 standard is a family of specifications for WLAN technology. For instance, WLAN in the 2.4 GHz band (2.40-2.4835 GHz) of IEEE 802.11b/g has been developed widely and rapidly applied by using wireless communication terminals, such as desktop computers, laptop computers, mobile phones, personal digital assistants (PDAs), etc. Nowadays, SOP technology is one solution for establishing future wireless transceiver modules that can provide flexibility by integrating all functional blocks using the multi-layer process and novel interconnection methods. To enhance the function of SOP for wireless communications, it has become very attractive to develop the SOP which is efficiently to integrate an antenna with a module. Therefore, the antenna in SOP is a significant subject for investigation and thus our motivation is to design the antenna for high integration module application.

Furthermore, the antenna performance is affected by the operating environment, especially when metal bodies are nearby the antenna. In the practical using environment, the antenna might be placed parallel above a metal body such as metal-like table, PC case or placed near the LCD screen edges, inserted inside a laptop, and so on. Figure 1.1 shows a practical environment of a PCMCIA (Personal Computer Memory Card International Association) card (within a PIFA or monopole antenna) inserts inside a laptop. The simulated E-field distribution around the laptop is shown in Figure 1.2. In this case, when the antenna is operating, fringing fields are expected to be present externally; thus, coupling between the antenna and the nearby associated elements (e.g., a metal-like table under the antenna) will occur. This possible coupling will then cause degradation effects on the antenna performances. Moreover, the EM wave radiated from the antenna will induce currents on the metal bodies, which in turn will radiate back to the antenna and thus deteriorate the antenna function. With different height and position of the antenna above the metal bodies, the image current can procure constructed or destructed radiation, according to the phase relationship between antenna current and image current induced on the metal object. Thus the performance of the antenna will be quite different depending on the placement relative to the metal body. Hence, the study on the antenna behavior when near a metal body is an important and necessary research issue.

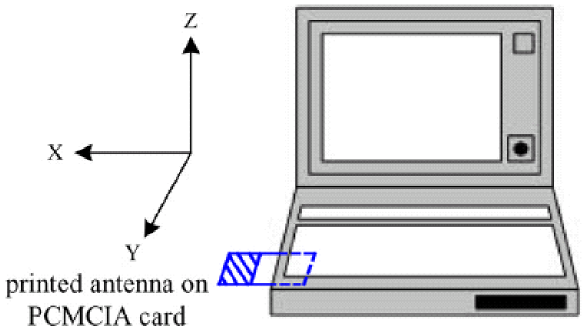

Figure 1.1 Illustration of the printed antenna on a PCMCIA card inserted inside a laptop PC for WLAN application.

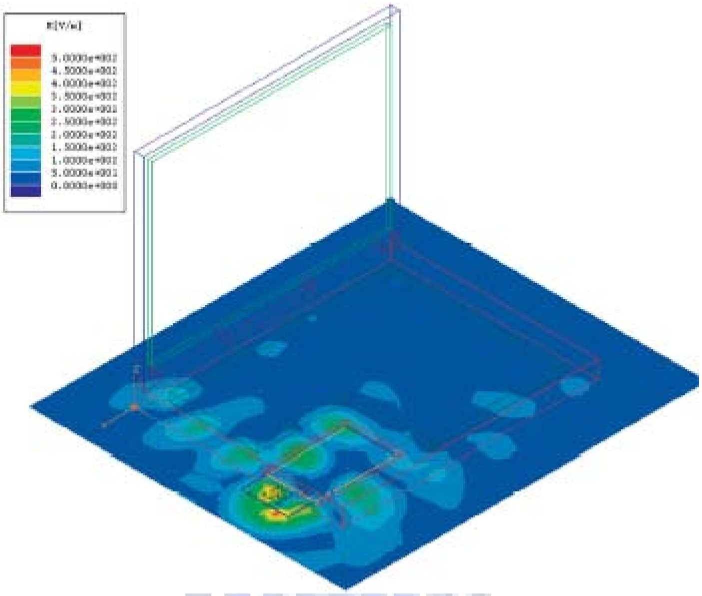

Figure 1.2 HFSS simulated E-field distribution around the laptop PC housing.

Moreover, the typical transmitting antenna type of the Access Point (AP) antenna might have a monopole antenna structure, which has a strong vertical polarization field. If the receiving antenna is of printed type and has strong horizontal polarization field. That will cause deterioration in quality communication while there’s different polarization between the transmitter and receiver antenna. Although increasing the antenna height can improve the vertical polarization field but the height is restricted to the practical use environment and the device size. Hence, designing a low-profile UWB antenna with high vertical polarization field is also an investigation necessary.

In summary, a series of miniaturized antenna designs were proposed. For the UWB communication applications, there are four antenna designs. First of all, an internal UWB antenna design for PCMCIA card is presented. Then, a miniature UWB antenna with small size for external applications is also introduced. Finally, a simple structure and a low-profile UWB antenna designs were proposed. In addition, another miniaturized antenna design for the high integration module applications, and an on-package PIFA fabricate directly on the shielding package which can further reduce the device size, had been investigated in this dissertation.

1.2 Literature Survey

According to there is a growing demand on antenna design for a brief structure with wideband operation. There are many researches in the open literature related to achieving the wideband performance. In [5]-[8], using parasitic elements as shown in Figure 1.3 (a), for providing additional current paths, can create more resonant frequencies adjacent to the center one and thus get the wideband operation. Modifying the shape of the feed line is another method for enhancing the bandwidth. It was demonstrated that, applying double or triple feeds to the main antenna structure (as Figure 1.3 (b)) can generate a pure and intense current distribution, leading to the improvements in the polarization properties and impedance bandwidth [9]-[12].

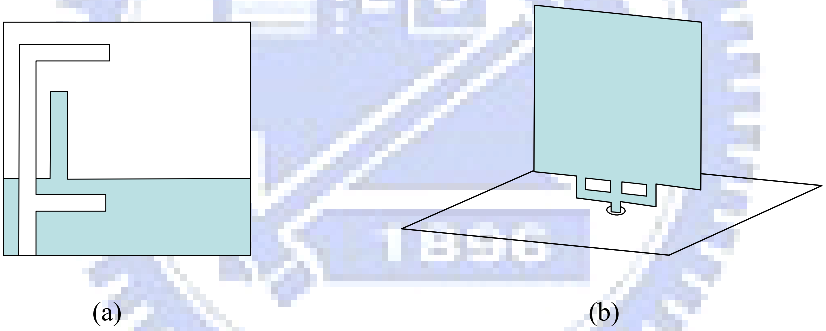
(a) (b)

Figure 1.3 Wideband antenna structure. (a) Use the parasitic element, (b) use the triple feed.

Besides, the UWB antennas proposed in the open literature mainly focus on the monopole and slot antenna. The wideband planar monopole antenna is one of UWB antennas that have attracted a lot of attention because it is simple in geometry, easy for manufacture and integration, and low-cost, and exhibits not only a good impedance matching but also stable radiation patterns over the bandwidths. There are many related studies to the type of antenna having been available in the open literature and most researches focus on the planar design antenna such as half-disc [13]-[14], circular [15]-[17], elliptical [18], triangle [19]-[21], rectangular [22]-[25], bow-tie [26]-[28], hexagonal [29]-[30], and others with smooth edges [31]-[35], which provide the possible shapes of antennas suitable for UWB application. Most of them were designed with printed “fat” monopole structure to achieve UWB performance. There is usually a small gap between the fat monopole and the ground plane edge as shown in Figure 1.4, which is an important factor for impedance matching, especially in the high frequency range. For these antennas, in the lower operation frequency band, the current is mainly distributed over the monopole and the nearby ground plane edge, which is similar to the current of a resonant monopole. In the higher frequency band, the current is distributed around the gap, therefore, acting like a slot antenna. Due to these appropriate current paths across the full band provided by the antenna structure, the wideband operation is thus achieved.

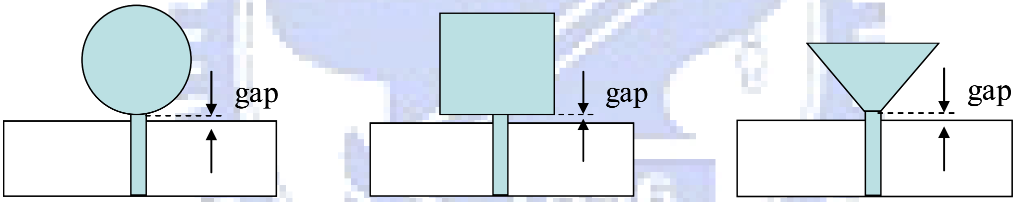

Figure 1.4 Geometry of the typical UWB antenna.

The other one, printed wide slot antennas has an attractive property of providing a wide operating bandwidth, especially for those having a modified tuning stub, such as the fork-like stub [36]-[39], the rectangular stub [40]-[41], and the circular stub [42] inside the wide slot as shown in Figure 1.5. Moreover, there is some research results related to using the ceramic material or Low Temperature Co-fired Ceramic (LTCC) technology, according to that its high dielectric constant material reduces the antenna size and achieves the UWB applications [43]-[45].

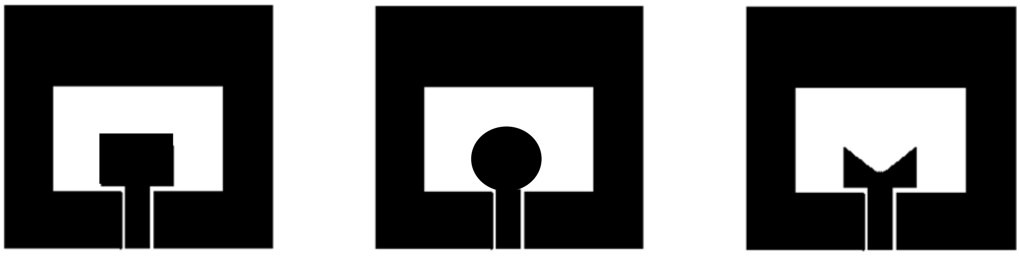

(a) (b) (c)

Figure 1.5 Geometry of the typical wide slot UWB antennas with (a) rectangular feed, (b) circular feed, and (c) fork feed.

The frequency range for UWB systems approved by the FCC is between 3.1 GHz and 10.6 GHz. It might cause interference with the existing wireless communication systems, for example, the WLAN operating in 5.15-5.85 GHz. Therefore, the UWB antenna with a band-notched characteristic is required. To obtain the band-notched function, there are various methods to achieve it. The conventional methods are cutting a slot (i.e., U-shaped, V-shaped, arc-shaped, and a pie-shaped slot) on the patch [46]-[54], inserting a slit on the patch [55]-[57], embedding a quarter-wavelength tuning stub within a large slot on the patch [58], or using the split ring resonator (SRR) structure on the patch [59]-[60]. Another way is putting parasitic elements near the printed monopole as filters to reject the limited band [61]-[63] or introducing a parasitic open-circuit element, rather than modifying the structure of the antenna's tuning stub [64]. Changing the feed structure is also a method to achieve the band-notched response such as using the lumped and distributed inductors and capacitors integrated on the top side of the substrate in front of the feed port [65] and inserting two quarter-wavelength tuning stubs or a resonance cell into the proposed feeding [66]-[67]. As mentioned above, at the notch frequency, the current mainly concentrates over the area of the cutting slot, the adding stub and parasitic element, thus, achieving the band notch function.

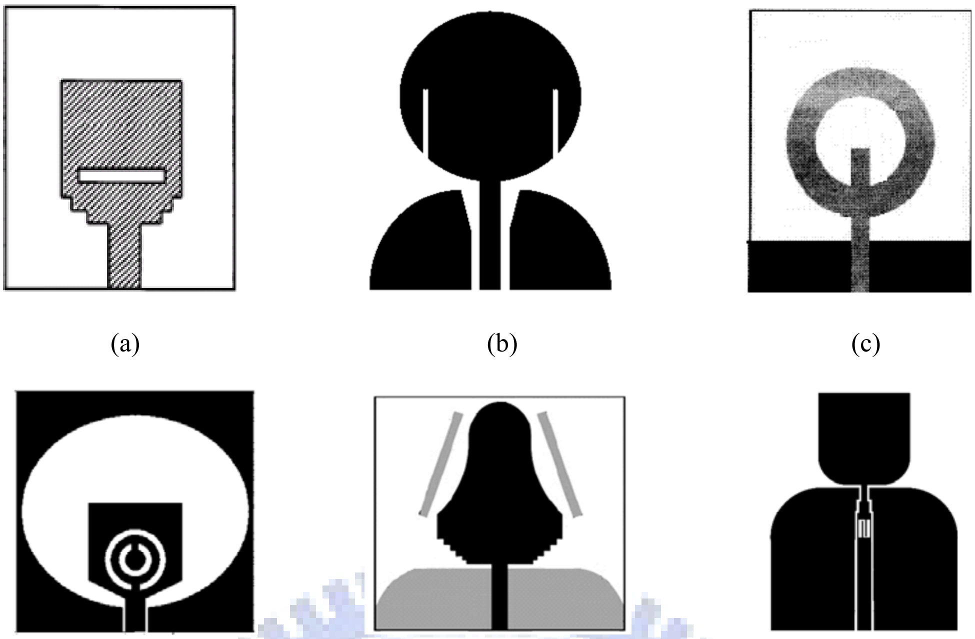

(a) (b) (c)

(d) (e) (f)

Figure 1.6 Geometry of the band notch UWB antenna design. (a) Cut a slot, (b) insert a slit, (c) embed a quarter-wavelength tuning stub, (d) use the SRR, (e) put a parasitic element, and (f) modify the feed line structure.

As regards the miniaturized antenna design for WLAN application, recently many conventional antennas have been successfully designed for WLAN applications, such as monopole antennas, PIFAs, patch antennas, and dielectric resonator antennas (DRA) [71]-[77]. For the kinds of the printed monopole antenna, the antenna is usually directly excited by a 50Ω microstrip line printed on the same (upper) side of the dielectric substrate [71]-[73]. This kind of internal antenna mainly uses the system ground plane as the antenna’s ground. The system ground-plane dimensions, to some extent, can strongly affect the antenna impedance bandwidth. And the other kind of DRA is attracted the attention of antenna researchers because of its wide impedance bandwidth and flexible coupling schemes [74]. Another kind of antenna design is PIFA that provides several merits of compact size, light weight and low cost [75]-[77]. For establishing future wireless transceiver modules provide flexibility by integrating all functional blocks using the multi-layer process and novel interconnection methods, SOP technology is one solution. Many single-chip wireless transceivers have been designed, such as those fabricated in 0.25 μm at 1.8 GHz for DCS-1800 applications and at 2.45 GHz for Bluetooth applications [78]. To enhance the function of SOP for wireless communications, it has become very attractive to develop the SOP which integrates an antenna with a module efficiently. In the case that the embedded antennas are integrated with the low temperature co-fired ceramic (LTCC) package, semiconductor substrates, or the ceramic ball grid array package (CBGA), interferences between the antenna and the RF blocks may happen in highly integrated modules [79]-[85]. Usually the patch antenna is employed and stacked on the top above the circuit within the package. The configuration leads to an increase in the overall height of the package and results in narrow-band operation as well. In addition, due to the use of high permittivity dielectric material, the radiation efficiency of the antenna is also limited.

Besides, the antenna performance is affected by the operating environment, especially when metal bodies are nearby the antenna. The EM wave radiated from the antenna will induce currents on the metal bodies, which in turn will radiate back to the antenna and thus deteriorate the antenna function. This possible coupling will then cause degradation effects on the antenna performances. But, there are only few references concerned to the operating environment affecting the antenna characteristics, especially when metal bodies are nearby or under the antenna [68]-[70].

1.3 Contributions

A series of miniaturized antenna designs for UWB and high integration module applications have been established in this dissertation.

First, for the UWB application, although the typical shapes of the UWB monopole antenna include a half-disc, a circle, an ellipse, a rectangle, and others with smooth edges are published in the open literature as described above. But there are only few references concerned to the edge curve affecting the antenna characteristics. In this dissertation, we present a new method to construct the edge curve of the antenna and analyze parametric effects on the impedance bandwidth. Formulating the curves of the antenna edge by a binomial function, the impedance bandwidths of the proposed antenna can significantly be improved if the parameters of the binomial function are properly selected.

To obtain the band-notched function in the UWB antenna application, then, different approach of the continental design, the concept of the parallel LC circuit is applied. At the resonant frequency, the parallel LC circuit will cause high input impedance that leads to the desired high attenuation and impedance mismatching near the notch frequency. Hence, a pair of T-shaped stubs is embedded inside an elliptical slot cut in the radiation patch to form the parallel LC circuit. The elliptical slot and the T-shaped stubs are equivalent to an inductor and a capacitor, respectively. By adjusting the inductor and capacitor values, the suitable notch frequency and bandwidth can be achieved.

Beside, a new antenna configuration which is different from the printed fat monopoles is proposed for the ultra-wideband operation. The structure is quite simple, containing a conventional printed thin-wire monopole, in addition to a quasi-transmission line section. The input signal from the feed line first passes through the quasi-transmission line section then enters the monopole. The quasi-transmission line section provides impedance matching or antenna radiation at different frequency bands. By properly designing the parameters of this quasi-transmission line section, several current resonances with continuous frequencies can happen in the antenna structure, which thus makes the whole antenna possess wideband performance.

Moreover, in the practical environment, there will cause deteriorate quality of communication while the different polarization propagation between the transmitter and receiver antenna. Hence, in this study, a low-profile DS-UWB antenna with strong vertical polarization field is proposed. According to embedded two L-shaped slits on the ground plane, which provide additional resonances and improve the input impedance matching thus wideband performance can be obtained. Besides, because of the loop structure, the current direction on the feed and the shorting strip are the same, hence, the proposed antenna has stronger vertical polarization field as compared to the conventional printed antenna in the horizontal plane and then maintains good radiation characteristics even while a metal plane is placed parallel under the antenna closely. The antenna has a low profile of 5 mm.

Finally, for high integration module application, an on-package PIFA, consisting of a single folded metal plate for WLAN applications, is proposed. Fabricating an antenna directly on the package has the advantage of reducing feeder loss and the overall size of the circuitry. The shielding package can perform as part of the ground plane and block to eliminate the undesired coupling with nearby RF components and the coupling effect between the on-package PIFA and the RF components in the shielding package is examined. The antenna performance is rarely changed and the isolation between the antenna and the RF components can be maximized by appropriately locating the components in the package. Moreover, an on-package PIFA integrated with a WLAN front-end module and a WLAN card was successfully implemented. The prototype has a compact size of 15 mm × 20 mm × 3.5 mm.

1.4 Outline of the Dissertation

This dissertation is organized as follows. Chapter 2 presents two planar UWB antennas design, and at first, a binomial curved monopole antenna is introduced. We propose a new edge curve characterized by the binomial function, for designing UWB antenna. The effect on the impedance bandwidth through the change with the different order of the binomial function and the gap width between the antenna and ground plane has been investigated and analyzed. Then, a novel planar UWB antenna with band-notched function is proposed. The concept of the parallel LC circuit is applied. The notched band, covering the 5-GHz WiFi band, is achieved by an equivalent parallel LC circuit formed by two T-shaped stubs inside an ellipse slot cut in the radiation patch. The elliptical slot and the T-shaped stubs are equivalent to an inductor and a capacitor, respectively. By adjusting the inductor and capacitor values, the suitable notch frequency and bandwidth can be achieved.

In Chapter 3, a simple and compact monopole-like printed ultra-wideband antenna is presented. The antenna is composed of a monopole section and a quasi-transmission line section. The input signal from the feed line first passes through the line section then enters the monopole. The resonance mechanisms of the proposed ultra-wideband antenna are firstly described. Four antenna resonances with different resonant conditions are examined. The effect of the quasi-transmission line section on the antenna performance is then investigated. Moreover, an equivalent model is proposed to explain the behavior of the line section in the lower frequency band. The geometry parameter study on the impedance bandwidth is done next, followed by the presentation of measured return loss and radiation patterns.

In Chapter 4, a low-profile ultra-wide band antenna with strong vertical polarization field is proposed. The antenna design, including the embedded L-shaped slits mechanisms of the proposed UWB antenna and the simulated current distributions of the proposed antenna, is first described. Besides, in the practical using environment, the performance of the antenna will be quite different depending on the placement relative to the metal bodies. Hence, the effect on the antenna performance on the metal object will be investigated and a conventional printed UWB antenna is also simulated for comparison. Lastly, the measured return loss and radiation patterns of the proposed antenna are presented.

In Chapter 5, an on-package PIFA made from a single folded metal plate for IEEE 802.11b/g WLAN band applications has been proposed and demonstrated. This antenna is fabricating directly on the shielding package. First, to demonstrate the on-package antenna, several design parameters, such as the package dimensions and ground size, have been analyzed in detail. Secondly, the coupling between the antenna and the RF component embedded inside the package is studied. Next, an on-package PIFA integrated with a WLAN front-end module and a WLAN card was successfully implemented. Finally, the antenna embedded front-end module (AFEM) is first built and measured.

Finally, Chapter 6 concludes the overall dissertation and also provides suggestions for the future works.

Chapter 2 Planar Ultra-wideband Antennas

In this chapter, two planar UWB antennas design are presented. Firstly, by introducing the binomial function for characterized the edge curve of the antenna. Through the change with the different order of the binomial function and the gap width between the antenna and ground plane, the UWB (3.1-10.6 GHz) antenna can be achieved. Secondly, in order to obtain the band-notched function in the UWB antenna application, then, the concept of the parallel LC circuit is applied and proposed. By properly adjust the inductor and capacitor values, the notched band, covering the 5 GHz WiFi band, is obtained.

2.1 Planar Binomial Curved Monopole Antenna for Ultra-Wideband Communication

The curve of a planar antenna edge is an important parameter which affects the antenna performances. As mentioned in Chapter 1, there are many related studies to the type of antenna having been available in the open literature and most researches focus on the planar design antenna such as half-disc [13]-[14], circular [15]-[17], elliptical [18], triangle [19]-[21], rectangular [22]-[25], bow-tie [26]-[28], hexagonal [29]-[30], and others with smooth edges [31]-[35], which provide the possible shapes of antennas suitable for UWB application.

In this section, we propose a new edge curve, characterized by the binomial function, for designing ultra-wideband (UWB) antenna. The effect on the impedance bandwidth through the change with the different order of the binomial function and the gap width between the antenna and ground plane has been investigated and analyzed. The measurement result shows a good agreement with the simulation. Besides, the radiation patterns are omnidirectional in the H plane across the operating bandwidths.

2.1.1 Antenna Configuration

Figure 2.1 illustrates the geometry of the investigated antenna. This antenna is printed on a FR4 microwave substrate with the thickness of 0.8mm and the dielectric constant of 4.4. The areas of the monopole antenna and the ground plane are denoted as $w \times \ell$ and $W \times L$, respectively. A 50 Ω microstrip feed line of 1.5 mm width is etched on the same side of the monopole. The gap width between the monopole antenna and the ground plane is G. Hence, the whole substrate size of the antenna is $W \times (\ell + G + L)$.

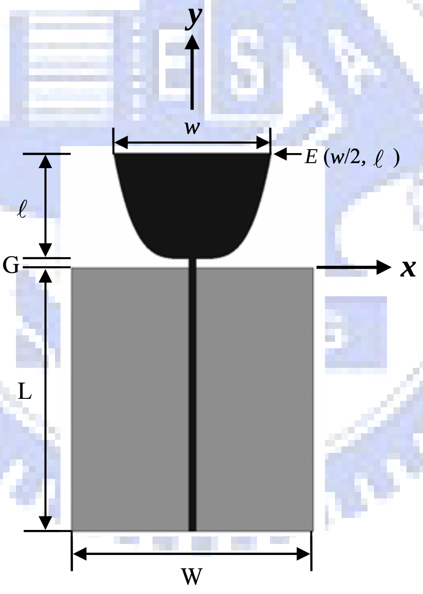

Figure 2.1 Geometry of the planar binomial curved monopole antenna.

The curve of a planar antenna edge is an important parameter which affects the antenna characteristics. The parametric effects on the impedance bandwidth of the proposed antenna are analyzed by utilizing a binomial function. The function includes parameters of the length ℓ and width w of the antenna, the gap width G between the antenna and the ground plane, and the order N of the binomial function, which is expressed as follows:

$$y = f(x) = G + \ell\left(\frac{x}{w/2}\right)^{N}, 0 \le x \le \frac{w}{2} \qquad (2.1)$$

where (x, y) is the coordinate of the curved boundary. In this study, the vertex point E $(w/2, \ell)$ is fixed, with w = 30 mm and ℓ = 20 mm. By selecting the different order N and the gap width G, we can obtain the half shape of the antenna and then mirror along with y axis to obtain the whole antenna configuration.

The antenna shape is like a triangle with N = 1 as shown in Figure 2.2(a). When N approaches infinite, the shape of the antenna looks like a rectangle. Figure 2.2 shows the antenna configurations for G = 0 mm with different order N from 1 to 6.

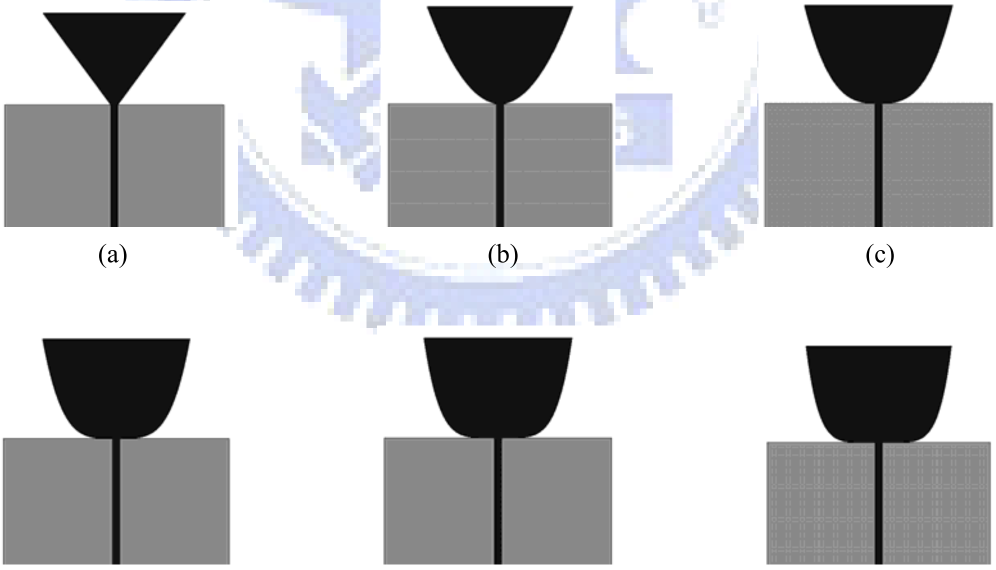
(a) (b) (c)

(d) (e) (f)

Figure 2.2 Antenna forms for G = 0 mm with different order N. (a) N = 1, (b) N = 2, (c) N = 3, (d) N = 4, (e) N = 5, (f) N = 6.

2.1.2 Parameter Analysis

In this section, the effects with respect to parameters N and G of the binomial function on impedance bandwidth are discussed. The simulation results shown below are tackled by using the commercial 3-D full-wave electromagnetic (EM) simulation software package, Ansoft High Frequency Structure Simulator (HFSS) [90].

Figure 2.3 shows the simulated return losses of the proposed antenna for $G = 0.45$ mm with different binomial order N. The relationship between the order N and return loss is not obvious, but by selecting the order N properly, it can be observed that the proposed antenna can cover the frequency band 2.65-10.4 GHz for the case of $N = 4$.

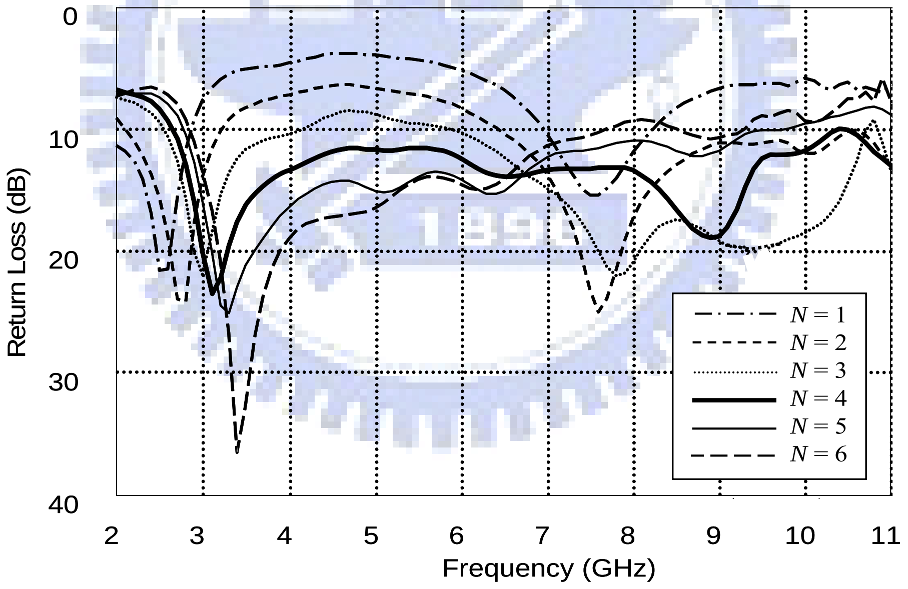

Figure 2.3 Simulated return losses for proposed antenna with different order N, $w = 30$ mm, $\ell = 20$ mm, $W = 46$ mm, $L = 50$ mm, and $G = 0.45$mm.

Furthermore, it should also be noted that the gap width G between the antenna and the ground plane has important effect on the impedance bandwidth of the proposed antenna as shown in Figure 2.4. When $N = 4$, the impedance bandwidth of the proposed design can further be improved by selecting G. The bandwidth increases if $G > 0.3$ mm. In particular, the widest 10 dB return-loss bandwidth, from 2.7 GHz to more than 11 GHz, occurs when $G = 0.45$ mm and $N = 4$.

The simulated current distributions for the proposed antenna at the frequencies 3, 5, and 8 GHz are shown in Figure 2.5. At 3 GHz, the current is mainly distributed over the monopole and the upper edge of ground plane, which is similar to the current of a printed resonant monopole. At 8 GHz, the current is mainly distributed around the gap between the monopole and the ground, therefore, its behavior acts like a slot antenna. By comparing with Figure 2.4, it is clear that, the effect of the high-frequency performance through the change with different gap width G is more remarkable than that of the low-frequency.

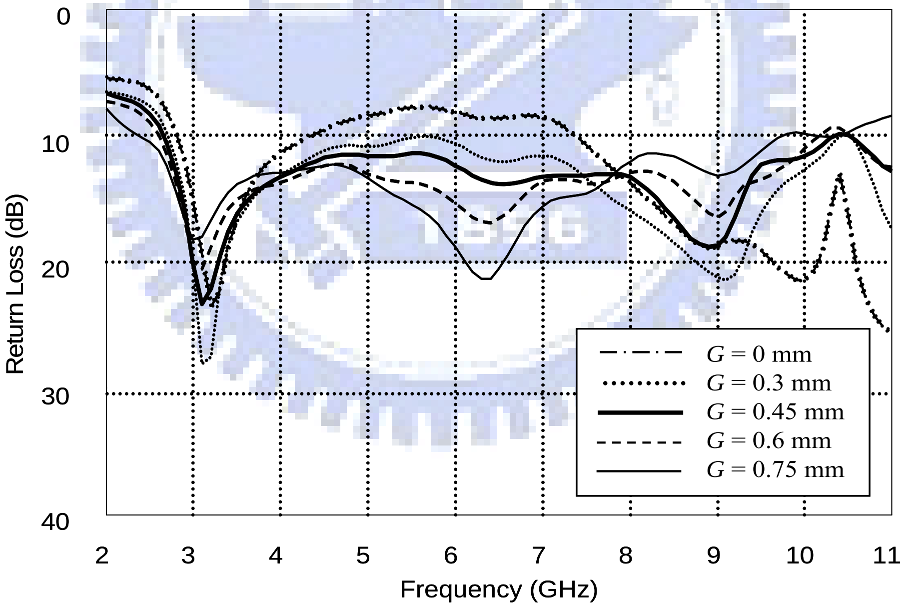

Figure 2.4 Simulated return losses for antenna A with different gap width G, w = 30 mm, ℓ = 20 mm, W = 46 mm, L = 50 mm, and N = 4.

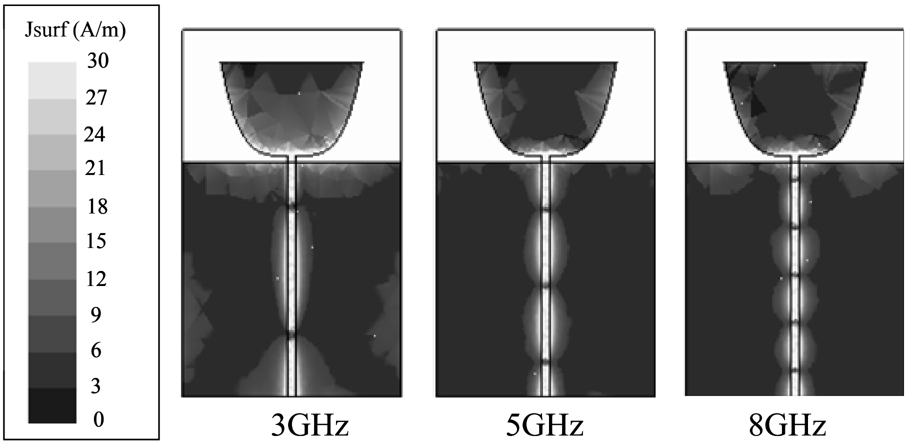

3GHz 5GHz 8GHz

Figure 2.5 Simulated current distributions for the proposed antenna with $w = 30$ mm, $\ell = 20$ mm, $W =$ 46 mm, $L = 50$ mm, $G = 0.45$ mm, and $N = 4$.

2.1.3 Experiment Results

Figure 2.6 shows the measured return loss of the proposed antenna for $N = 4$ and $G = 0.45$ mm. The simulation results are also shown for comparison. A good agreement between the measurement and the simulation results is obtained. The measured impedance bandwidth, determined by a 10 dB return loss, is from 2.59 to 10.97 GHz.

The measured radiation patterns of the proposed antenna at the frequencies 3.1, 5.0, and 8.0 GHz in x-z plane are shown in Figure 2.7(a), (b), and (c), respectively. The radiation pattern is omnidirectional and quite stable over the whole frequency band. The measured peak (average) gains for the frequencies of 3.1, 5.0, and 8.0 GHz are, respectively, -0.88 dBi (-3.65 dBi), -2.36 dBi (-4.51 dBi), and 1.54 dBi (-2.1 dBi). Figure 2.8 shows the photograph of the finished antenna.

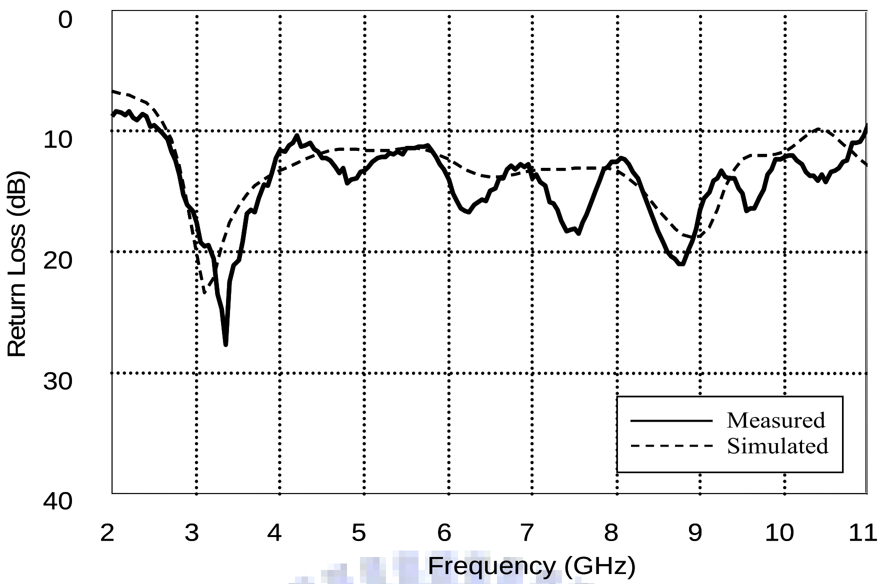

Figure 2.6 Measured and simulated return losses for proposed antenna with w = 30 mm, ℓ = 20 mm, W = 46 mm, L = 50 mm, G = 0.45 mm, and N = 4.

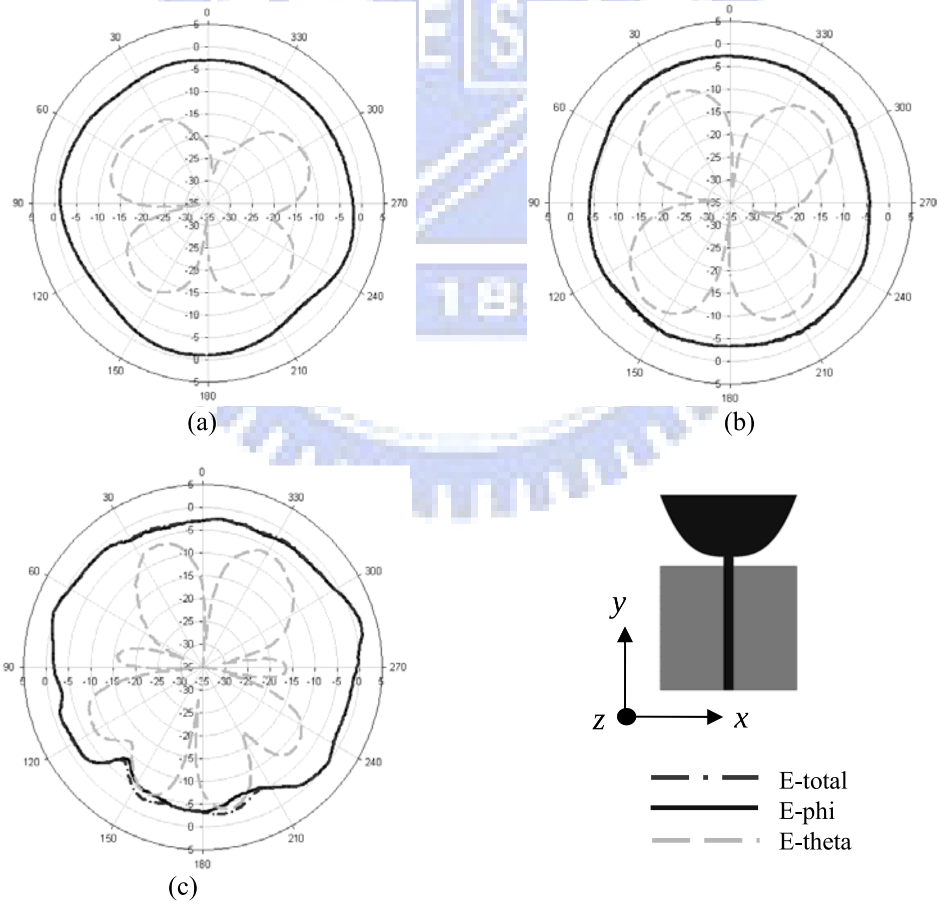
(a)
(b)
(c)

Figure 2.7 Measured x-z plane radiation patterns at (a) 3.1 GHz, (b) 5.0 GHz and (c) 8.0 GHz for the proposed antenna with w = 30 mm, ℓ = 20 mm, W = 46 mm, L = 50 mm, G = 0.45 mm, and N = 4.

Figure 2.8 Photograph of the proposed antenna.

2.1.4 Summary

The planar binomial curved monopole antenna has been proposed and investigated. The antenna has a simple structure and can be designed by utilizing only few parameters. The experiment results show that the impedance bandwidth of the proposed antenna can significantly be improved by selecting the suitable binomial order *N* and the gap width *G*. Also show that a wide impedance bandwidth has been obtained, which makes the proposed antenna suitable for UWB (3.1-10.6 GHz) applications. A stable omnidirectional radiation pattern was also obtained for the whole impedance bandwidth.

2.2 Planar Ultra-wideband Antenna with a New Band-Notch Structure

This section proposes a novel planar UWB antenna with band-notched function. The antenna consists of a radiation patch that has an arc-shaped edge and a partially modified ground plane. The antenna that makes it different from the traditional monopole antenna is the modification in the shape of ground plane, including two bevel slots on the upper edge and two semicircle slots on the bottom edge of the ground plane. These slots improve the input impedance bandwidth and the high frequency radiation performance. With this design, the return loss is lower than 10 dB in 3.1-10.6 GHz frequency range and the radiation pattern is highly similar to the monopole antenna. By embedding a pair of T-shaped stubs inside an elliptical slot cut in the radiation patch, a notch around 5.5 GHz WLAN band is obtained. The average gain is lower than -18 dBi in the stopband, while the patterns and the gains at frequencies other than in the stopband are similar to that of the antenna without the band-notched function.

2.2.1 Antenna Configuration

Figure 2.9 shows the geometry of the proposed antenna. It consists of a radiation patch with an arc-shaped edge and a partially modified ground plane with two bevels to achieve a broad bandwidth. The arc-shaped edge of the radiation patch is a half-ellipse with the major axis of 8 mm and the axial ratio of 1.5. The lengths and width of the straight-edges of the radiation patch are L_a and W, respectively. The bevels with dimensions of $W_s \times L_s$ are placed on the upper side of the ground plane. Additionally, the antenna performance in the high frequency band can be further improved by cutting two semicircle slots on the bottom side of the ground plane. The two semicircle slots have the same radii of r and are placed W_e away from the side edge of the ground plane. The gap between radiation patch and ground plane is denoted as g. A 50Ω microstrip line of 1.5 mm width is connected to the radiation patch as the feed line. Moreover, an elliptical slot cut in the radiation patch with a pair of T-shaped stubs embedded inside produces a notched band in the vicinity of 5.5 GHz and thus prevents the interference with the WLAN system. The antenna is printed on both the top (the radiation patch and microstrip line) and back-side (the ground plane) of a FR4 substrate with thickness of 0.8 mm, relative permittivity of 4.4, and loss tangent of 0.02. The total antenna size is 24 mm × 35 mm.

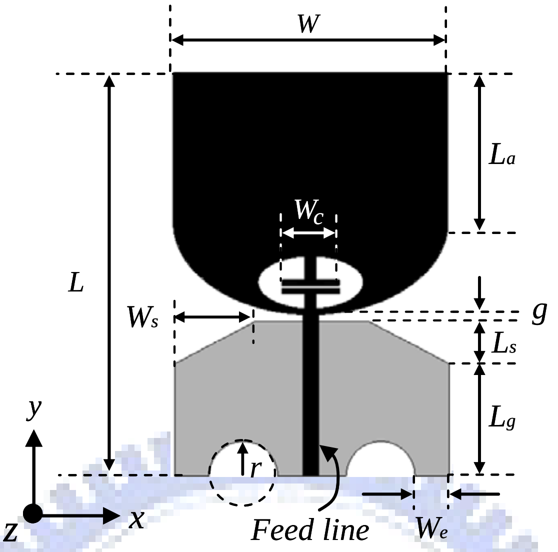

Figure 2.9 Geometry of the proposed antenna. $W \times L$ = 24 mm × 35 mm, L_a = 13 mm, g = 0.6 mm, L_g = 9.7, $W_s \times L_s$ = 7 mm × 3.7 mm, W_c = 3.6 mm, W_e = 3 mm, r = 3 mm.

2.2.2 Antenna Design

In this section, the antenna covering the full UWB band (3.1-10.6 GHz) is first described. Then, the new band-notched structure, which is equivalent to a parallel LC circuit, is investigated. The effects with respect to the geometric parameters of the proposed antenna on impedance bandwidth and radiation pattern are discussed. The proposed antenna structure is simulated using the HFSS.

A. Full band UWB Antenna Design

At low frequencies, the current is mainly distributed over the radiation patch and the ground plane, which is similar to the current of a printed finite-ground monopole antenna. Thus, increasing the patch length L_a is equal to increasing equivalent current length and decreasing the resonant frequency. Figure 2.10 shows the simulated return losses for L_a varied from 7 to 13 mm. It can be seen that the edge of low frequency decrease as L_a increase. When L_a varies from 7 to 13 mm, the low frequency edge moves from 3.25 to 2.75 GHz.

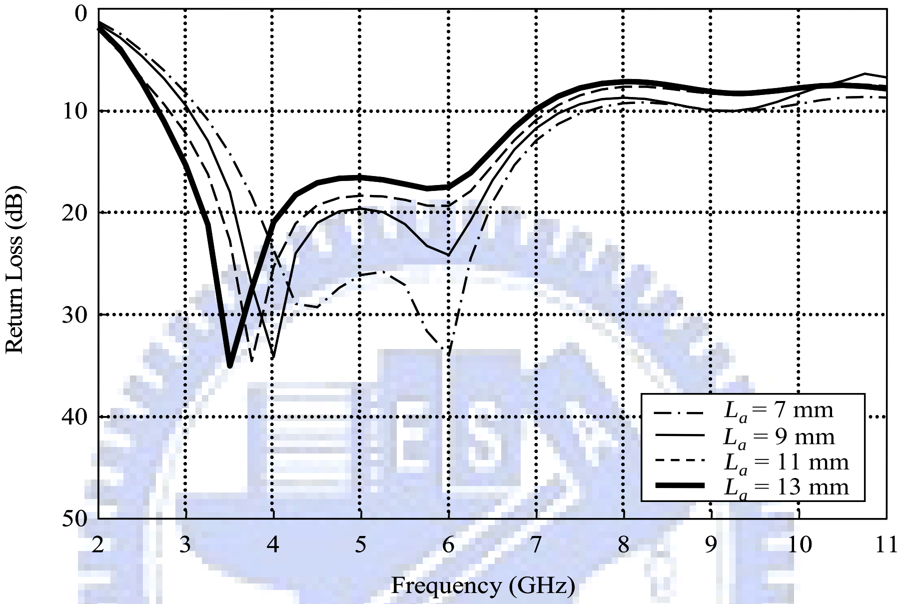

Figure 2.10 Simulated return losses for the proposed antenna with various patch length L_a. $W_s = L_s = W_c = W_e = r = 0$ mm. Other geometric parameters are the same as given in Figure 2.9.

The ground plane of the proposed antenna is also a part of the antenna. The current distribution on the ground plane affects the characteristics of the antenna. The monopole antenna as well as the ground plane forms an equivalent dipole antenna. Figure 2.11 shows the effects of varying the ground plane length L_g (L_g = 7.4, 9.4, 11.4, and 13.4 mm) on the simulated return losses, with L_a = 13 mm. In Figure 2.11, the edge of low frequency decreases as L_g increases, the behavior is similar to changing L_a. When L_g varies from 7.4 to 13.4 mm, the edge of low frequency moves from 3.5 to 2.75 GHz.

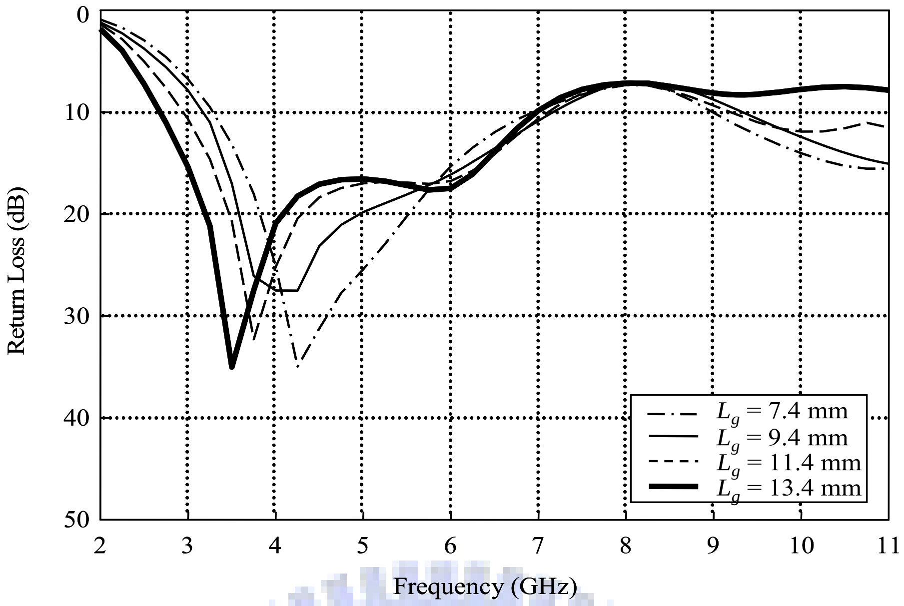

Figure 2.11 Simulated return losses for the proposed antenna with various ground plane length L_g. Other geometric parameters are the same as given in Figure 2.9.

The gap between the radiation patch and the ground plane has an important effect on the impedance matching of the proposed antenna, as shown in Figure 2.12. When the gap g is increasing from 0 to 0.6 mm, the impedance matching at low frequencies can be greatly improved, at the expense of little deterioration in high frequency matching.

By comparing Figure 2.10 to Figure 2.12, it is found that L_a, L_g, and g are principally relevant to the low frequency characteristics, but not the high frequency performance. The reason is that in the low frequency band, the proposed antenna acts like as a printed monopole (or dipole) antenna, while in the high frequency band, the antenna behavior is like a slot antenna. Hence, properly designing the shape of the two bevels between the patch and ground plane will enhance the slot mode radiation and improve the impedance matching in high frequency band.

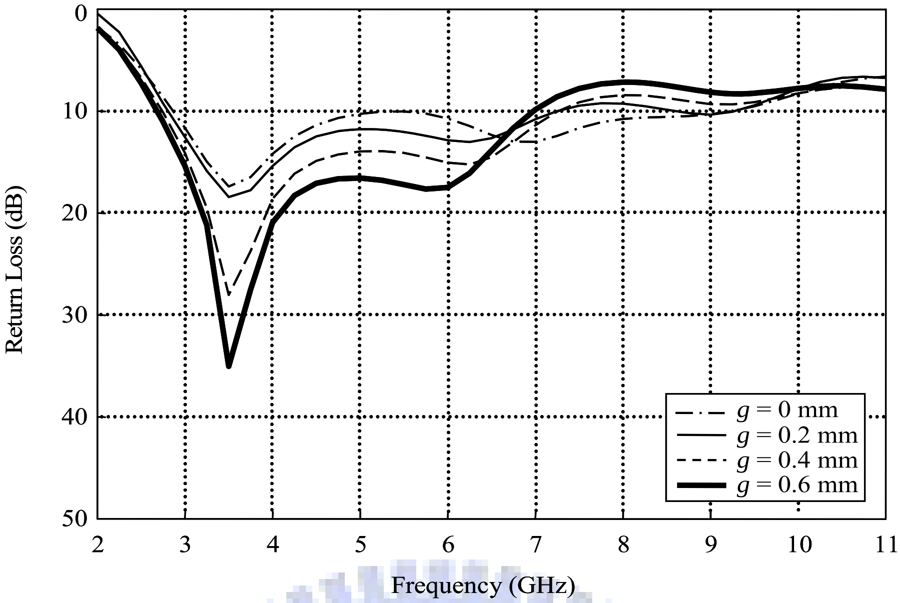

Figure 2.12 Simulated return losses for the proposed antenna with various gap *g*. Other geometric parameters are the same as given in Figure 2.9.

Figure 2.13 and Figure 2.14 show the simulated return losses for various bevel sizes of the ground plane. It is clearly seen that changing W_s or L_s is an efficient way to improving the input impedance matching, especially at the high frequency. For the case of the bevel size $W_s = L_s = 0$ mm, which means no bevel on the ground plane, the bandwidth is not sufficient. Properly choose W_s and L_s, a widest bandwidth can be obtained. From the simulated results in Figure 2.13 and Figure 2.14, it occurs when $W_s = 7$ mm and $L_s = 3.7$ mm.

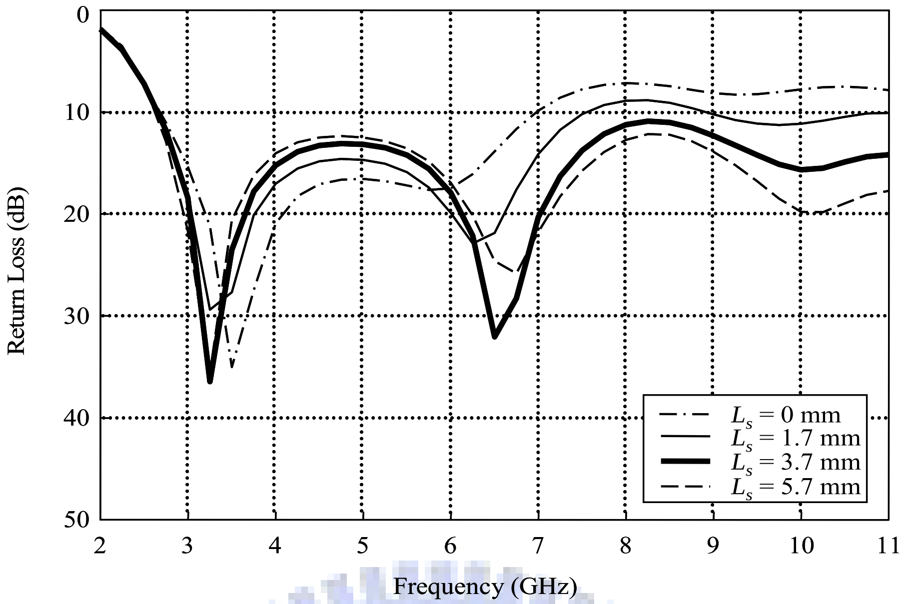

Figure 2.13 Simulated return losses for the proposed antenna of various bevel length L_s with a fixed value of W_s = 7mm. Other geometric parameters are the same as given in Figure 2.9.

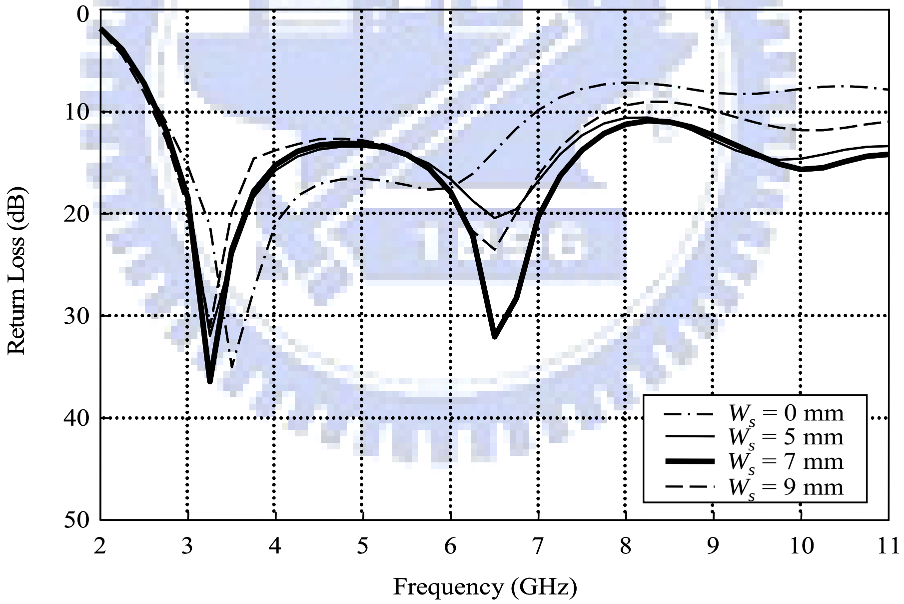

Figure 2.14 Simulated return losses for the proposed antenna of various bevel width W_s with a fixed value of L_s = 3.7mm. Other geometric parameters are the same as given in Figure 2.9.

Additionally, two semicircle slots cut in the bottom side of the ground plane may further improve the antenna performance. The effects of different radii and positions of the semicircle slots were investigated. The simulated return losses for various sizes and positions of the semicircle slot are shown in Figure 2.15 and Figure 2.16. It can be seen in Figure 2.15 that the return loss curves have similar shapes for the three different slot radii (r = 2.0, 2.5, and 3.0 mm) at low frequencies, but the high frequency impedance matching changes significantly with the variation of r. In Figure 2.16, when W_e becomes larger (i.e., becoming farther from the side edge of the ground plane), the high frequency matching is slightly improved.

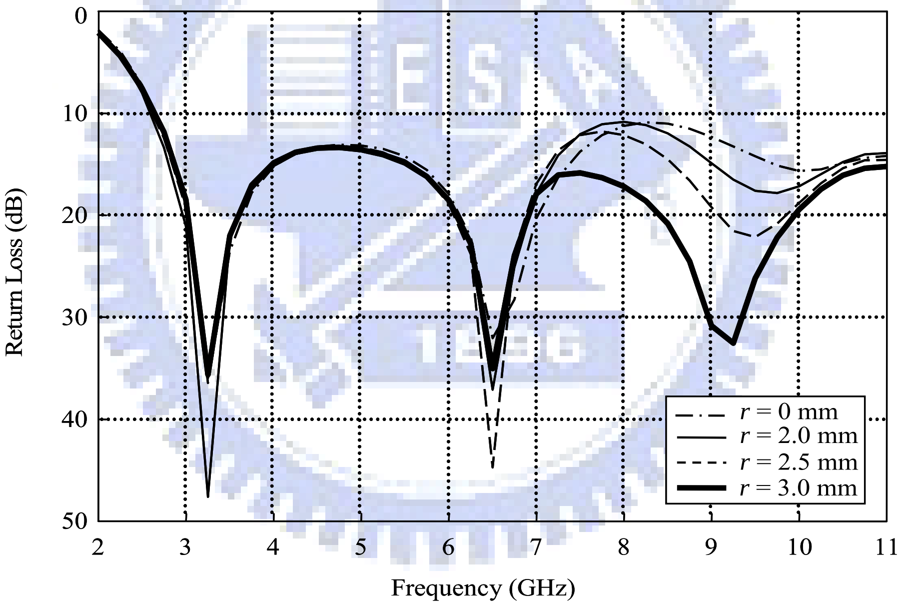

Figure 2.15 Simulated return losses for the proposed antenna of various slot radii r with a fixed value of W_e = 3 mm. Other geometric parameters are the same as given in Figure 2.9.

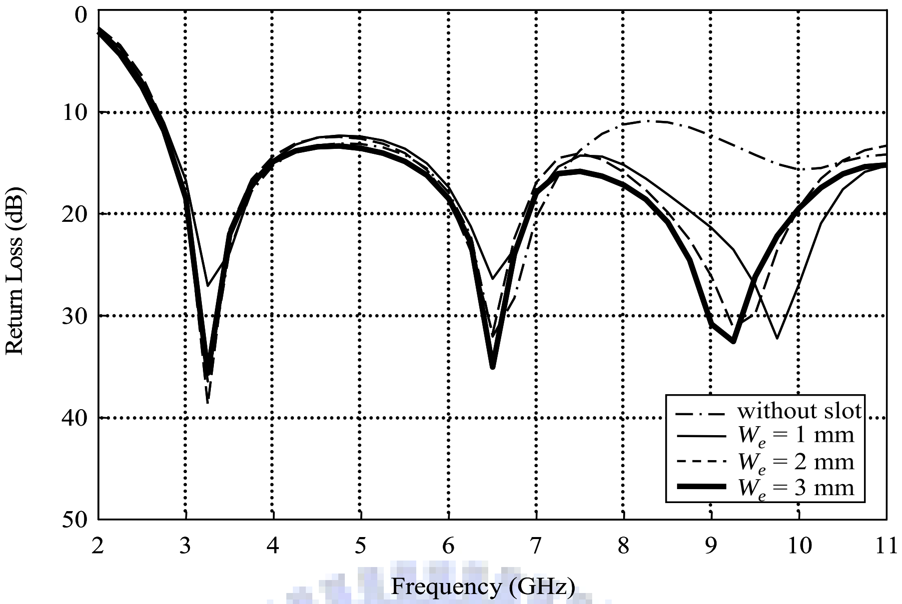

Figure 2.16 Simulated return losses for the proposed antenna of various distance W_e with a fixed value of r = 3 mm. Other geometric parameters are the same as given in Figure 2.9.

The radiation pattern in low frequency band is omnidirectional, but it usually deteriorates in the high frequency region. It is because that at the high frequencies, the magnetic currents mainly distributed over the slots between the radiation patch and the ground plane. The waves travel through the slots cause directional radiation patterns in the horizontal plane (i.e., the *xz*-plane). By introducing these two semicircle slots, the transverse currents on the ground plane near the bottom side diminish. Thus the waves radiated from the slot propagate in a more omnidirectional way. Also, since the currents on the ground plane at high frequencies are rectified with the insertion of the two semicircle slots, more power is fed into the slots between the patch and the ground plane. As the results, the return-loss bandwidth of the antenna is broadened, and the gains in high frequency band become larger. Figure 2.17 shows the comparison of the simulated 3-D radiation patterns with and without the semicircle slots at 9 GHz. In Figure 2.17, the radiation pattern with semicircle slots is more omnidirectional than that without slots in the horizontal plane (i.e., the *xz*-plane).

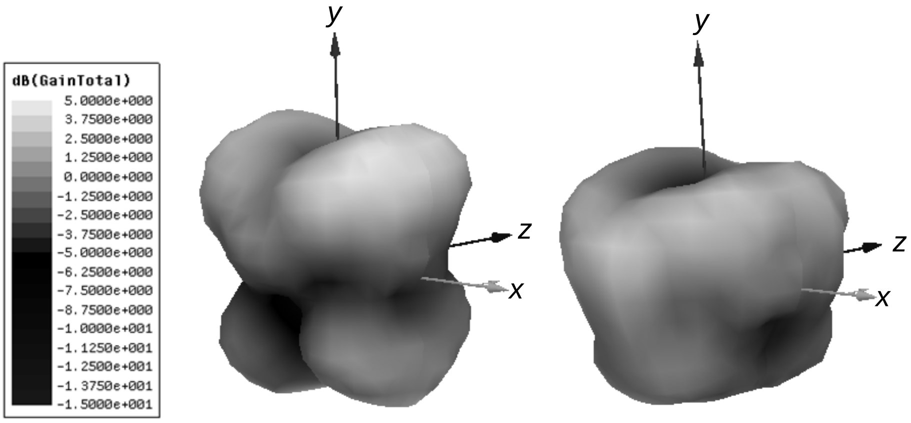

without semicircle slots with semicircle slots

Figure 2.17 Simulated 3-D radiation patterns with and without semicircle slots in the ground plane of the proposed antenna at 9 GHz.

B. UWB Antenna with Band-Notched Function Design

The frequency range for UWB systems approved by the FCC is between 3.1 GHz to 10.6 GHz. It might cause interference to the existing wireless communication systems, for example the WLAN operating in 5.15-5.85 GHz. Therefore, the UWB antenna with a band-notched characteristic is required. To obtain the band-notched function, there are various methods to achieve it as described in Chapter 1. The conventional methods are cutting a slot on the patch [46]-[54], inserting a slit on the patch [55]-[57], embedding a quarter-wavelength tuning stub within a large slot on the patch [58], or using the SRR structure on the patch [59]-[60]. Another way is putting parasitic elements near the printed monopole as filters to reject the limited band [61]-[63] or introducing a parasitic open-circuit element, rather than modifying the structure of the antenna's tuning stub [64]. Changing the feed structure is also a method to achieve the band-notched response such as using the lumped and distributed inductors and capacitors integrated on the top side of the substrate in front of the feed port [65] and inserting two quarter-wavelength tuning stubs or a resonance cell into the proposed feeding [66]-[67].

In our design, the concept of the parallel LC circuit is applied. At resonant frequency, the parallel LC circuit will cause high input impedance that leads to the desired high attenuation and impedance mismatching near the notch frequency. In this section, a pair of T-shaped stubs is embedded inside an elliptical slot cut in the radiation patch to form the parallel LC circuit. The elliptical slot and the T-shaped stubs are equivalent to an inductor and a capacitor, respectively. By adjusting the inductor and capacitor values, the suitable notch frequency and bandwidth can be achieved.

Figure 2.18 shows the simulated return losses for various axial ratios (*AR*) of the elliptical slot with the minor axis fixed at 2.3 mm. It is seen that, increasing the axial ratio, which is similar to increasing the inductor value of the parallel LC circuit, has the effects of adjusting the center notch frequency as well as increasing the notch bandwidth. When *AR* varies from 1.8 to 2.2 mm, the center notch frequency varies from 6 to 5 GHz. On the other hand, as W_c increases, the rejection-band region moves toward lower frequency with a narrower notch bandwidth. It is similar to increasing the capacitor value of a parallel LC circuit. The simulated return losses for various W_c are shown in Figure 2.19. When W_c varies from 2.6 to 5.6 mm, the center notch frequency varies from 6.5 to 4.75 GHz. Thus, the notch frequency can be adjusted by selecting the suitable W_c and *AR*.

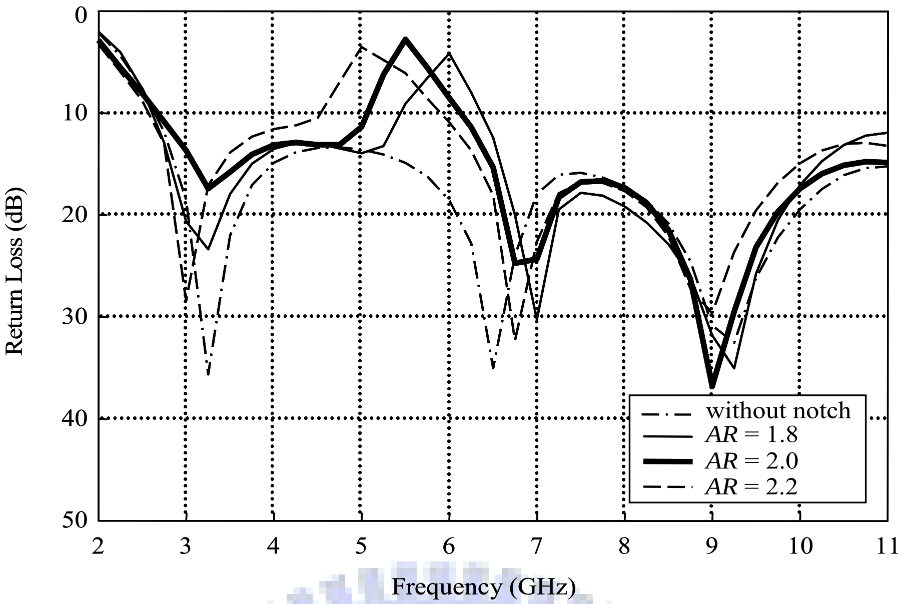

Figure 2.18 Simulated return losses for the proposed antenna of various axial ratio (*AR*), the minor axis is 2.3 mm with a fixed value of W_c = 3.6 mm. Other geometric parameters are the same as given in Figure 2.9.

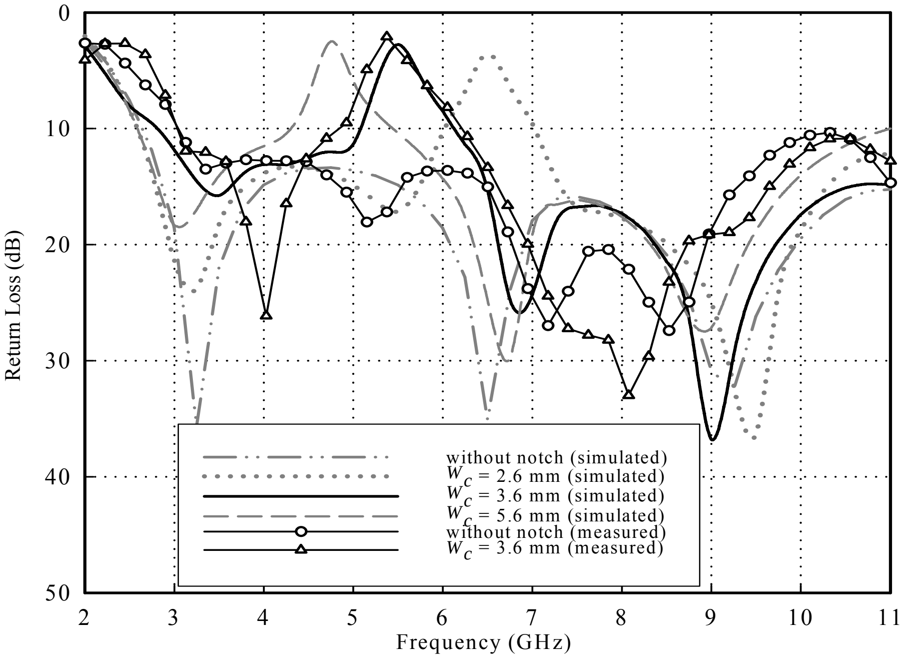

Figure 2.19 Simulated and measured return losses of the proposed antenna for various T-shaped stub width W_c with a fixed value of *AR* = 2. Other geometric parameters are the same as given in Figure 2.9.

In the case of W_c = 3.6 mm and *AR* = 2.2, the resistance and reactance of the proposed antenna at 5.5 GHz are 112Ω and 146Ω, respectively. This high input impedance causes impedance mismatching at the notch frequency, and the band-notched function covering the WLAN frequencies is obtained. Based on the analysis described above, the optimized design value of each physical dimension of the proposed antenna is determined and as shown in Figure 2.9. The simulated current distribution at 5.5 GHz is shown in Figure 2.20. It reveals that the currents mainly concentrate over the area of the two T-shaped stubs inside the elliptical slot cut in the radiation patch.

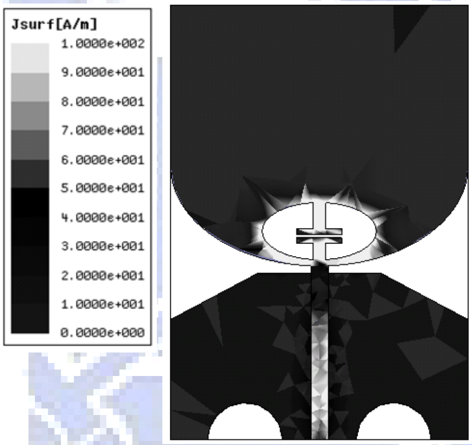

Figure 2.20 Simulated current distribution of the proposed antenna at 5.5 GHz.

2.2.3 Experiment Results

The measured return losses of the proposed antenna with and without the band-notched function are also shown in Figure 2.19. Without band-notched function, the antenna bandwidth (2:1 VSWR, or about 9.5 dB return loss) covers the range of 3.1-10.6 GHz assigned for the UWB application. Whereas with the band-notched function, the bandwidth is from 2.95 GHz to more than 11 GHz, and the antenna has a rejection frequency band of 5 to 6 GHz, where the wireless LAN service is allocated, when inserting the equivalent parallel LC circuit into the radiation patch. An immediate sharp increase in VSWR is observed at the notch frequency.

Figure 2.21(a) to (d) show the measured radiation patterns at 3, 5.5, 6 and 9 GHz, respectively. It can be seen that the patterns of the proposed antenna at frequencies out of the notched band present omindirectional and stable radiation characteristics in the *xz*-plane (H-plane) over the operating frequency range, which are similar to that of the typical monopole antenna. The patterns measured at 5.5 GHz demonstrates that the antenna has much lower gains in the notched band than at other frequencies (3, 6 and 9 GHz), as shown in Figure 2.21(b).

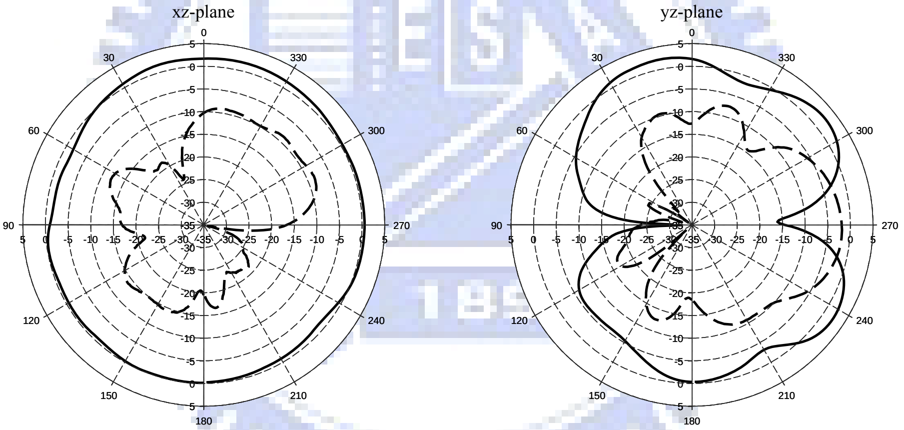

(a)

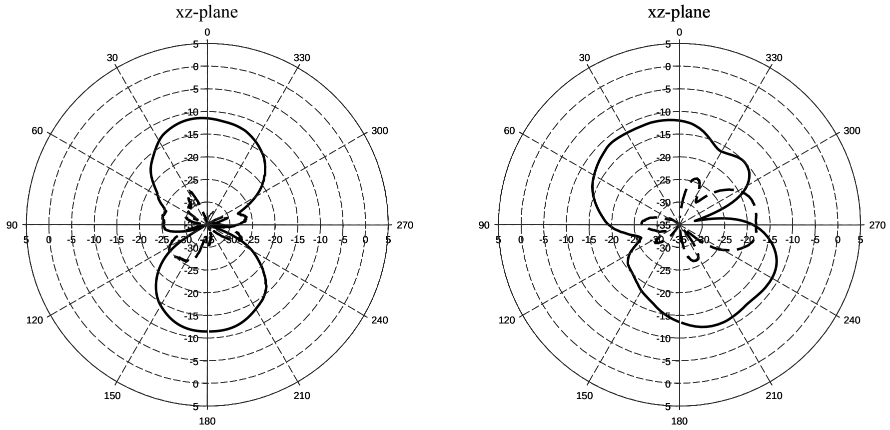

(b)

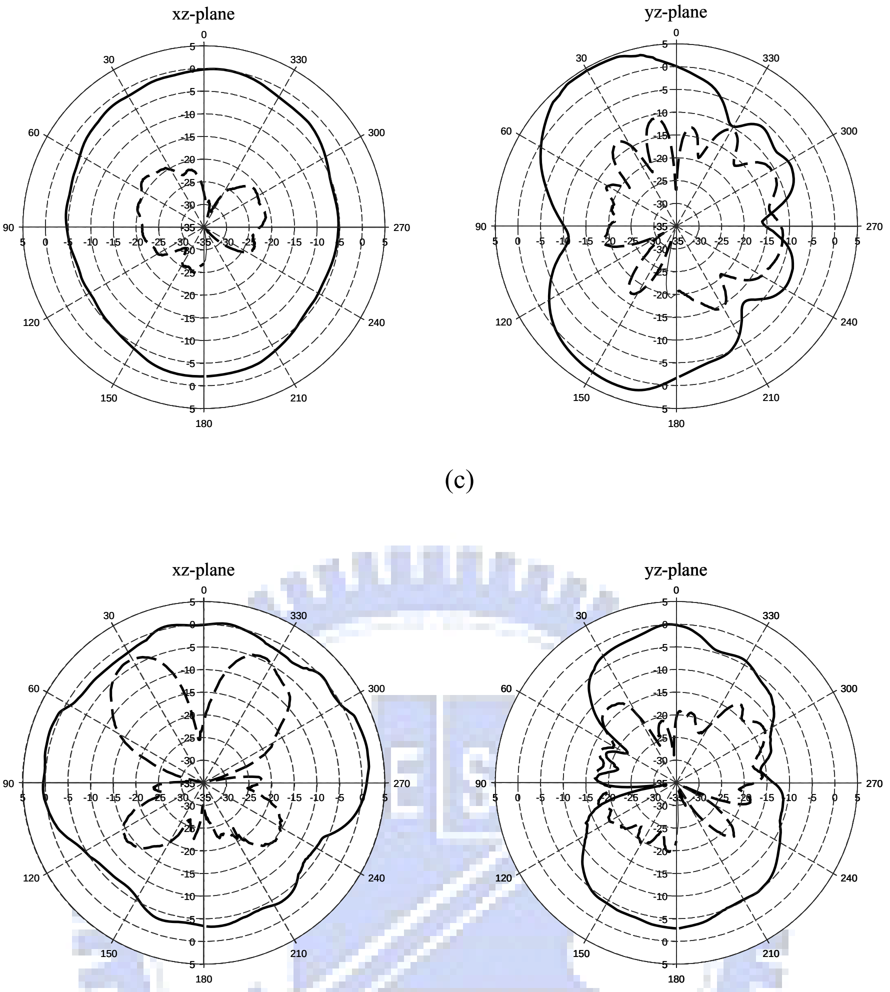

(c)

(d)

Figure 2.21 Measured radiation patterns at (a) 3 GHz, (b) 5.5 GHz, (c) 6 GHz, and (d) 9 GHz. (solid line: E_θ dashed line: E_ϕ)

The measured antenna gains from 3 to 10 GHz of the realized antenna are shown in Figure 2.22. The figure indicates that, the proposed antenna has good gain flatness except for in the notched band. The measured antenna gain variations are less than 4 dB throughout the desired UWB frequency band, and a sharp gain drop of about 10 dB occurs at 5.5 GHz.

The reduction in gain at the notch frequency is significantly greater than the reduction of power fed into the antenna caused by the return loss. This phenomenon can be investigated by examining the radiation efficiency. In Figure 2.22, the simulated radiation efficiency, which excludes the impedance mismatching effect, at 5.5 GHz is only about 21%. It is because that most currents are trapped in a small region of the equivalent parallel LC circuit at this frequency, as shown in Figure 2.20, the resultant radiation fields cancel out, and thus the antenna does not radiate efficiently. Figure 2.23 shows the photograph of the finished antenna.

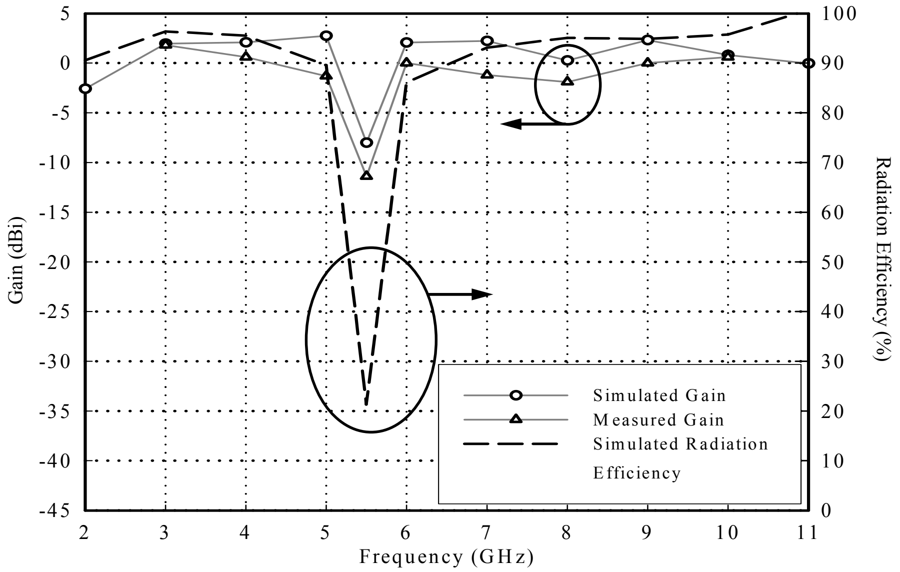

Figure 2.22 Gains and radiation efficiency of the proposed antenna with band-notched function.

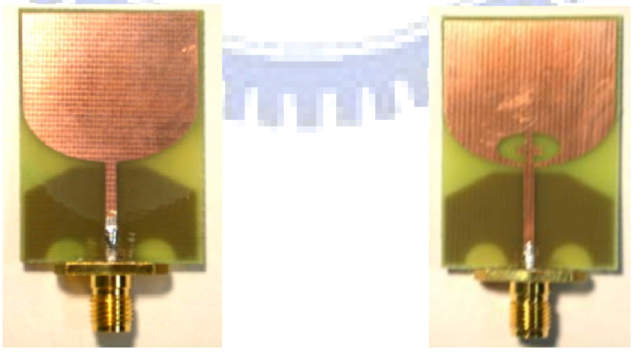

(a) (b)

Figure 2.23 Photograph of the proposed antenna. (a) Full band design and (b) with band-notch function design.

2.2.4 Summary

A compact microstrip-fed planar UWB antenna with the band-notched characteristic at around 5.5 GHz has been proposed and implemented. The total antenna size is 24 mm × 35 mm × 0.8 mm. Several design parameters have been investigated for the optimal design. By using two bevels on the upper side of the ground plane, the impedance matching in high frequency band can be improved. Moreover, adding two semicircle slots in the bottom side of the ground plane improve not only the input matching, but also the radiation characteristics at high frequencies. A pair of T-shaped stubs inside an elliptical slot, which is an equivalent parallel LC circuit, is realized to obtain the band-notched function. The center notch frequency and desired notch bandwidth are achieved by the properly designed equivalent capacitor and inductor values (i.e., W_c and AR of the elliptical slot). It is seen from the measured results that the proposed antenna has omnidirectional radiation patterns and a rather flat gain variation over the full UWB band expect for in the notched band. Therefore, the proposed antenna is suitable for the UWB communication applications and at the same time prevents interference with the WLAN systems.

Chapter 3

A Simple Monopole-like Printed Ultra-wideband Antenna with a Quasi-Transmission Line Section

In this chapter, we propose a simple and compact monopole-like printed ultra-wideband antenna. The antenna is composed of a monopole section and a quasi-transmission line section. The input signal from the feed line first passes through the line section then enters the monopole. The quasi-transmission line section provides different functions as the operating frequency changes. It serves not only as an impedance matching circuit but also a main radiator, which leads to the ultra-wideband performance of the antenna. The resonance mechanisms across the full band are described, followed by a thorough study of the antenna's geometrical parameters. The experimental results show good agreement with the simulation. The measured 10-dB return loss bandwidth is 93.2% from 3.57 to 9.80 GHz, with a total antenna size of 20 × 40 mm^2.

3.1 Antenna Configuration

Figure 3.1 (a) shows the geometry of the proposed antenna. It consists of a vertical monopole section and a short horizontal quasi-transmission line section. The quasi-transmission line section is formed by a parallel metal wire and the ground plane with a small gap of G. The metal wire has a length of L_t and a width of w_t. The height and width of the monopole section are denoted as H and w, respectively, and the size of the ground plane is $W \times L$. A 50 Ω microstrip line of 1.5 mm width is connected to the antenna as the feed line. The antenna is implemented on two sides of a FR4 substrate, whose dielectric constant is 4.4, loss tangent 0.02, and thickness 0.8 mm. Figure 3.1(b) is the geometry of a conventional printed monopole antenna for comparison.

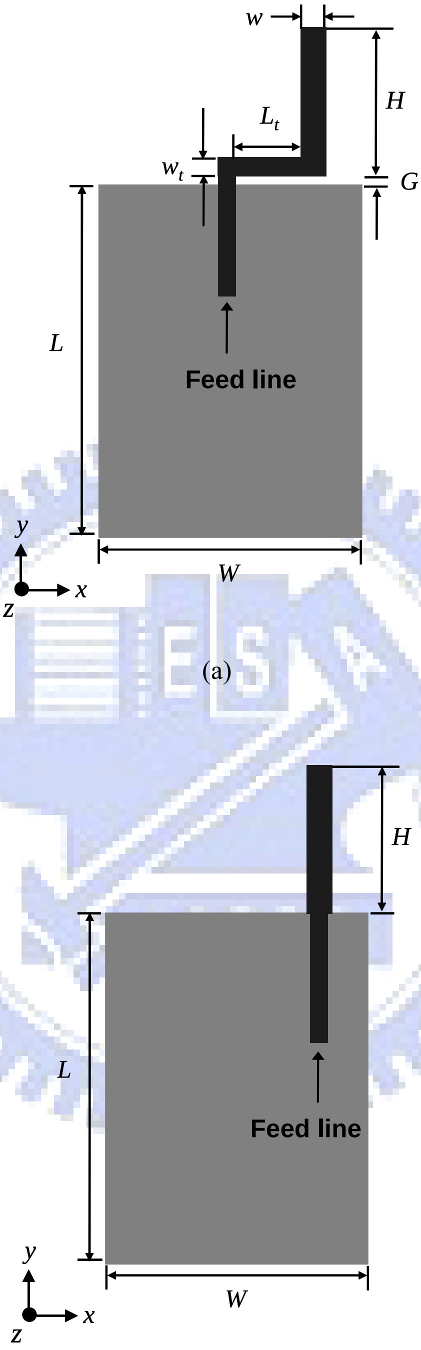

(b)

Figure 3.1 Geometries of (a) the proposed antenna and (b) a conventional monopole antenna.

3.2 Resonances of the Antenna

The resonance phenomenon of an antenna depends on the antenna configuration. For a wideband antenna, like a printed fat monopole antenna, it may not have only single but multiple resonances. In this section, the resonance mechanisms of the proposed antenna are described according to the simulated current distributions on the antenna structure. They can also be checked from the parameter study in Section IV. The antenna is simulated using the Ansoft High Frequency Structure Simulator (HFSS), which is a commercial 3-D full-wave electromagnetic simulation software.

Figure 3.2 shows the simulated return loss of the proposed antenna with the monopole of H = 12.4 mm, w = 2 mm and the quasi-transmission line of L_t = 4 mm, w_t = 1.5 mm, and G = 0.6 mm. The ground size $W \times L$ equals 20 mm × 27 mm. It is seen from the figure that, a total impedance bandwidth, determined by a 10-dB return loss, is about 98.6 % from 3.33 to 9.80 GHz. There are four resonances, with resonant frequencies at 3.66, 4.83, 6.46, and 8.43 GHz, sustaining the full band.

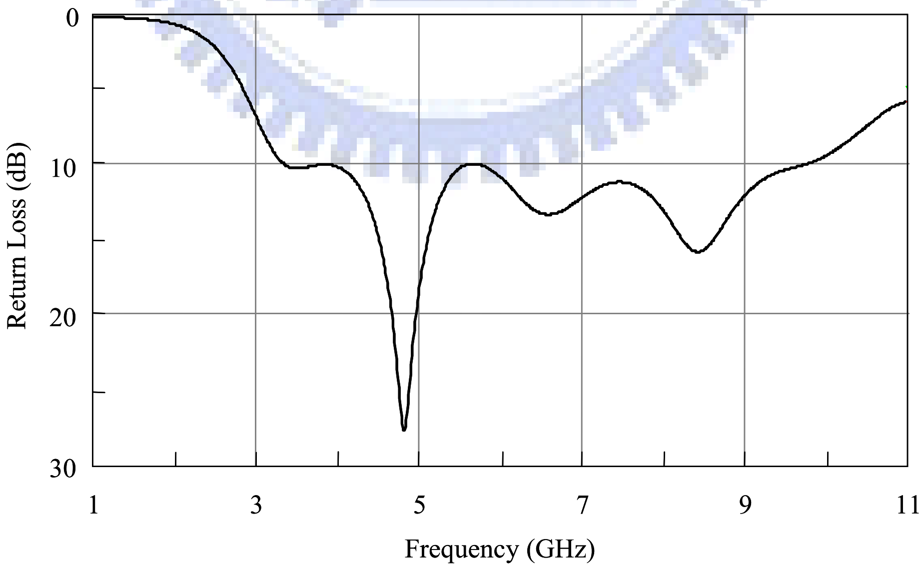

Figure 3.2 Simulated return loss of the proposed antenna with H = 12.4 mm, w = 2 mm, L_t = 4 mm, w_t = 1.5 mm, and G = 0.6 mm. The ground size $W \times L$ = 20 mm × 27 mm.

To understand the resonance mechanisms of the antenna, the current distributions at the four resonant frequencies are examined and shown in Figure 3.3 (a)-(d), respectively. At the first resonant frequency (Figure 3.3 (a)), the current on the vertical monopole section is weak as compared to that on the quasi-transmission line section. However, as will be shown later, the quasi-transmission line section at this frequency behaves as a series inductor, thus not corresponding to the antenna radiation. Although not obvious in the figure, it is actually the currents on the two sides of the ground plane contributing to the antenna radiation. It means that the ground plane is the main radiator at the present resonant frequency. This can be doubly checked in Section 3.4 when one changes the ground size to see the variation of the resonant frequency.

At the second resonant frequency (Figure 3.3 (b)), the vertical monopole section has the strongest current as compared to other portions of the proposed antenna. And the current vanishes at the open end and becomes larger when moving toward the connection point of the monopole and the quasi-transmission line section, which is a current distribution similar to that on a typical quarter-wavelength monopole antenna (Figure 3.1 (b)). It is thus evident that at the second resonant frequency of 4.83 GHz, the monopole section is the main radiator of the proposed antenna and functions as a quarter-wavelength monopole antenna.

As for the third resonant frequency (6.46 GHz), as shown in Figure 3.3 (c), the current is mainly distributed on the quasi-transmission line section, surrounding the transmission line gap *G*. The current vanishes near the right end of the line section and is a maximum at the left end. This current distribution is like that of a quarter-wavelength open slit antenna. Thus, the quasi-transmission line section plays a role as a resonant slit antenna, which is the key contributor of the antenna radiation at the third resonant frequency.

Finally, for the fourth resonant frequency of 8.43 GHz, the proposed antenna has a current distribution as shown in Figure 3.3 (d). The vertical monopole section has a strong current with a maximum at the midpoint and nulls at both ends. It is clear that a half-wavelength resonance is formed on this vertical monopole section. The monopole section is again the main radiator of the proposed antenna at this resonant frequency, and behaves as a half-wavelength monopole antenna.

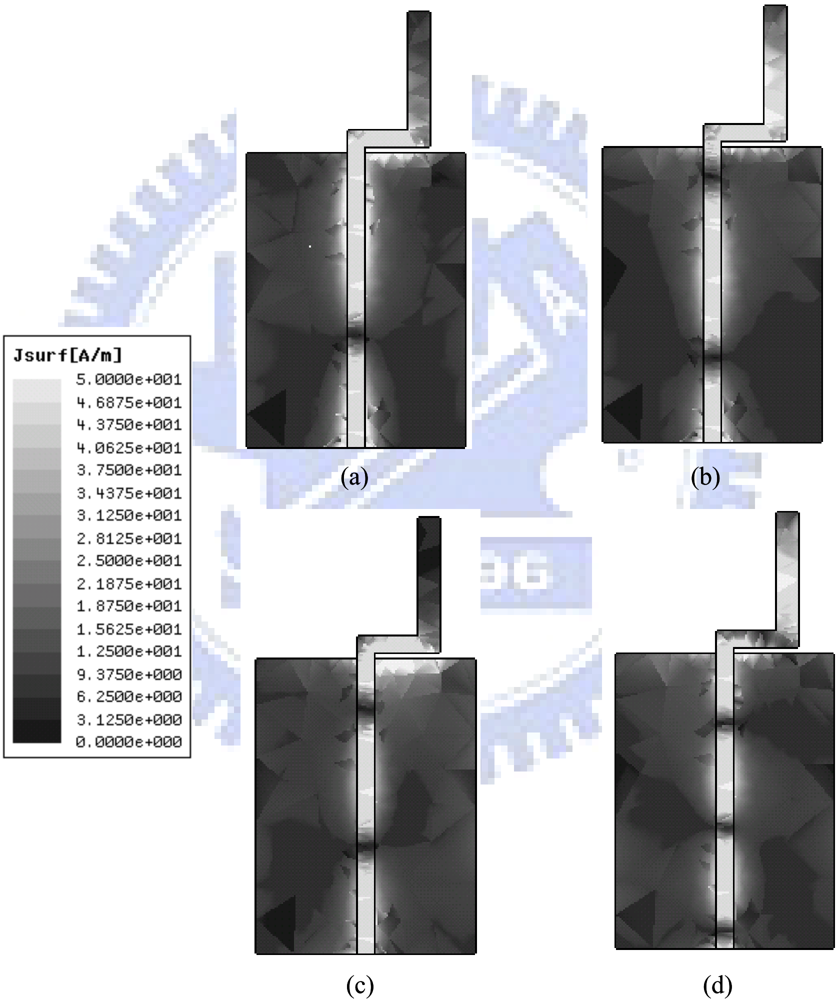

Figure 3.3 Simulated current distributions of the proposed antenna at (a) 3.66, (b) 4.83, (c) 6.46, and (d) 8.43 GHz.

3.3 Effect of the Quasi-Transmission Line Section

As shown in Figure 3.1, the quasi-transmission line section is the only geometrical difference of the proposed ultra-wideband antenna from a conventional narrow-banded monopole antenna. It is thus interesting to investigate its position on the antenna's wideband performance.

Figure 3.4 compares the input impedances of the proposed antenna (solid lines) and the convention monopole antenna (dashed lines). It is seen that the impedance behaviors of the two antennas are quite uncorrelated for frequency higher than 5 GHz. However, below that frequency, they have similar variation trends when the frequency varies. The proposed antenna has an input resistance smaller but close to that of the monopole antenna, and possesses a more inductive input reactance. Therefore, it can be modeled as a conventional monopole antenna in series with an inductor. This means that the quasi-transmission line section in the proposed antenna serves as an inductor at the lower frequency range. Figure 3.5 shows the equivalent circuit model of the antenna. Since electric charges may accumulate at the bend formed at the connection point of the monopole and quasi-transmission line sections, a small shunt capacitance is added. The simulated input impedance of the equivalent circuit model, with a series inductance of 1.3 nH and a small shunt capacitance of 0.14 pF, is shown as the dotted lines in Figure 3.4. (The values of the inductance and capacitance are obtained by curve fitting.) It is obvious that the results agree very well with the input impedance of the proposed antenna for frequency lower than 5 GHz. It can thus be concluded that, the quasi-transmission line section provides a series inductance for canceling the capacitive input reactance of the monopole antenna due to insufficient monopole length at the lower frequency, thus improving the impedance matching of the proposed antenna.

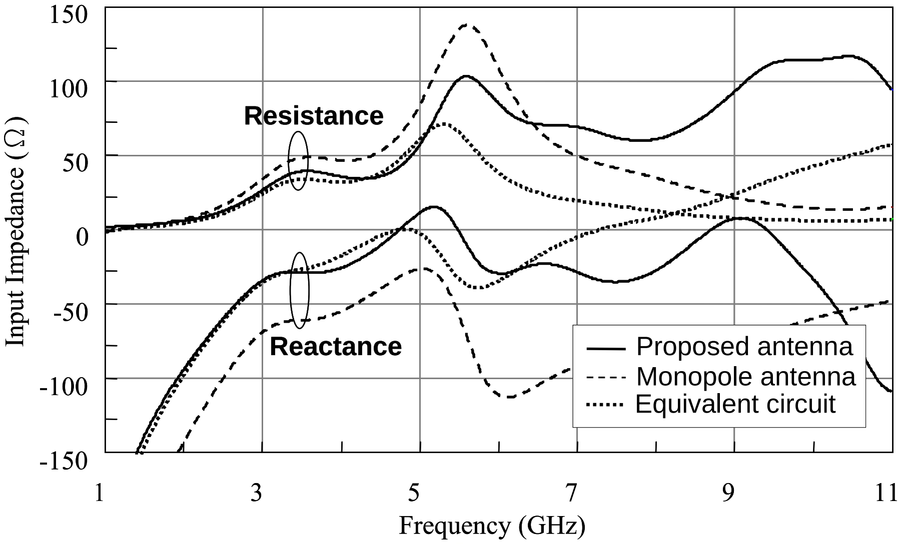

Figure 3.4 Comparison of the input impedances of the proposed antenna, the conventional antenna, and the equivalent circuit. H = 12.4 mm, w = 2 mm, L_t = 4 mm, w_t = 1.5 mm, and G = 0.6 mm. The ground size $W \times L$ = 20 mm × 27 mm.

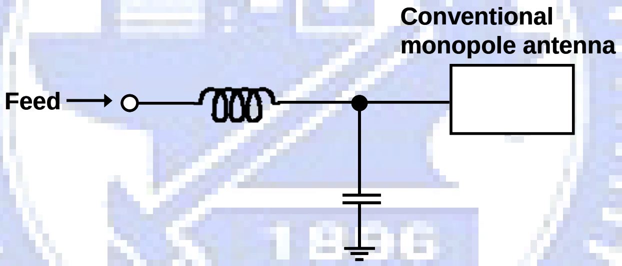

Figure 3.5 Equivalent circuit model of the proposed antenna at lower frequency range (f < 5 GHz) with series inductance of 1.3 nH and shunt capacitance of 0.14 pF.

As for frequency higher than 5 GHz, there are two antenna resonances in this range, one at 6.46 GHz and the other at 8.43 GHz. For frequency near 6.46 GHz, according to the simulated current distribution in Figure 3.3 (c), the primary antenna current, which corresponds to the antenna radiation, is located around the quasi-transmission line section. Thus, the line section in this frequency range is no longer a circuit element but plays the role of a quarter-wavelength slit radiator.

Finally, for frequency near the last resonance (8.43 GHz), as stated earlier, a current null appears at the right end of the quasi-transmission line section, forcing a half-wavelength resonance at the vertical monopole section of the proposed antenna. From the simulation, if one increases the length of the quasi-transmission line section, it is found that the current null will move into the line section, extending the resonant length of the monopole current, and thus resulting in a lower resonant frequency. It seems that the quasi-transmission line section in this frequency range acts as a current buffer for the resonant monopole section, and has the function like a quarter-wavelength impedance transformer, which transfer the high input impedance of the end-fed half-wavelength monopole antenna to the 50 Ω feed line impedance.

In summary, the quasi-transmission line section of the proposed antenna provides different functions as the operating frequency changes. In the frequency range covering the first two antenna resonances, the quasi-transmission line length is short as compared to the wavelength, and it is equivalent to a series inductor for improving the input impedance matching. As the frequency increases to the third resonant frequency, a strong quarter-wavelength current resonance happens at the quasi-transmission line section itself. It turns out to be the main radiator of the antenna. After that, as the frequency further increases to the last resonance, the line section changes again to a circuit element, i.e., a quarter-wavelength transformer, for input impedance matching.

3.4 Parameters Analysis

In this section, the effect of the antenna's geometrical parameters on the antenna performance is to be investigated. The results would respond to the descriptions made in the last two sections.

Figure 3.6 shows the simulated frequency response of the return loss for various lengths L_t (3, 4, 5, 6 mm) of the quasi-transmission line section. It is first observed that the third resonant frequency decreases as the length is increased, since the quasi-transmission line section behaves as a quarter-wavelength slit antenna for this resonance. For the first two resonances, the line section provides the inductance for impedance matching. The increase of the length would raise the inductance and thus alter the matching condition. Notably, the second resonant frequency decreases quite obviously as the increase of the length. This can be explained from Figure 3.4 that, when L_t increased, the input resistance curve of the equivalent circuit model remains unchanged and has a value near 50 Ω, while the corresponding input reactance curve will be raised due to the increase of the equivalent inductance. The zero-crossing frequency of this reactive curve would thus move toward the lower frequency, thus causing the second resonant frequency changed as shown in Figure 3.6. Lastly, one observes that the fourth resonant frequency decreases with the increase of L_t, which is, as mentioned earlier, the result due to the resonant length extension of the half-wavelength monopole current.

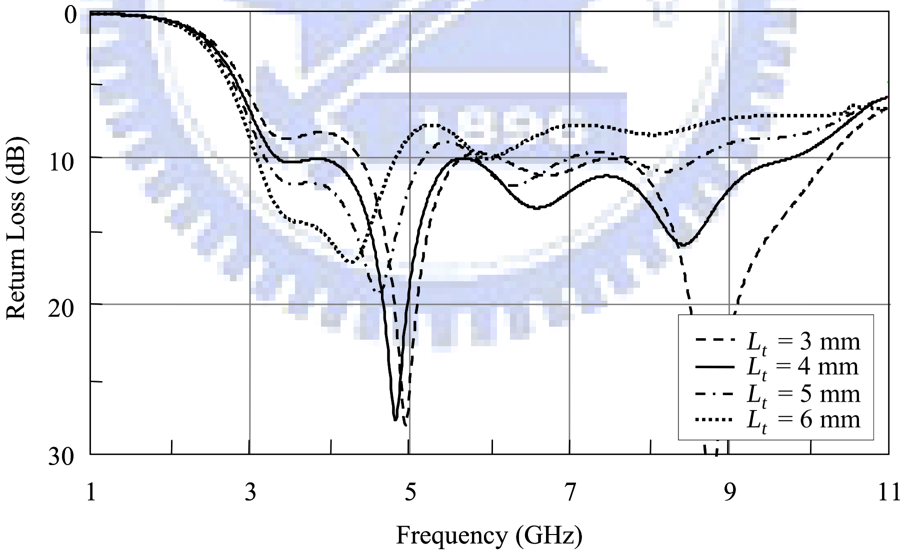

Figure 3.6 Simulated return losses for the proposed antenna of various length L_t of the quasi-transmission line section. Other geometric parameters are the same as given in Figure 3.2.

Figure 3.7 shows the variations of the return-loss frequency response when the width w_t of the quasi-transmission line section is decreased from 2.5 mm to 1.0 mm.

The change of the width influences the equivalent impedance of the line section, and thus mainly affects the impedance matching of the antenna. The resonant frequencies are negligibly changed except the second one. The decreasing of the second resonant frequency, as the width reduced, is due to the increase of the equivalent inductance, causing the zero-crossing frequency of the reactive curve moving toward the low frequency end. It is seen that by properly choosing the width w_t (= 1.5 mm), better input impedance matching can be achieved over the whole frequency band. Figure 3.8 depicts the simulated return losses for various gap widths G (3.0, 1.0, 0.6, 0 mm) of the quasi-transmission line section. Similar to the influence of w_t, the gap variation primarily affects the quasi-transmission line impedance and thus the impedance matching of the antenna. However, the frequency behavior alters dramatically when G = 0 mm. This is because that at this value, the gap in the quasi-transmission line vanishes and the original slit antenna at the third resonance no longer exits, leading to the drastic impedance mismatch from 6 to 8 GHz.

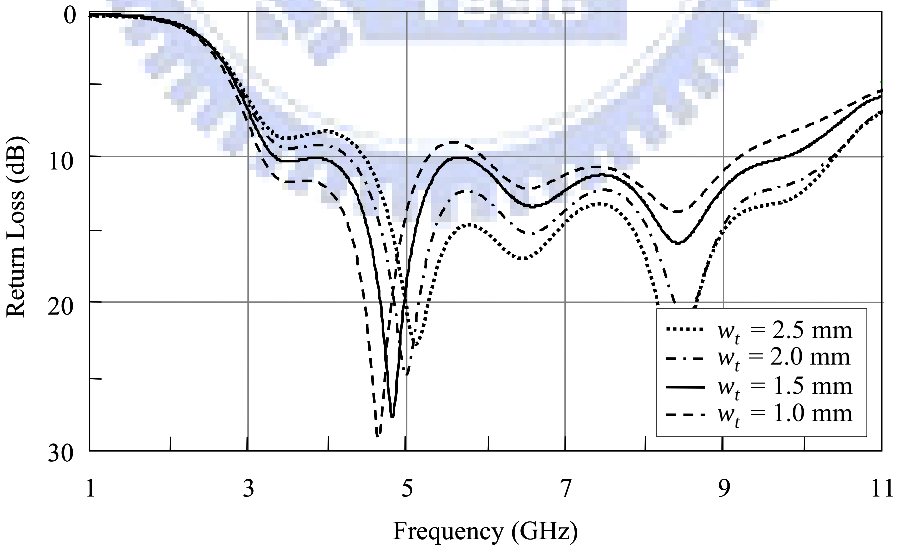

Figure 3.7 Simulated return losses for the proposed antenna of various width w_t of the quasi-transmission line section. Other geometric parameters are the same as given in Figure 3.2.

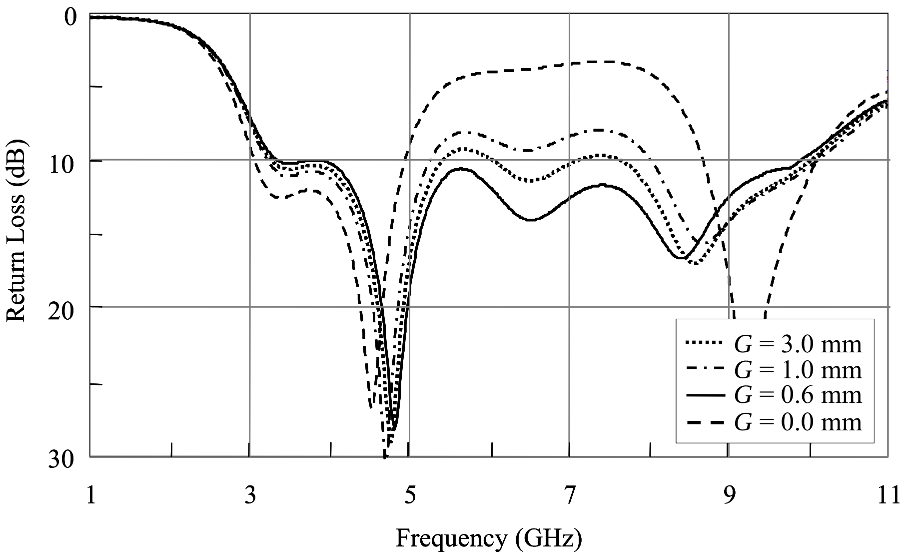

Figure 3.8 Simulated return losses for the proposed antenna of various gap *G*. Other geometric parameters are the same as given in Figure 3.2.

Figure 3.9 and Figure 3.10 illustrates the simulated return losses when varying, respectively, the height *H* (11.4, 12.4, 13.4, 14.4 mm) and width *w* (2.5, 2.25, 2.00, 1.75 mm) of the monopole section. Since the monopole section serves as a quarter-wavelength and a half-wavelength radiator, respectively, at the second and the fourth resonant frequencies, the increase of its length would lead to the decrease of these two frequencies as observed in Figure 3.9. A close examine reveals that as the height *H* varies from 11.4 to 14.4 mm, the second resonant frequency moves from 4.87 to 4.62 GHz and the fourth one from 8.61 to 7.90 GHz. The frequency ratio of the latter to the former keeps around a fixed value of 1.7. On the other hand, as seen from Figure 3.10, changing the monopole width *w* has little influence on the resonant frequencies. However, it will affect the antenna's input impedance, especially in the high frequency range around the fourth resonant frequency. Properly selecting the monopole width can lead to a largest high band edge and thus a widest impedance bandwidth.

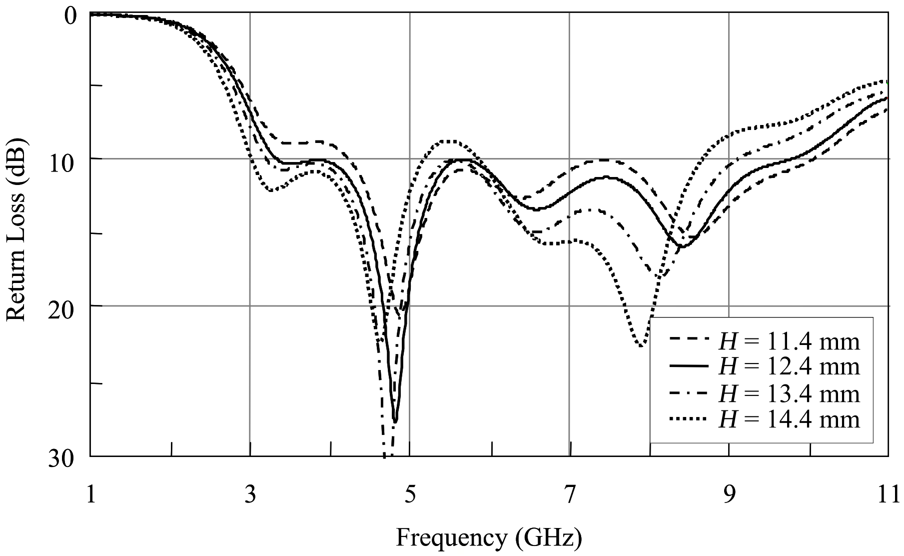

Figure 3.9 Simulated return losses for the proposed antenna of various height *H* of the monopole antenna. Other geometric parameters are the same as given in Figure 3.2.

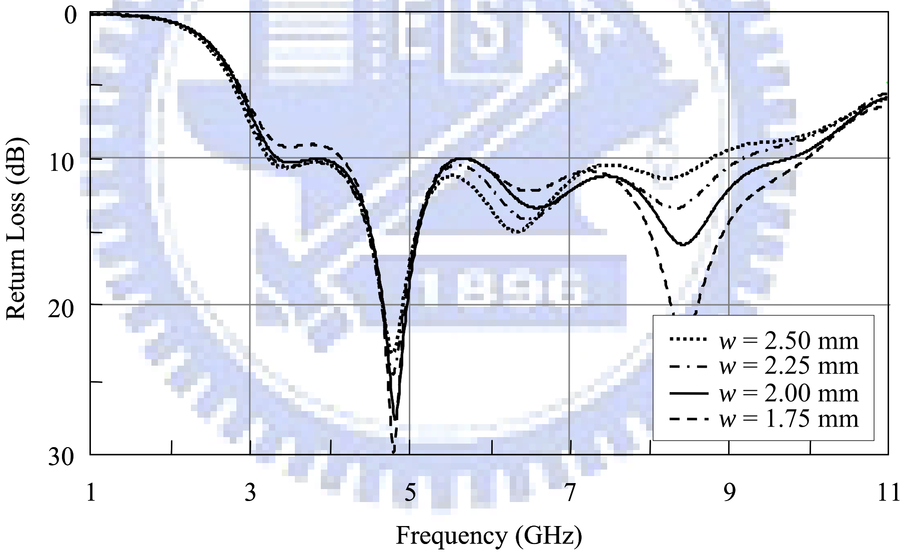

Figure 3.10 Simulated return losses for the proposed antenna of various width *w* of the monopole antenna. Other geometric parameters are the same as given in Figure 3.2.

Finally, the effect of the ground plane size is considered. The ground plane of a small antenna is actually an important portion of the antenna, since the induced current on it may have significant contribution to the radiation field as compared to other parts of the antenna. Figure 3.11 depicts the results of varying the ground plane length *L* (25, 27, 29, 31 mm) with the width *W* fixed at 20 mm. It can be observed that the change of *L* affects all the four resonances especially the first one. When *L* varies from 25 to 31 mm, the first resonant frequency moves from 3.67 to 3.12 GHz, and the impedance matching becomes apparently deteriorated. It is noticed that as compared to other geometrical parameters of the antenna, the ground plane length has the most manifest influence on the first resonance.

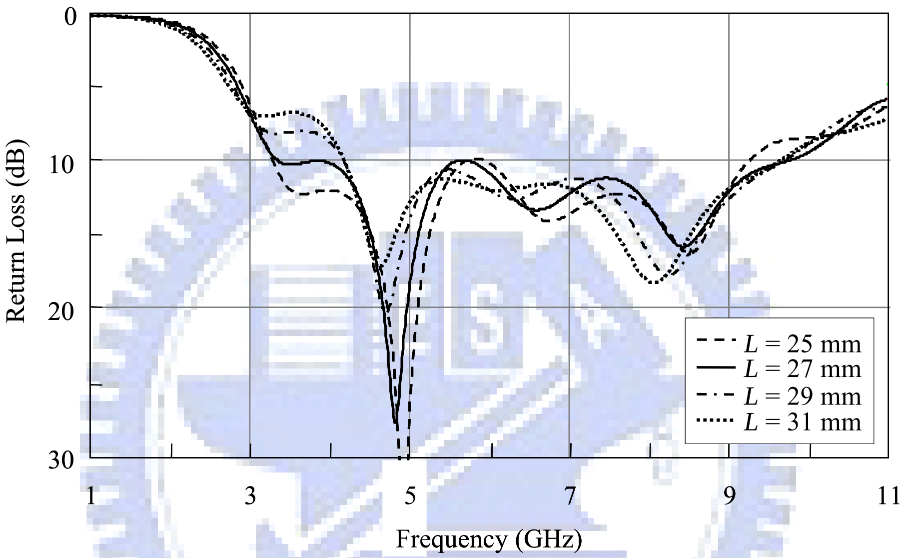

Figure 3.11 Simulated return losses for the proposed antenna of various length *L* of the ground plane. Other geometric parameters are the same as given in Figure 3.2.

Figure 3.12 depicts the results of varying the ground plane width *W* (18, 20, 22, 24 mm) with *L* = 27 mm. The variation of the ground plane width mainly influences the high frequency performance of the antenna. As is observed, when *W* increases, the input matching becomes better around the fourth resonant frequency, while worse around the third one. Also, the third resonant frequency decreases as the width increases. To explain this phenomenon, let us reexamine the current distribution of the third resonance shown in Figure 3.3 (c). It is observed that the induced ground plane current flows over the quasi-transmission line region and extends to the right edge of the ground plane. Therefore, the equivalent length of the corresponding quarter-wavelength slit antenna should be actually determined by not only the quasi-transmission line length L_t but also the ground plane width W. The increase of W would result in the increase of the equivalent slit antenna length, thus reducing the resonant frequency.

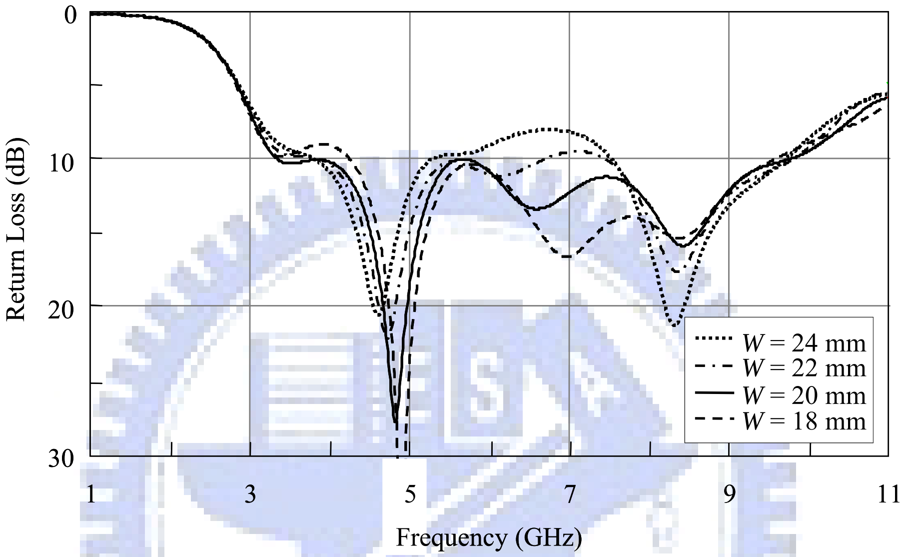

Figure 3.12 Simulated return losses for the proposed antenna of various ground width W. Other geometric parameters are the same as given in Figure 3.2.

3.5 Experiment Results

Figure 3.13 shows the measured, as well as the simulated, return losses of the proposed antenna. The dimensions of the antenna are $L_t \times w_t$ = 4 mm × 1.5 mm, G = 0.6 mm, $H \times w$ = 12.4 mm × 2 mm, and $W \times L$ = 20 mm × 27 mm. It is seen that the 10-dB return loss bandwidth is 6.23 GHz, extending from 3.57 to 9.8 GHz. The four resonant frequencies are located at 3.67, 4.65, 6.29, and 8.35 GHz, very close to the simulated ones. A best return loss of 22 dB is measured at the second resonant frequency. In general, the measured result agrees well with the simulated one.

Figure 3.14 (a) to (d) show the measured radiation patterns in the *xz*-plane at the four resonant frequencies (3.67, 4.65, 6.29 and 8.35 GHz), respectively. The measured peak gains (average gains) are correspondingly -0.07 dBi (-3.75 dBi), 0.66 dBi (-1.70 dBi), 4.02 dBi (-1.52 dBi), and 0.44 dBi (-2.06 dBi) at the four frequencies, as summarized in Table 3.1. It is noticed that the third resonance (quarter-wavelength slit antenna) at 6.29 GHz exhibits a higher antenna gain than other ones. Figure 3.15 shows the photograph of the finished antenna.

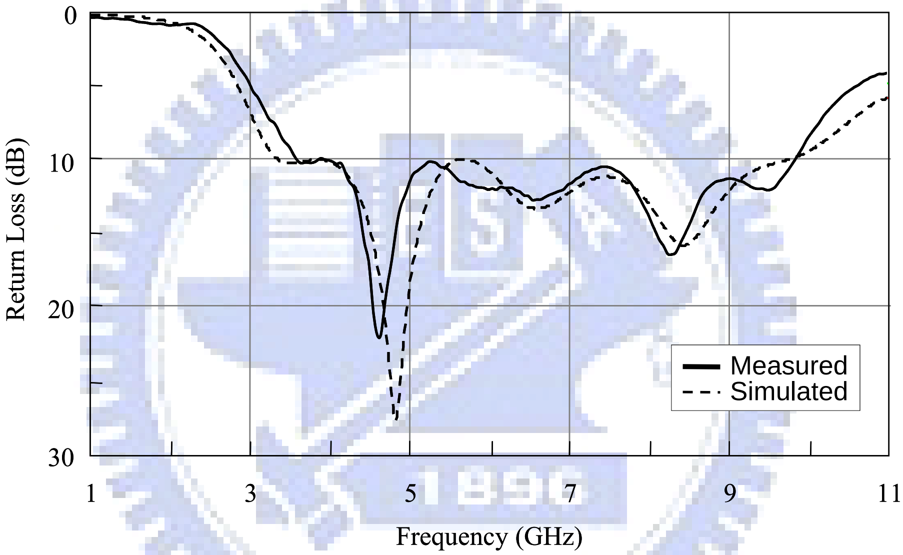

Figure 3.13 Measured and simulated return loss of the proposed antenna.

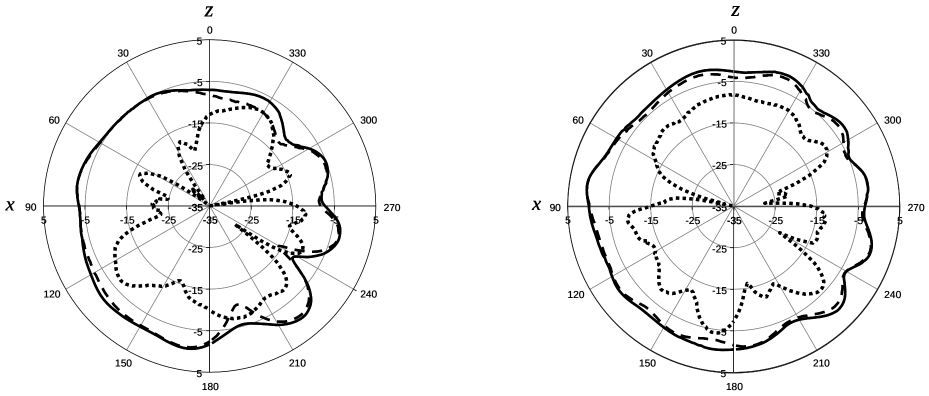

(a)

(b)

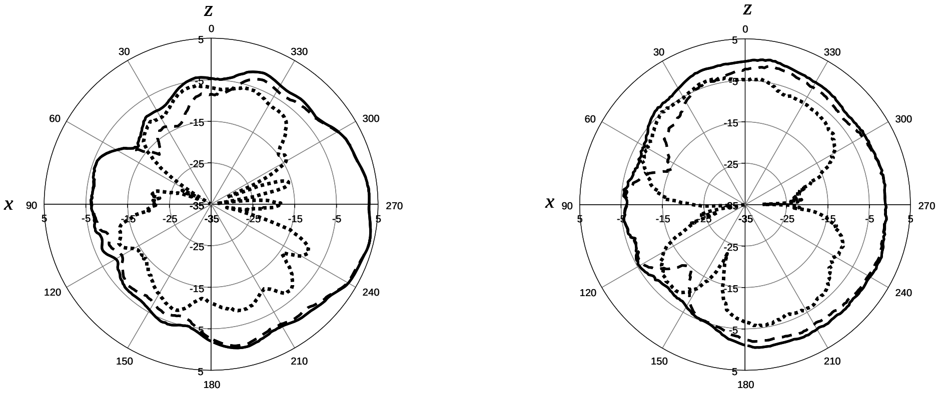

(c)

(d)

Figure 3.14 Measured radiation patterns at (a) 3.67 GHz, (b) 4.65 GHz, (c) 6.29 GHz, and (d) 8.35 GHz. (solid line: E_{total} ; dashed line: E_{phi} ; dotted line: E_{theta})

Table 3.1

The Measured Peak and Average Gains at Four Resonant Frequencies

Frequency (GHz)	Peak gain (dBi)	Average gain (dBi)
3.67	-0.07	-3.75
4.65	0.66	-1.70
6.29	4.02	-1.52
8.35	0.44	-2.06

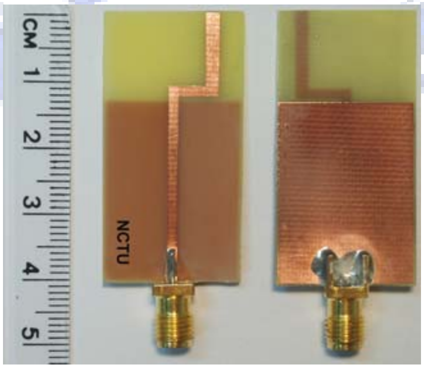

Figure 3.15 Photograph of the proposed antenna.

3.6 Summary

A simple and compact monopole-like printed ultra-wideband antenna has been proposed and analyzed. It has been demonstrated that the quasi-transmission line section in the proposed antenna structure provides multiple functions, which leads to the appearance of four continuous resonant modes and thus yields to the ultra-wideband performance. The quasi-transmission line section not only serves as an impedance matching circuit but also a main radiator in the appropriate frequency range. The resonant mechanisms of the antenna across the operational bandwidth have been described, which responded to the results from a thorough antenna parameters investigation. Finally, the measured results agree well with the simulation ones, with a peak gain of 4.02 dBi and a 10-dB return loss fractional bandwidth of 93.2% from 3.57 to 9.8 GHz. The proposed antenna has a compact size of 20 mm × 40 mm, which is suitable for wideband wireless communication applications.

Chapter 4

Low-Profile Ultra-Wideband Antenna with Strong Vertical Polarization Field

In this chapter, a low-profile ultra-wide band antenna with strong vertical polarization field is proposed. The antenna is made by a single folded metal plate, which has several advantages, including small size, light weight, low cost, and ease of fabrication. Two L-shaped slits are embedded on the ground plane, which provide additional resonances and improve the input impedance matching thus wideband performance can be obtained. Besides, according to the loop structure, the current direction on the feed and shorting strip are the same, hence, the proposed antenna has stronger vertical polarization field as compared to the conventional printed antenna in horizontal plane. The antenna radiation pattern is omnidirectional in the *xy*-plane. Moreover, the metal plane effect on the antenna performance also analyzed. The proposed antenna maintains good radiation characteristics while a metal plane is placed parallel under the antenna closely.

4.1 Configuration and Design

Figure 4.1 shows the three–dimensional (3-D) structure and geometry of the proposed antenna. The antenna is a loop structure. The input signal fed from the feed strip first enters the patch then passes through the shorting strip to the ground plane. The antenna is soldered on the PCB using a single folded metal plate formed by several bending manufacture procedure. The 12 edges polygonal radiation patch is a quasi-ellipse shape with the major axis and the minor axis are 25mm and 17 mm, respectively. The feed point is denoted as point *A* as shown in Figure 4.1. A 50 Ω microstrip line of 1.5 mm width is connected to the antenna as the feed line. The substrate chosen is FR4 substrate, whose dielectric constant is 4.4, loss tangent 0.02, and thickness 0.8 mm. The polygon patch size of the antenna $w_a \times \ell_a$ and the ground size is $W \times L$. The shorting strip is offset located at the corner of the patch opposite to the feed strip of the antenna and its width denotes as w_s. There are two L-shaped slits embedded on the ground plane, the size of the right slit is $w_1 \times \ell_1$ and the left slit is $w_2 \times \ell_2$. Also two cut portion of the ground plane are $w_3 \times \ell_3$. The gap width of the L-shaped slit is denoted as g. The feed depth and the position are d and s, respectively.

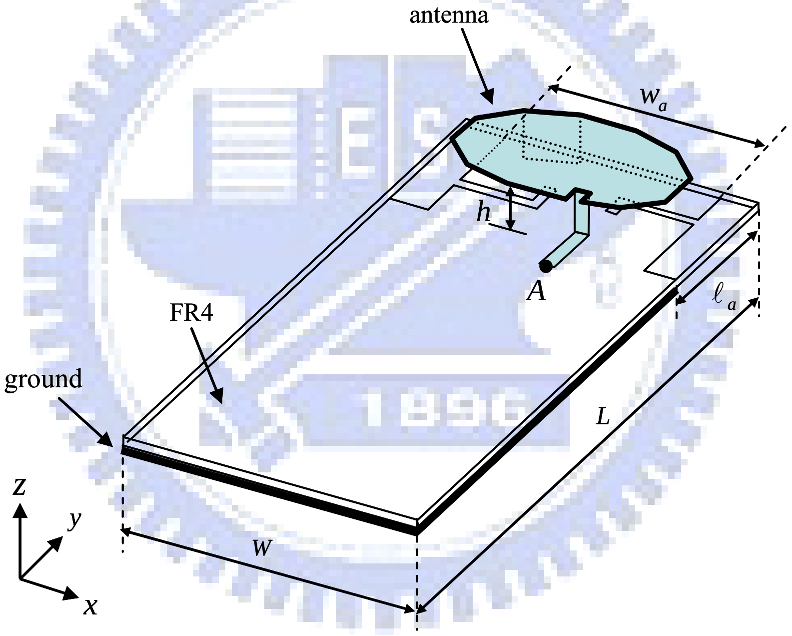

(a)

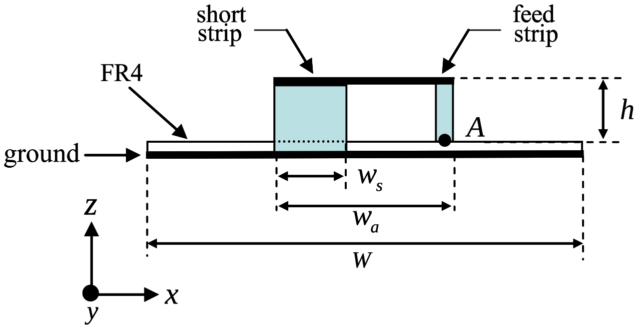

(b)

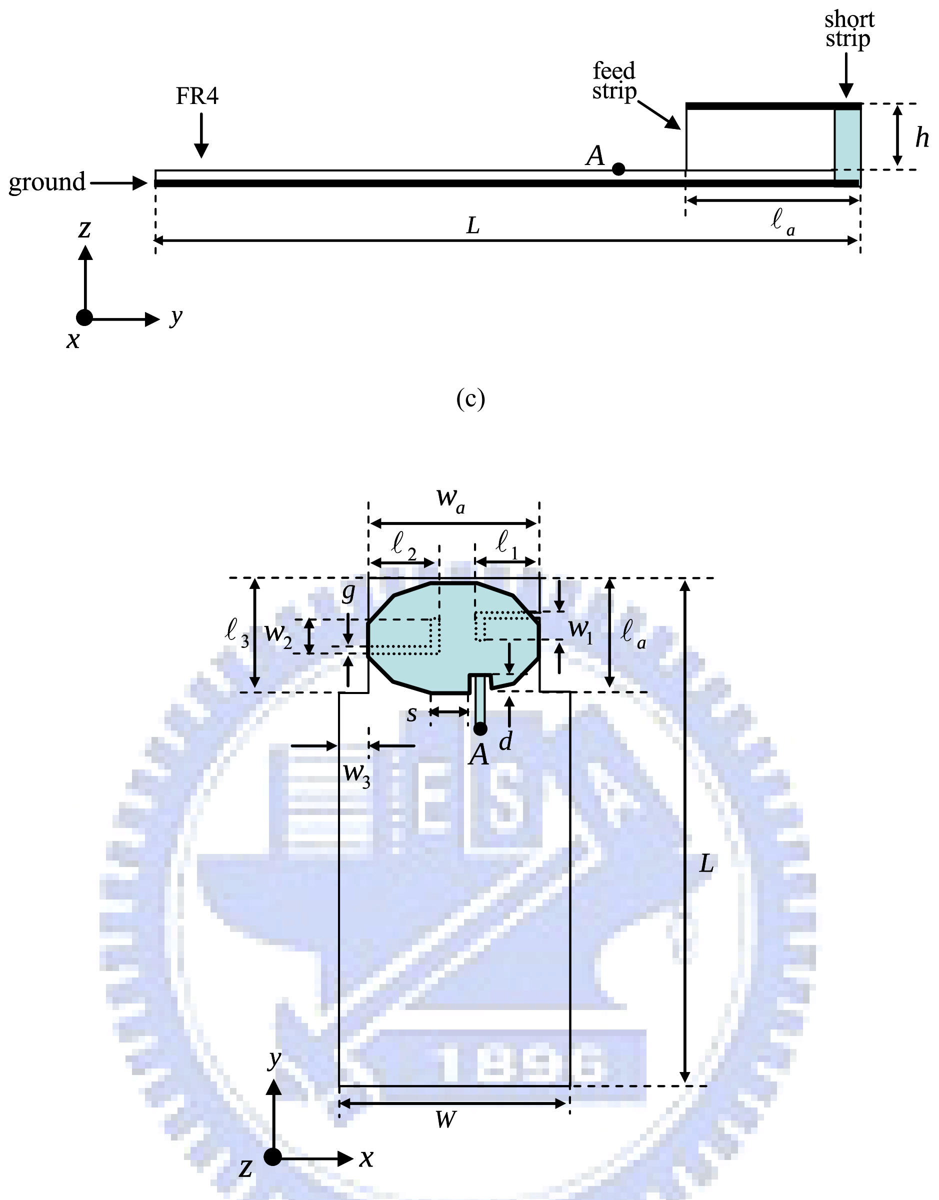

(c)

(d)

Figure 4.1 Geometry of the low-profile UWB antenna. (a) 3-D structure, (b) side view of *x*-*z* plane, (c) side view of *y*-*z* plane, and (d) top view of *x*-*y* plane.

Figure 4.2 shows the simulated return loss of the proposed antenna with and without the embedded L-shaped slits. The patch size of the antenna $w_a \times \ell_a = 25$ mm × 17 mm and the ground size is $W \times L = 34$ mm × 75 mm. The width and height of the shorting strip are $w_s = 5.85$ mm and $h = 5$ mm, respectively, while those of the feed strip are 1.5 and 5 mm, respectively. The depth and the position of the feed line are $d = 2.5$ mm and $s = 6.75$ mm, respectively. The slit on right side one is $w_1 \times \ell_1 = 9$ mm × 3 mm and the left side one is $w_2 \times \ell_2$ = 9.5 mm × 4 mm. The two cut portions of the ground plane are $w_3 \times \ell_3$ = 4.5 mm × 17 mm. The gap width g of the L-shaped slit is 1mm. As show in Figure 4.2, there is poor impedance bandwidth and only has one resonance (dashed line). The total impedance bandwidth, determined by a 10-dB return loss, is about 15.75 % from 3.45 to 4.04 GHz. But when we embedded two L-shaped on the ground plane (solid line), the total impedance bandwidth is about 44.53 % from 2.95 to 4.64 GHz. There are three resonances, with resonant frequencies at 3.19, 3.71, and 4.41, sustaining the full band.

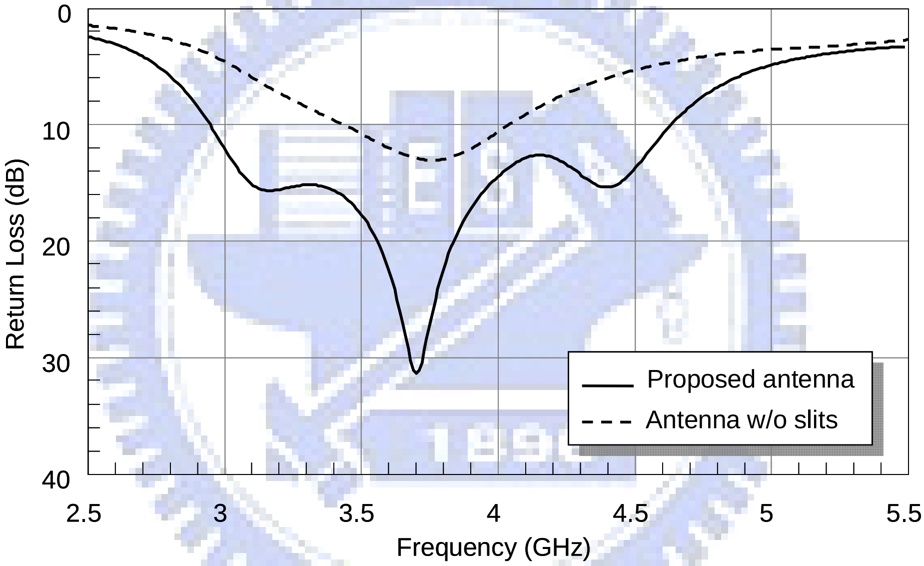

Figure 4.2 Simulated return loss for the proposed antenna shown in Figure 4.1 with and without slits. $w_a \times \ell_a$ = 25 mm × 17 mm, $W \times L$ = 34 mm × 75 mm, $w_1 \times \ell_1$ = 9 mm × 3 mm, $w_2 \times \ell_2$ = 9.5 mm × 4 mm, $w_3 \times \ell_3$ = 4.5 mm × 17 mm, w_s = 5.85 mm, h = 5mm, d = 2.5 mm, s = 6.75 mm, and g =1 mm.

For further comprehension on the embedded L-shaped slits mechanisms of the proposed antenna. Figure 4.3 compares the simulated return loss results of the antenna with and without the embedded L-shaped slit on the ground plane. The embedded arrangement have two position i.e., right or left side on the ground plane. As show in Figure 4.3 the dotted line means the antenna without embedded slits. It can be seen from the figure that, there is only one resonance across full band. But when a slit embedded on the ground plane in different arrangement, both of them result in an additional resonance at different frequency. The simulated return loss of the embedded slit at right side (solid line) and left side (dashed line) as show in Figure 4.3 for comparison. When the slit is adding at the right side on the ground plane, the additional higher resonance frequency (denote as f_3) is appeared. But when the slit is embedded at the left side on the ground plane, the lower resonance frequency (denote as f_1) is obtained. Besides, according to the results in the Figure 4.3, while the slit is embedded on different position, the second resonance frequency (denote as f_2) maintain its resonant surrounding 3.78 to 3.98 GHz.

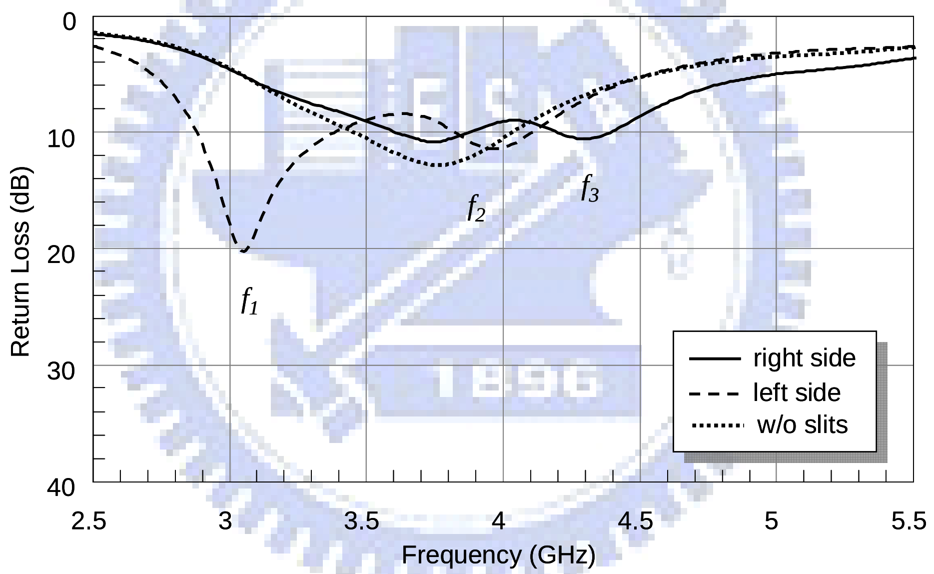

Figure 4.3 Comparison of the simulated return loss for the proposed antenna with different arrangement of the embedded slits. Other geometric parameters are the same as given in Figure 4.2.

Figure 4.4 (a) shows the effect on the resonance frequencies with various slit length ℓ_2. The influence on the second resonant frequencies is negligibly changed comparing the first one. It can be seen that the first resonance frequency decrease as ℓ_2 increase. When ℓ_2 varies from 9 to 15 mm, the first resonance frequency moves from 3.31 to 2.92 GHz. And the effect on the resonance frequencies with various slit length ℓ_1 is shown in Figure 4.4 (b). Notably, the third resonant frequency decreases quite obviously as the increase of the length ℓ_1. When ℓ_1 varies from 5 to 15 mm, the third resonance frequency moves from 7.54 to 3.05 GHz.

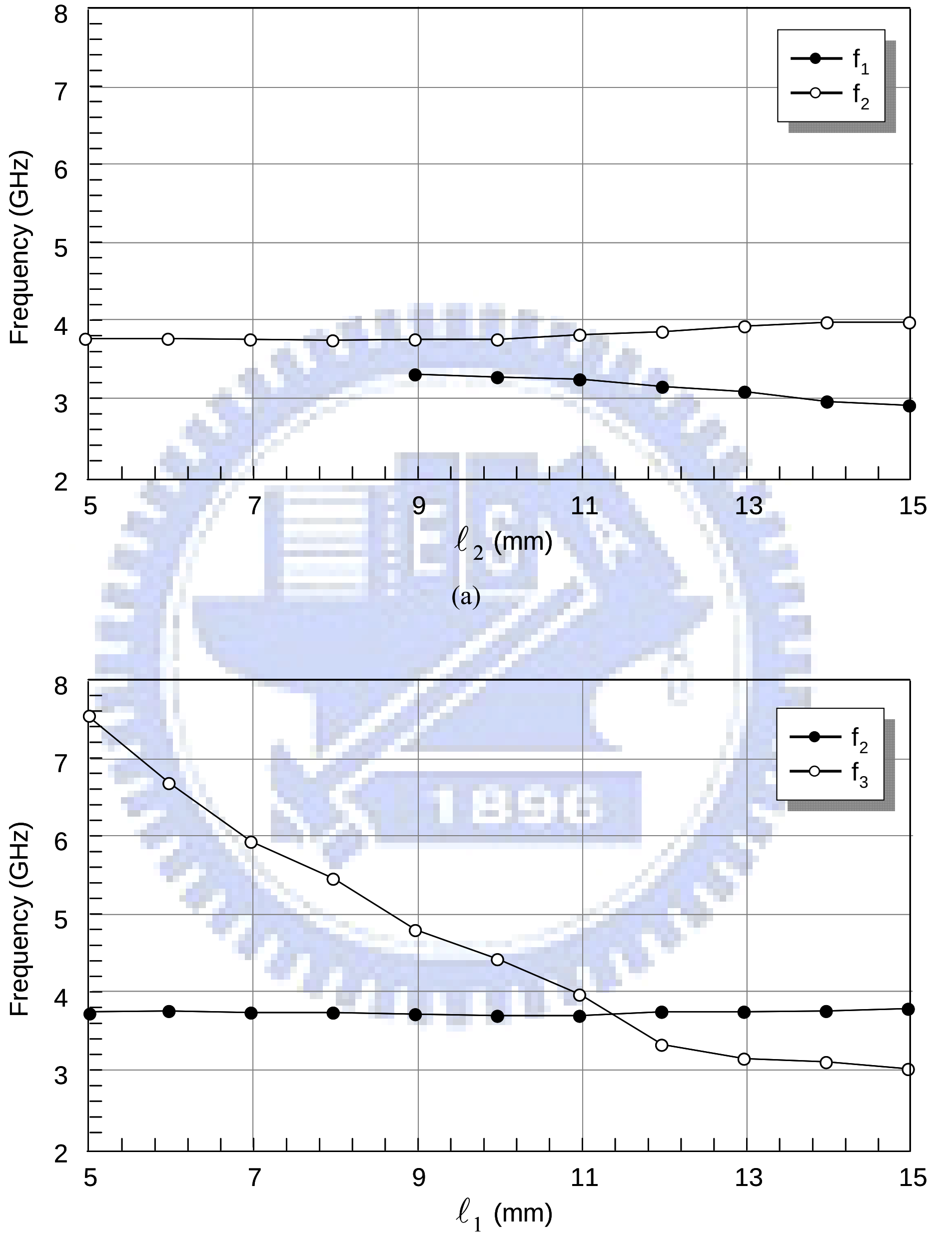

(a)

(b)

Figure 4.4 The effect on the resonance frequencies with various slit length of (a) ℓ_2 and (b) ℓ_1.

Figure 4.5 (a)-(c) shows the surface current distribution at 3.19, 3.71, and 4.41 GHz to illustrate the wideband mechanism, respectively. As seen in Figure 4.5 (a) at lower frequency region, the primary current mainly concentrated and flow through the left side of the patch then surrounding the left side slit. Hence, the increase of the length would alter the current distribution condition. Notably, the first resonant frequency decreases quite obviously as the increase of the length ℓ_2 (shows in Figure 4.4(a)). Moreover, the current direction of the feed strip and shorting strip are the same, hence, the proposed has stronger vertical polarization field as compared to the conventional printed antenna. And, the antenna radiation pattern is omnidirectional in the *xy*-plane (see Figure 4.17 (a)).

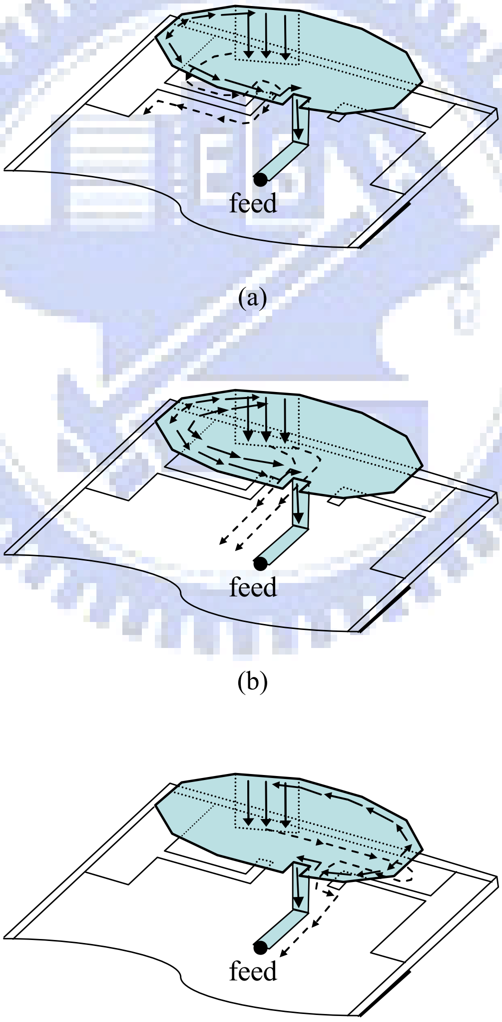

(a)

(b)

(c)

Figure 4.5 Simulated current distributions of the proposed antenna at (a) 3.19, (b) 3.71, and (c) 4.41GHz.

As for the third resonant frequency (4.41 GHz), as shown in Figure 4.5 (c), the primary antenna current mainly distributed on the right side of the patch and flow through the right side slit which arranged on the ground plane. Hence, the increase of the length ℓ_1 would alter the third resonance frequency. It is verified with Figure 4.4 (b), the third resonant frequency decreases quite obviously as the increase of the length ℓ_1. Similarly, both feed and shorting strip have the same current direction. Finally, for the second resonant frequency of 3.71 GHz, the current on the ground plane through pass the space between two slits immediately, thus, however the slit length varied, the second resonance frequency has slightly changed. Hence, by comparing Figure 4.4 and Figure 4.5, it can be summarized that, the first and third resonance frequency is controlled by the slit embedded on the left side and right side of the ground plane, respectively.

The effect of the position of the feed strip on antenna performance is investigated. All of the antenna dimensions are fixed, except for the feed strip position s relative to the antenna patch side wall. Figure 4.6 shows the simulated return loss for the proposed antenna of various feed positions s. It is clear that, the change of the feed position influences the impedance matching of the antenna, mainly at the second and third resonance frequencies. When the feed strip moves along the x direction (i.e., aparting from the right side of the ground plane) the input impedance matching becomes better. The input impedance can be improved when properly choosing the feed position s especially at high band. The widest bandwidth can be obtained when the $s = 6.75$ mm.

Figure 4.7 depicts the results of varying the feed depth d (0, 2.5, 5, 7.5 mm). When $d = 0$ mm, indicating that the feed strip is located on the patch edge. It can be seen that, the variation of the feed depth mainly influences the input impedance of the antenna. When d increases, the input matching becomes better, expect the case of $d > 7.5$ mm. In the case of $d = 7.5$ mm as shown in Figure 4.7, it is obvious that, the antenna performance becomes dual-band operating. The reasons is that, when a deeper feed strip insert to the patch, the current distribution on the patch can provide two current flow paths. One is mainly toward the right side of the patch. The other one enters the left side of the patch and then result in a dual-band operation.

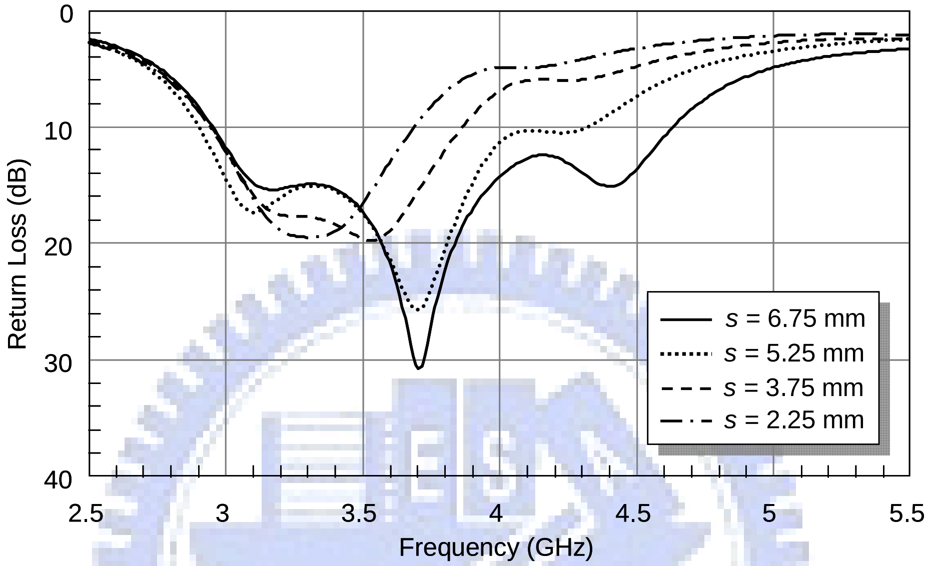

Figure 4.6 Simulated return loss for the proposed antenna of various feed position *s*. Other geometric parameters are the same as given in Figure 4.2.

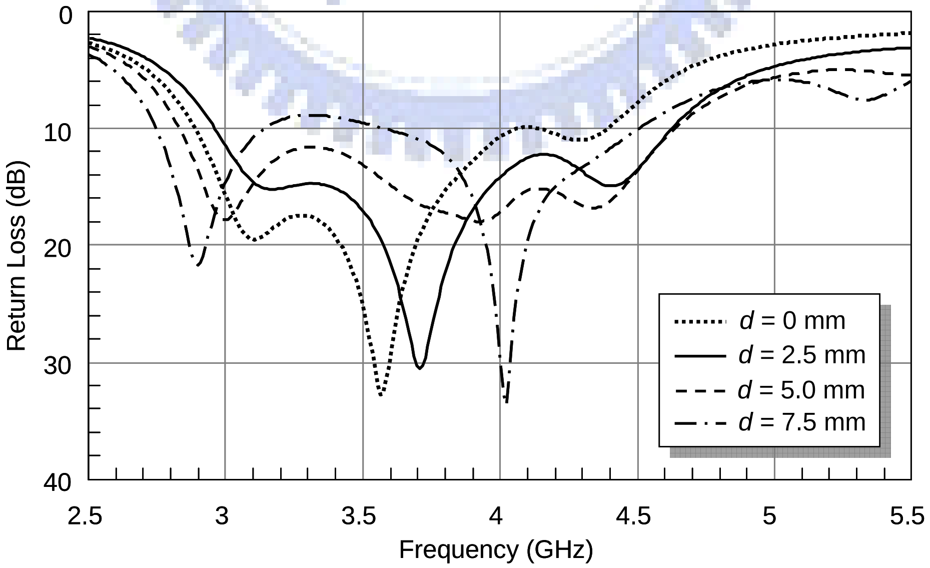

Figure 4.7 Simulated return loss for the proposed antenna of various feed depth *d*. Other geometric parameters are the same as given in Figure 4.2.

Figure 4.8 shows the effect of the position of the short strip on antenna performance. As show in Figure 4.8, there are four position of the shorting strip arrangement from p_1 to p_4. At the position p_1, there are two resonance frequencies at 3.25 and 4.4 GHz. When the shorting strip moves to the position p_3, two resonance frequencies occur at 3.05 and 3.89 GHz. But there is only one resonance frequency at 3.13 GHz while the shorting strip moves to the position p_4. It indicates that by properly choosing the position, the antenna structure can provide appropriate current distribution across full band. Thus the three resonance modes can be effectively excited and better input impedance matching can be achieved over the whole frequency band.

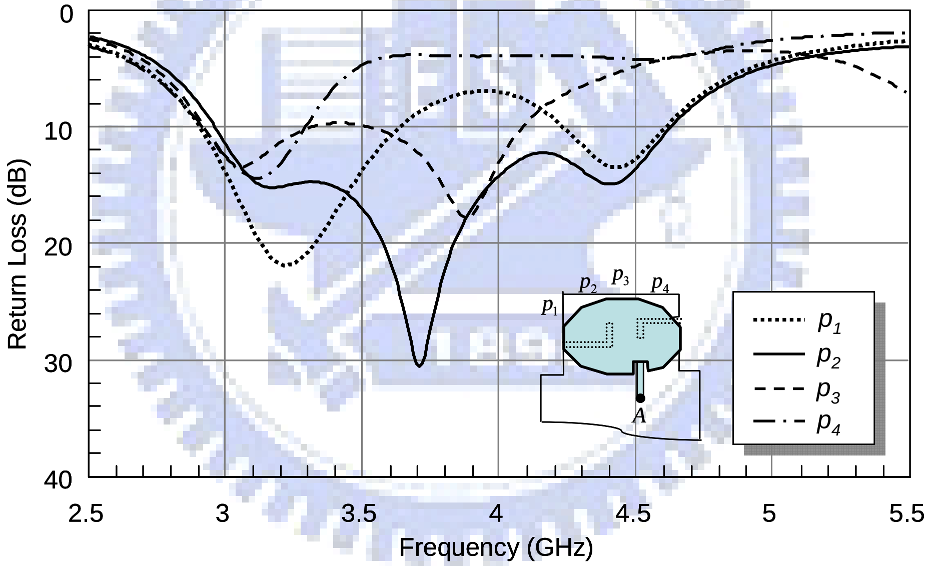

Figure 4.8 Simulated return loss for the proposed antenna of various short position. Other geometric parameters are the same as given in Figure 4.2.

Figure 4.9 shows the results of varying the shorting strip width w_s from 2.85 to 5.85 mm step 1 mm. As the simulated result in Figure 4.9, the change of the width mainly affects the impedance matching of the antenna. The decreasing of the second and third resonant frequency, as the width reduced, which is due to the increase of the equivalent current path, causing the resonance frequency moving toward the low frequency. As refer to the current distributions shown in Figure 4.5, the shorting strip has strong current magnitude at the second frequency than the other two frequencies. Thus, changing the shorting strip width influences the antenna performance obviously, especially at the second resonance frequency. Properly selecting the shorting width can lead to a largest high band edge and thus a widest impedance bandwidth.

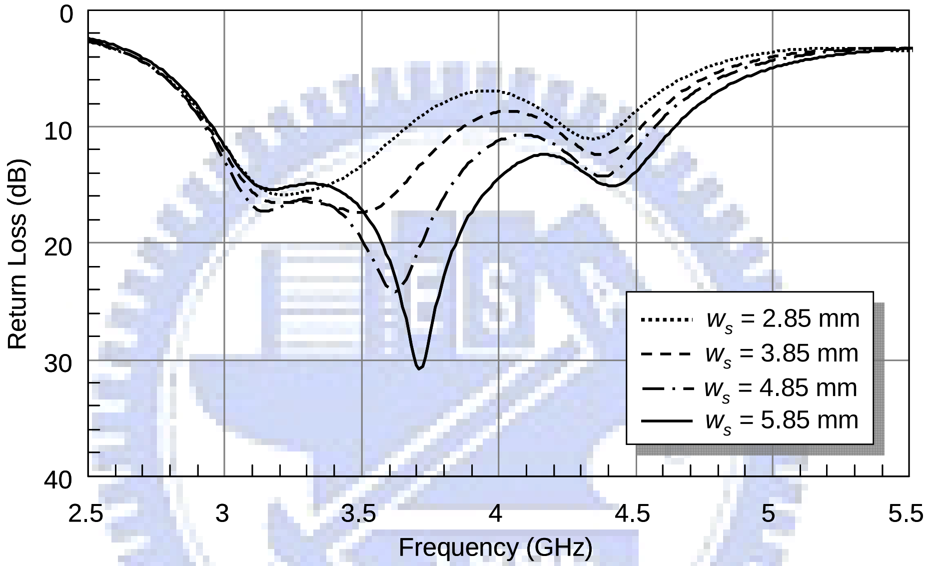

Figure 4.9 Simulated return loss for the proposed antenna of various shorting strip width w_s. Other geometric parameters are the same as given in Figure 4.2.

Figure 4.10 shows that the results of varying the antenna height *h* from 4 to 7 mm step 1 mm. As the simulated result in Figure 4.10, the change of the height mainly affects the impedance matching of the antenna, especially the third resonant frequency. It has been observed from the simulation result that the input reactance of the third resonant frequency with h = 4 mm is capacitive. Increasing the antenna height would lengthen the feed strip, thus the input inductance is increased. As a result, a larger antenna height *h* is associated with better input matching.

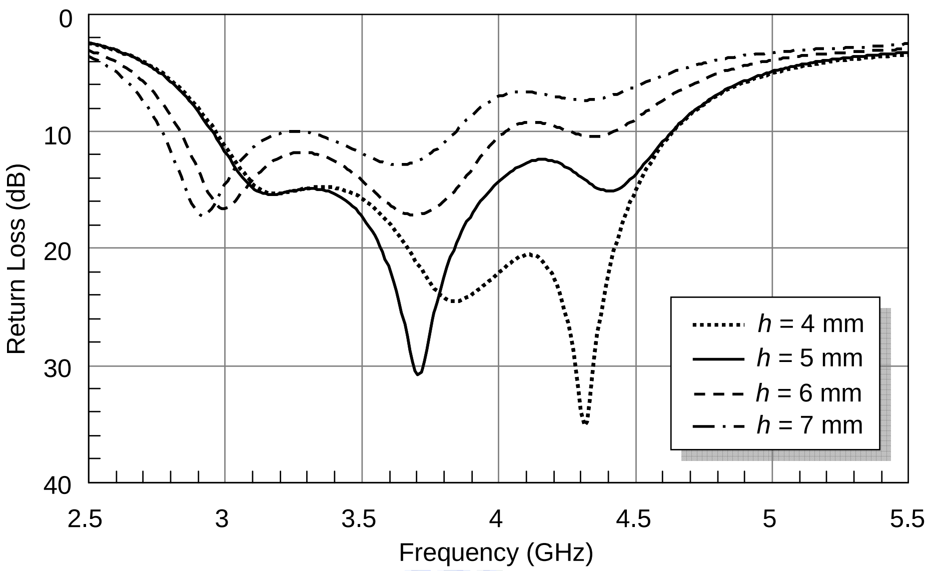

Figure 4.10 Simulated return loss for the proposed antenna of various antenna height *h*. Other geometric parameters are the same as given in Figure 4.2.

4.2 Metal Body Effect Analysis

The antenna performance is affected by the operating environment, especially when metal bodies are nearby the antenna. In actual application environment, the antenna might be placed parallel above a metal body such as metal-like table, PC case or placed near the LCD screen edges, inserted inside a laptop, and so on. In these cases, when the antenna is operating, fringing fields are expected to be present externally; thus, coupling between the antenna and the nearby associated elements (e.g., a metal-like table under the antenna) will occur. Moreover, the EM wave radiated from the antenna will induce currents on the metal bodies, which in turn will radiate back to the antenna and thus deteriorate the antenna function. With different height and position of the antenna above the metal bodies, the image current can procure constructed or destructed radiation, according to the phase relationship between antenna current and image current induced on the metal object. Thus the performance of the antenna will be quite different depending on the placement relative to the metal body. This possible coupling will then cause degradation effects on the antenna performances. Hence, in this section, the study on the antenna behavior when near a metal body is analyzed. A conventional printed UWB antenna is also simulated for comparison.

Figure 4.11 shows the side view of the low-profile UWB antenna placed parallel under a metal plane. In the simulation model, the metal plane whose size = 25 cm × 25 cm, the distance between the antenna and the metal plane is denoted as D. Figure 4.12 shows the simulated return losses for the proposed antenna above a metal plane of various distances between the antenna and the metal plane. In the case D = 0.5 cm, represents the distance between the antenna and metal plane almost nearby together. From Figure 4.12, it can be observed that, there still have three resonance frequencies, at the expense of little deterioration in impedance matching. When D is larger than 3 cm, the antenna performance is similar to the case without a metal plane under the antenna.

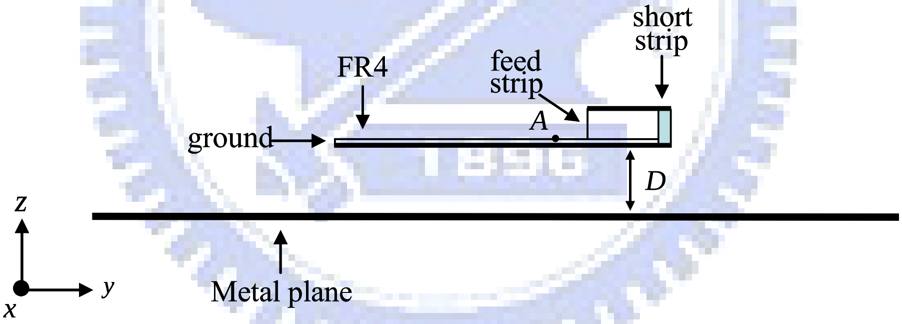

Figure 4.11 Side view of the low-profile UWB antenna placed parallel under a metal plane.

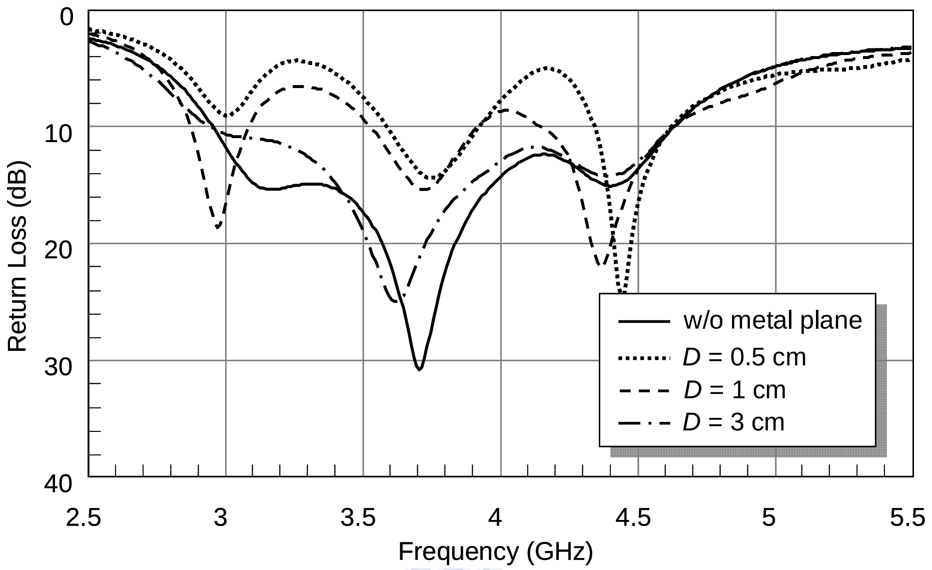

Figure 4.12 Simulated return losses for the proposed antenna above a metal plane of various distance *D*. Other geometric parameters are the same as given in Figure 4.2.

For comparison, a conventional printed UWB antenna is also investigated. In here, a half-circle monopole is used whose radius is 12 mm. Similarly, simulate the same arrangement as shown in Figure 4.11 and compare the antenna performance of the effect on the different antenna polarization above a metal plane. As the results in Figure 4.13, it can be seen that, in the case without metal plane, there are two resonance frequencies. But when *D* is less than 1 cm, the antenna resonance phenomenon is disappeared in low band region about 3.5 GHz. However, when *D* is larger than 3 cm, the antenna performance is similar to the case without a metal plane under the printed antenna.

Figure 4.14 shows the comparison of the radiation patterns with and without the metal plane which is 5 mm under the proposed antenna. In Figure 4.14 (a), show the simulated *xy*-plane radiation patterns without metal plane at 4.41 GHz. As refer to the current distributions show in Figure 4.5, because the current distributions has the same directional on both feed and shorting strip, thus provide the high vertical polarization field in *xy*-plane as shown in Figure 4.14. It can obviously see that, the E_θ are omnidirectional in *xy*-plane. When a metal plane is placed parallel under the proposed antenna, the simulated results are shown in the Figure 4.14 (b). The influence on the vertical polarization field is negligibly changed while adding the metal plane but the horizontal polarization field is almost deterioration. The reason is that, when a metal plane is placed parallel under the proposed antenna, it induces currents on the metal plane. By EM theory, the induced currents are equivalent to a parallel but out-of-phase image current on the other side of the metal plane and then degenerate the antenna performances. In here, the horizontal polarization field is reduced by the image current but the vertical polarization field is uninfluenced as compare in the Figure 4.14.

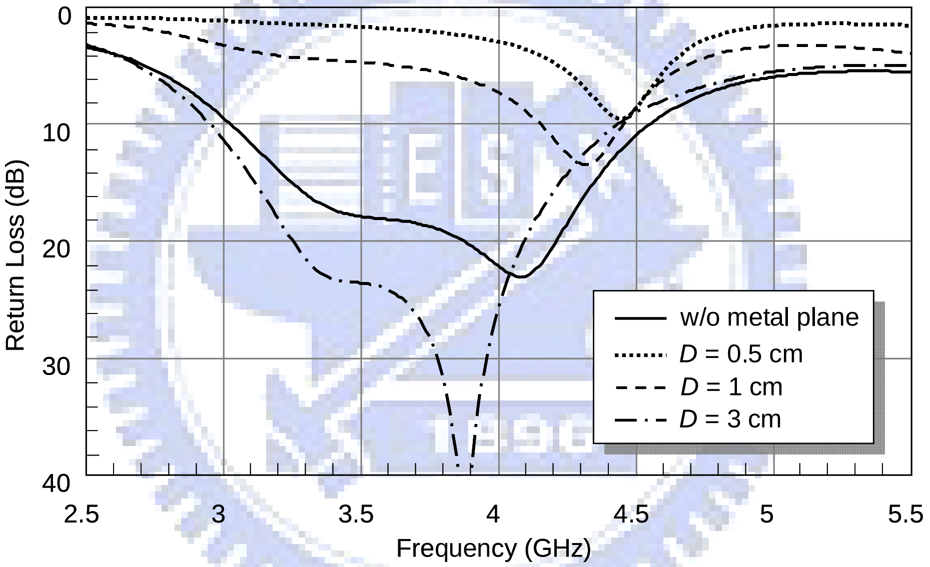

Figure 4.13 Simulated return losses for the reference antenna above a metal plane of various distance *D*.

Moreover, the low-profile UWB antenna is replaced a conventional printed UWB antenna and the same arrangement is placed as show in Figure 4.11. In Figure 4.15 (a), show the simulated *xy*-plane radiation patterns without metal plane of the printed antenna at 4.08 GHz. Because it's inherently printed structure, the dominated current is on the horizontal direction and thus stronger horizontal field but weaker vertical polarization field in *xy*-plane is obtained. Similarly, while the metal plane is adding under the printed antenna, by EM theory, the induced currents are equivalent to a parallel image current on the other side of the plane. It is noticeable that, the image current which induced on the plane has out-of-phase with the current on the printed antenna. As mentioned above, the printed antenna has high horizontal polarization field, hence, when a metal plane is placed parallel under the antenna closely. The current on the antenna will be canceled by the image current and produce destructed radiation. This phenomenon is shown in Figure 4.15 (b) and demonstrated from the simulated results. By comparing Figure 4.15 (a) and (b), it is obvious that, when a metal plane is placed parallel under the antenna, the horizontal polarization field is reduced strongly. However, because of the weaker vertical polarization field, whatever with or without the metal plane under the printed antenna, there is not significant influence in both situations.

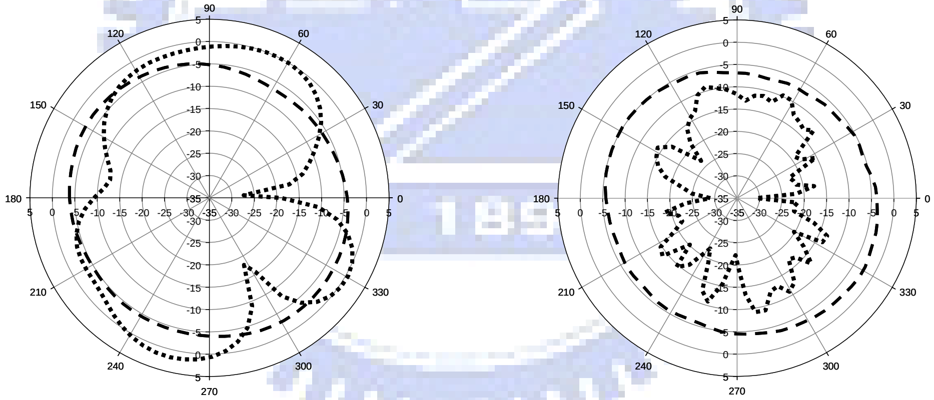

(a)

(b)

Figure 4.14 Simulated *xy*-plane radiation patterns without metal plane at (a) 4.41 GHz and with metal plane at (b) 4.45 GHz for the proposed antenna of $D = 0.5$ cm. (dashed line: E_θ dotted line: E_ϕ)

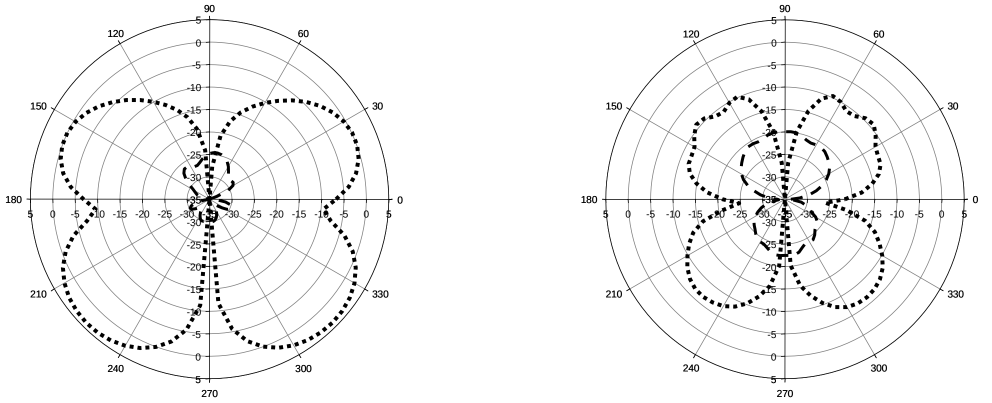

(a)

(b)

Figure 4.15 Simulated *xy*-plane radiation patterns without meta plane at (a) 4.08 GHz and with metal plane at (b) 4.45 GHz for the printed UWB antenna of $D = 0.5$ cm. (dashed line: E_θ dotted line: E_ϕ)

4.3 Experiment Results

Figure 4.16 shows the measured, as well as the simulated, return losses of the proposed antenna. The dimensions of the antenna are $w_a \times \ell_a$ = 25 mm × 17 mm, $W \times L$ = 34 mm × 75 mm, $w_1 \times \ell_1$ = 9 mm × 3 mm, $w_2 \times \ell_2$ = 9.5 mm × 4 mm, $w_3 \times \ell_3$ = 4.5 mm × 17 mm, w_s = 5.85 mm, h = 5mm, d = 2.5 mm, s = 6.75 mm, and g =1 mm. The measured impedance bandwidth, determined by a 10-dB return loss, is from 3.02 to 4.97 GHz, which is suitable for UWB low-band communication application. In Figure 4.16, it can be obviously seen that, the three resonant frequencies are located at 3.21, 3.74, and 4.65 GHz, very close to the simulated ones. The measured return losses for the proposed antenna above a metal plane of various distances between the antenna and the metal plane also show in Figure 4.16. It can be observed that, in the case D = 1 cm (dotted line), there still has three resonance frequencies, at the expense of little deterioration in impedance matching. When D = 3 cm (dash-dot line), the antenna performance is similar to the case without a metal plane under the antenna (solid line). Good agreement between the measured and simulated results is obtained.

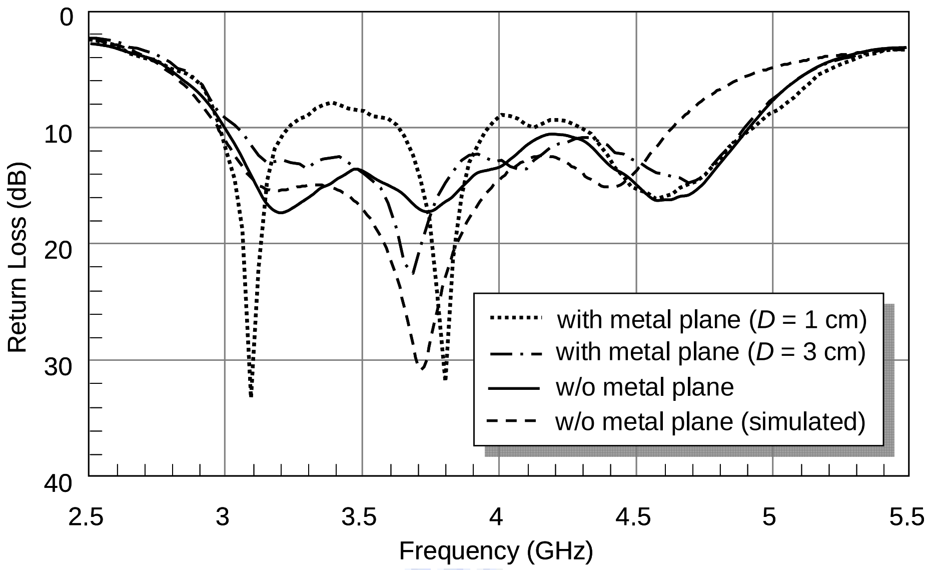

Figure 4.16 Measured and simulated return losses for proposed antenna with and without a metal plane.

Figure 4.17 (a) to (c) show the measured radiation patterns in the *xy*-plane at the three resonant frequencies (3.21, 3.74, and 4.64 GHz), respectively. The measured peak gains (average gains) are correspondingly 2.03 dBi (-1.10 dBi), 1.82 dBi (-0.64 dBi), and 2.34 dBi (-0.24 dBi) at the three frequencies, as summarized in Table 4.1. Figure 4.18 shows the measured peak gain from 3.1 to 5 GHz in the *xy*-plane. Across the impedance bandwidth, the curve is shown to be flat and the antenna gain varies from 1.56 to 3.95 dBi. Figure 4.19 shows the photograph of the accomplished antenna. The fabricated antenna with the dimension of 5 mm height, 25 mm width and 17mm length. It is mounted on the FR-4 substrate (ε_r = 4.4) with a thickness of 0.8 mm. The FR-4 substrate has a dimension of 34 mm × 75 mm, which is considered to be the ground plane of a practical application.

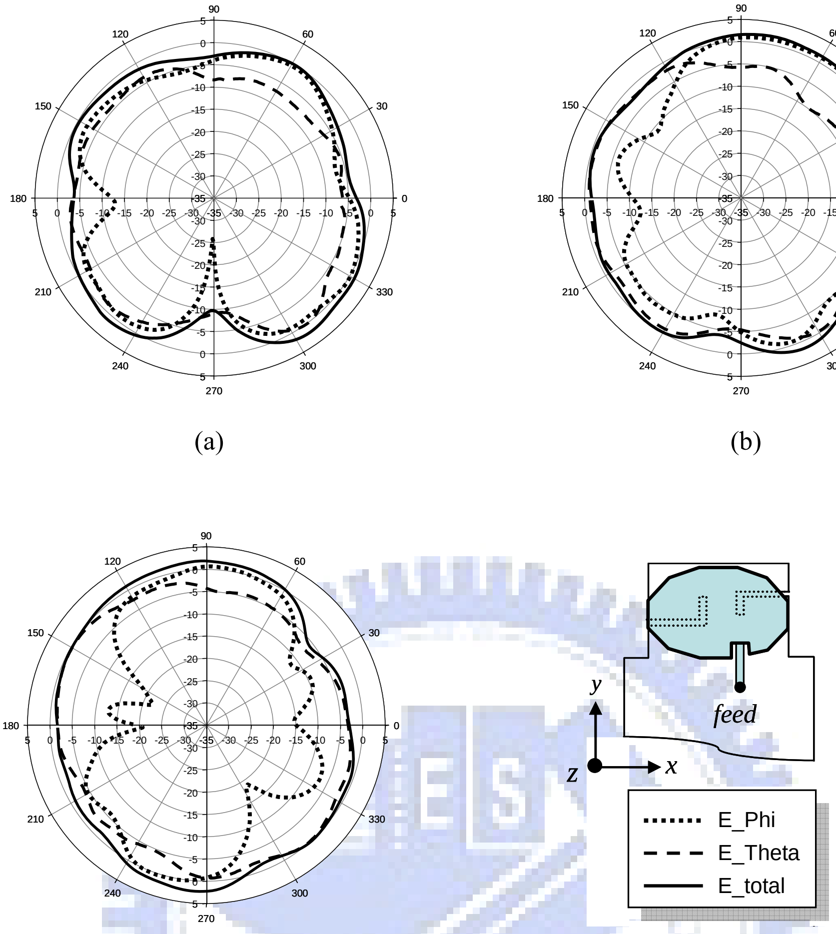

(a) (b)

(c)

Figure 4.17 Measured *xy*-plane radiation patterns at (a) 3.21 GHz, (b) 3.74 GHz and (c) 4.64 GHz for the proposed antenna.

Table 4.1

The Measured Peak and Average Gains at Three Resonant Frequencies

Frequency (GHz)	Peak gain (dBi)	Average gain (dBi)
3.21	2.03	-1.10
3.74	1.82	-0.64
4.64	2.34	-0.24

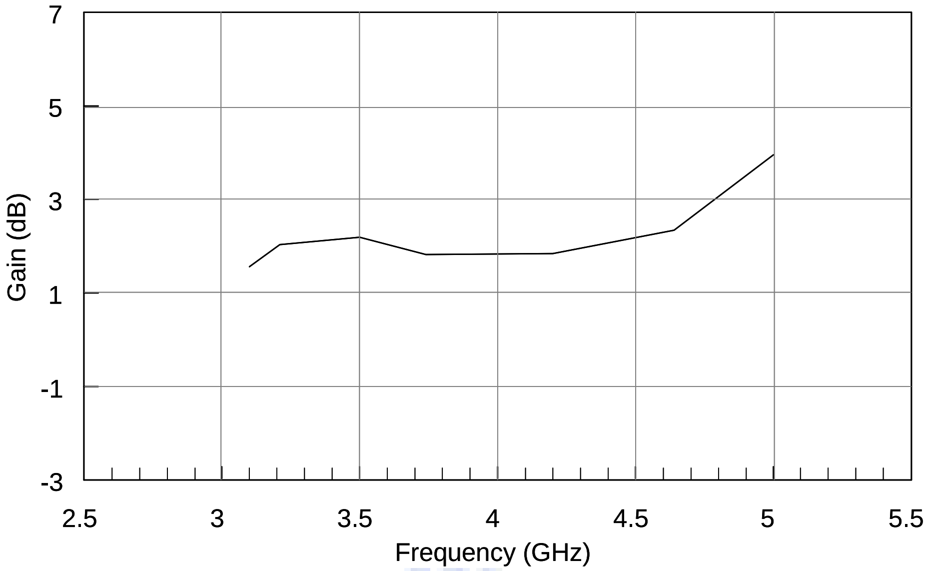

Figure 4.18 Measured peak gain of the proposed antenna at *xy*-plane.

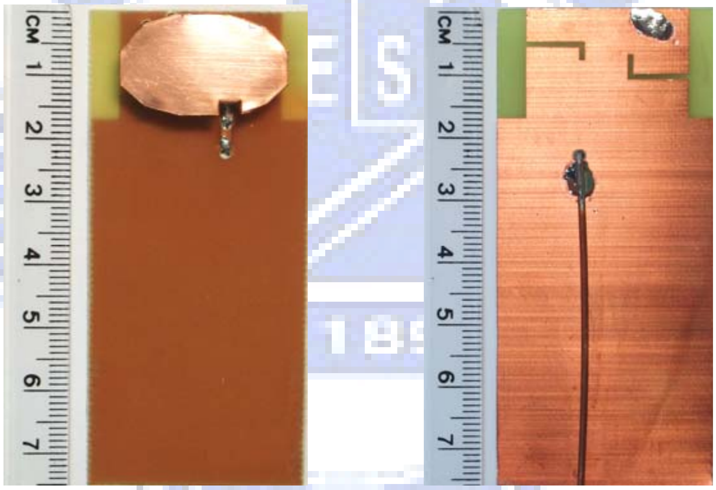

(a) (b)

Figure 4.19 The photographs of the fabricated antenna. (a) Front view and (b) back view.

4.4 Summary

A low-profile UWB antenna with strong vertically field has been proposed and investigated. From the simulated results, it has been demonstrated that the embedded L-shaped slits in the proposed antenna structure provide additional resonance frequencies, which leads to the appearance of three continuous resonant modes and thus yields to the ultra-wideband performance. Moreover, because of the current flow on the feed and shorting strip has the same direction and thus high vertical polarization field as compared to the conventional printed antenna at *xy*-plane can be obtained. In actual operating environment, even when a metal plane placed parallel nearby and under the antenna, the proposed antenna still maintained good radiation characteristics. Finally, the measured results agree well with the simulation ones, a 10-dB return loss fractional bandwidth of 48.81% from 3.02 to 4.97 GHz. Good gain flatness with a maximum variation of 1.39 dB is observed over the entire frequency band. The proposed antenna has a compact size of 25 mm × 17 mm and low-profile of 5 mm, which is suitable for DS-UWB low-band communication applications.

Chapter 5

Analysis and Application of an On-Package Planar Inverted-F Antenna

In this chapter, a miniaturized on-package planar inverted-F antenna (PIFA) is proposed for high integration module application. The on-package PIFA consists of a single folded metal plate and has several advantages, including small size, light weight, low-cost and ease of fabrication. The antenna radiation pattern is omnidirectional in the H-plane. The coupling effect between the on-package PIFA and the RF components in the shielding package was studied. The antenna performance rarely changes and the isolation between the antenna and the RF components can be maximized when the locations of the components are appropriately arranged in the package. Finally, a wireless local area network (WLAN) front-end module (FEM) including the switch, low-pass filter (LPF), band-pass filter (BPF) and power amplifier (PA), is embedded into the shielding package of the antenna. The Error Vector Magnitude (EVM) of the resultant antenna integrated FEM, together with a WLAN card containing the baseband/medium access control (MAC) circuitry, is tested. Good performance is obtained, showing the usability of the proposed antenna configuration.

5.1 Configuration and Design

In this study, the PIFA is integrated with a package using a single folded metal plate. Since the antenna is to satisfy the specification of IEEE 802.11b/g WLAN, the required return loss bandwidth should cover the band 2.4-2.4835 GHz. The on-package PIFA is implemented on the FR4 substrate, whose dielectric constant is 4.4, loss tangent is 0.02, and thickness is 0.8 mm.

Figure 5.1 shows the 3-D structure and side views of the on-package PIFA. The length and width of the on-package PIFA determine the resonant frequency, which is approximated by the formula

$$f_0 = \frac{c}{4(w_a + \ell_a)} \tag{5.1}$$

where c is the velocity of light; ℓ_a and w_a are the length and width of the radiating element, and f_0 is the resonant frequency. The radiating element is connected to the ground by using a short-circuit strip located near the antenna's feed strip. Equation (5.1) yields the patch size of the antenna $\ell_a \times w_a$ = 14.5 mm × 15 mm and an overall physical length of approximately one quarter-wavelength at the desired frequency of 2.45 GHz. The size of the shielding package is $\ell_p \times w_p \times h$ and the ground size is $W \times L$. The feed point is denoted as point A as shown in Figure 5.1.

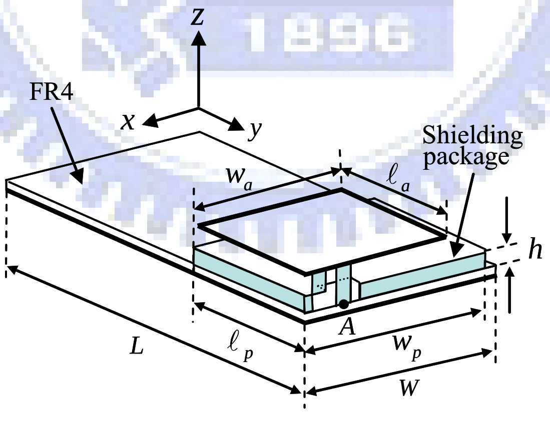

(a)

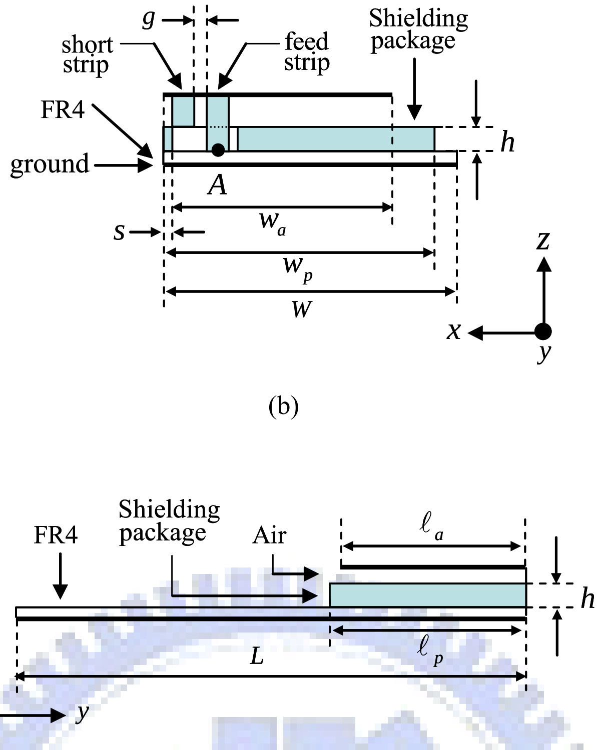

(b)

(c)

Figure 5.1 Geometry of the on-package PIFA. (a) 3-D structure, (b) side view of *xz*-plane, (c) side view of *yz*-plane.

The antenna is integrated with the shielding package using a single folded metal plate. The shorting strip is located at the corner of the patch and the feed of the on-package PIFA is located at the edge of the shielding package. The width and height of the shorting strip are 1.5 and 2 mm, respectively, while those of the feed strip are 1.5 and 3.5 mm, respectively. The input impedance of the antenna can be easily matched to 50Ω by controlling the feed position relative to the shorting strip. The proposed antenna structure is simulated using HFSS, a commercial 3-D full-wave electromagnetic (EM) simulation software. Figure 5.2 shows the return losses with various gap widths g between the shorting strip and the feed strip. The dimensions of the radiating element, the shorting strip, and the feed strip are fixed. The ground size and shielding package sizes are also specified as $W \times L$ = 20 mm × 40 mm and $w_p \times \ell_p$ = 20 mm × 15 mm, respectively. When the gap width g is smaller, input impedance matching can be improved. However, an extremely small gap width cannot be realized practically. Thus, the restriction of the fabrication technology must be considered and then the gap between the shorting strip and the feed strip chosen as g = 1 mm.

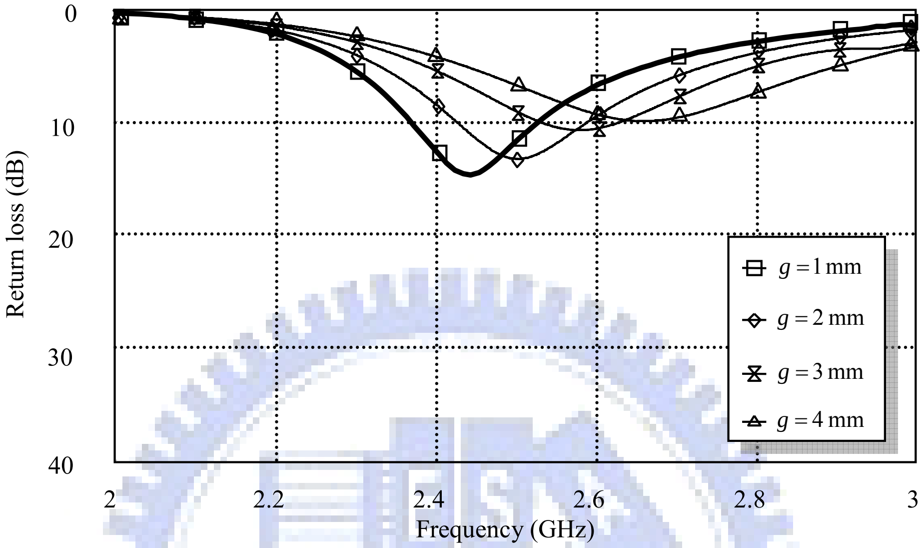

Figure 5.2 Return loss of on-package PIFA with various gap widths between the shorting strip and the feed strip; $\ell_a \times w_a$ = 14.5 mm × 15 mm, $\ell_p \times w_p$ = 15 mm × 20 mm, $W \times L$ = 20 mm × 40 mm, h = 1.5 mm, and s = 0 mm.

The effect of the position of the shorting strip on antenna performance is investigated. All of the antenna dimensions are fixed, except for the shorting strip position s relative to the shielding package side wall. The center frequency increases as the shorting strip moves along the $-x$ direction (i.e., becoming farther from the side wall), because the equivalent current length decrease as s increases. In Figure 5.3, the impedance bandwidth exceeds that required for the IEEE 802.11b/g WLAN band application when s is 0 mm. Furthermore, the shorting strip is located at the corner of the shielding package, indicating that the feed strip is adjacent to the shielding package side wall. Accordingly, the vertical current on the feed strip would not readily excite the cavity mode in the shielding package. Another advantage is that the size is small for a given operating frequency.

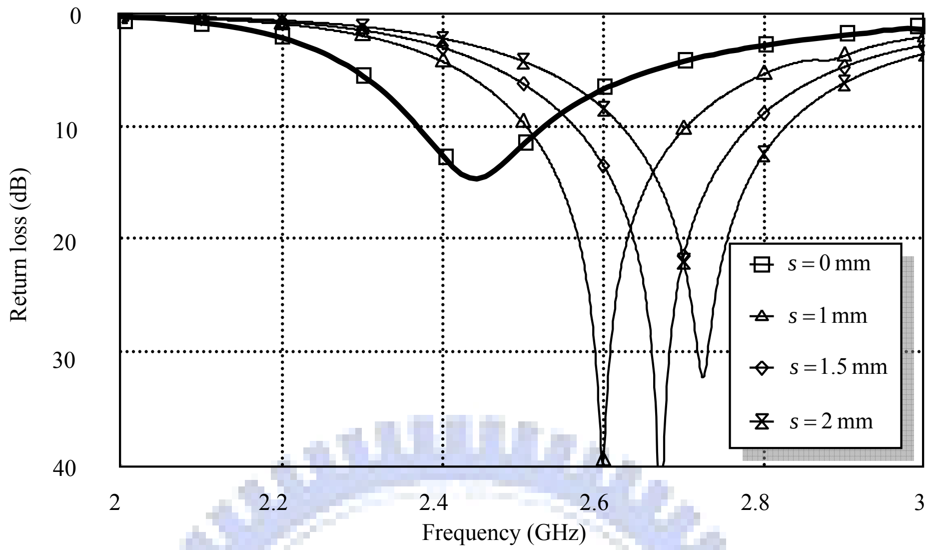

Figure 5.3 Return loss of on-package PIFA with various shorting strip positions. Other geometric parameters are the same as given in Figure 5.2.

The RF components can be placed within the shielding package and the baseband circuits arranged outside. The ground size and shielding package change with the size of the circuitry. However, the ground size influences the antenna performance and the shielding package is one part of the on-package PIFA. Therefore, changing the ground size and the shielding package affects the characteristics of the on-package PIFA. Hence, it is interesting to see the effect of varying the shielding package and the ground length.

Figure 5.4 shows the simulated return losses for various shielding package sizes, including $w_p \times \ell_p$ = 15 mm × 15 mm (case 1), 20 mm × 20 mm (case 2), and 20 mm × 25 mm (case 3). The result for the original package size (15 mm × 20 mm) is also shown for comparison. Basically, the antenna frequency is little changed due to the variation of the package size. The bandwidth of case 1 exceeds the original, but those in the other two cases are worse.

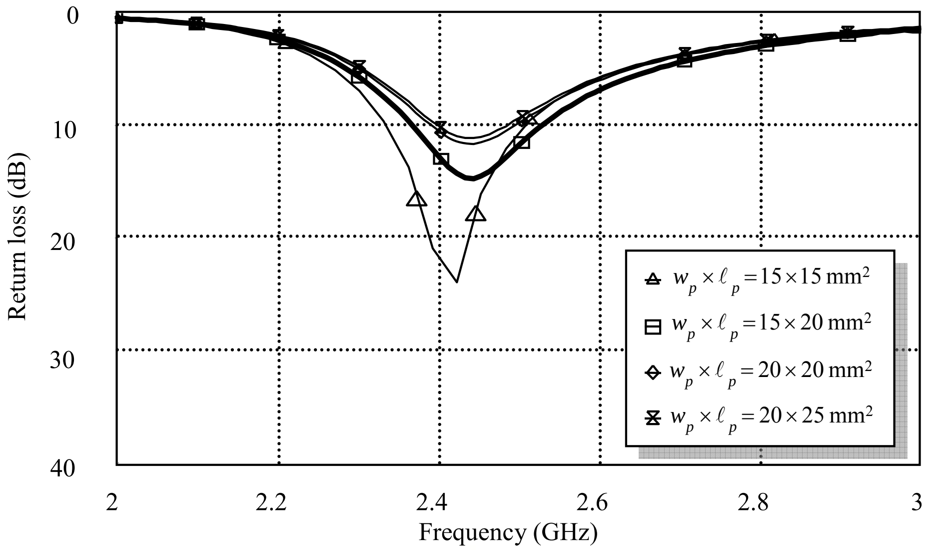

Figure 5.4 Return loss of on-package PIFA with various shielding package sizes. Other geometric parameters are the same as given in Figure 5.2.

The other parameter of shielding package is the package height. Figure 5.5 shows the effect of the package height h on the return loss, with h = 1.5, 2, 2.5, and 3 mm. The input impedance bandwidth is rarely changes with the package height, and the input impedance matching is improved when the package height h exceeds the original value (h = 1.5 mm). It has been observed from the simulation result that, the input reactance of the on-package PIFA with h = 1.5 mm is capacitive. Increasing the package height would lengthen the feed strip, thus increasing the input inductance. Therefore, a larger package height h is associated with better input matching. Hence, the proposed on-package PIFA is appropriate for RF components of various height without redesign when the package height h is increased from 1.5 to 3 mm.

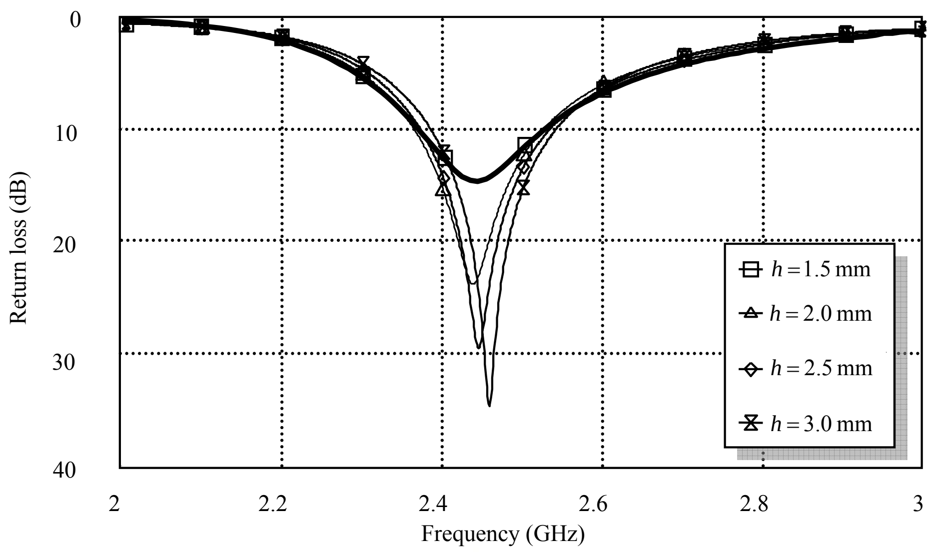

Figure 5.5 Return loss of on-package PIFA with various shielding package heights. Other geometric parameters are the same as given in Figure 5.2.

The effect of ground length is also examined. The ground width *W* is fixed to 20 mm and the ground length *L* varied among 35 mm, 45 mm, and 50 mm. Figure 5.6 shows the input return loss in each case. It is seen that the return loss at ground length of 35 mm is much poor, due to the truncation of the induced ground current.

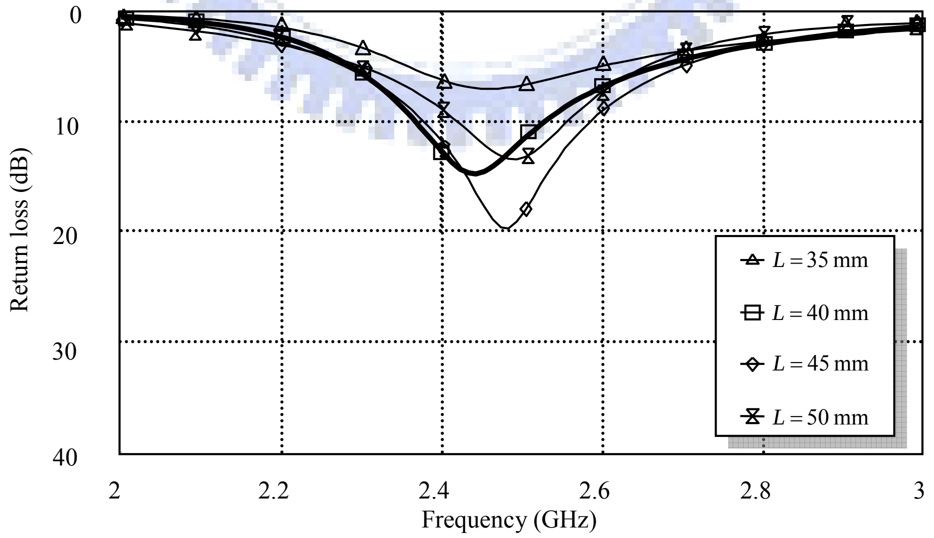

Figure 5.6 Return loss of on-package PIFA with various ground lengths. Other geometric parameters are the same as given in Figure 5.2.

As mentioned earlier, the proposed antenna structure can be made using a single metal sheet. As illustrated in Figure 5.7, first, trim the shape of the on-package PIFA and bend downward three sides of the shielding package except the one nearby the feed strip. Then bend upward the antenna patch, followed by bending the last side of the package. To keep the spacing between the antenna patch and the shielding package so as to remain the antenna performance, a low-loss foam with relative dielectric constant near 1.0 can be inserted in between. Figure 5.8 compares the simulated and measured input return losses of the proposed antenna for package and ground sizes of $\ell_p \times w_p \times h$ = 15 mm × 20 mm × 1.5 mm and $W \times L$ = 20 mm × 40 mm, respectively. A total impedance bandwidth of 160 MHz from 2.37 to 2.53 GHz is measured. Good agreement between the measured and simulated results is obtained.

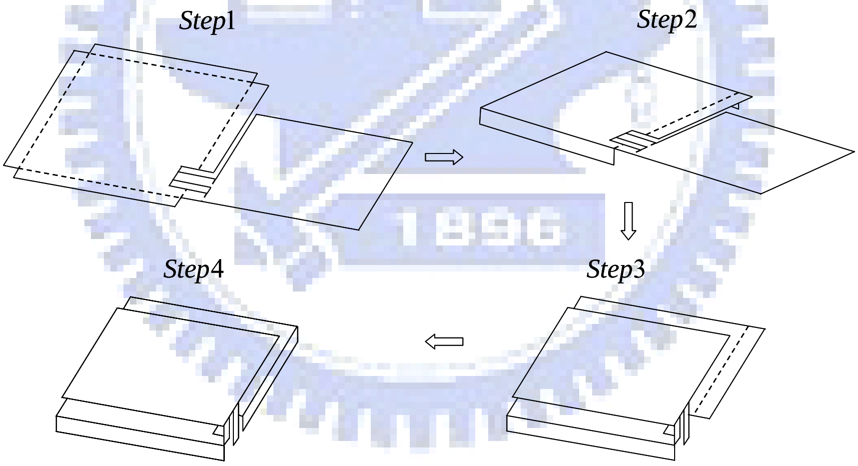

Figure 5.7 Manufacture procedure of on-package PIFA.

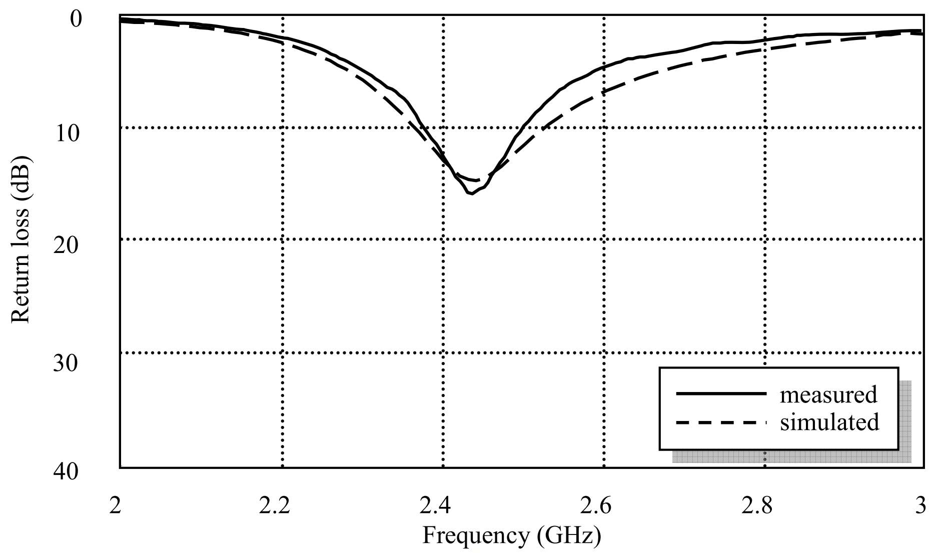

Figure 5.8 Measured and simulated return loss of on-package PIFA. $\ell_a \times w_a$ = 14.5 mm × 15 mm, $\ell_p \times w_p$ = 15 mm × 20 mm, $W \times L$ = 20 mm × 40 mm, h = 1.5 mm, g = 1 mm, and s = 0 mm.

5.2 Coupling Between On-Package PIFA and RF Components

The vertical current on the feed strip of the on-package PIFA would radiate field into the shielding package through the aperture on the package's side wall. This might induce the coupling between the antenna and the RF components embedded in the package. It is thus interesting to check the coupling level between the on-package PIFA and the components. Essentially, the RF circuitry comprises a T/R switch, filters, a PA, and a RF transceivers [86]-[89]. Here, for simplicity, an LTCC BPF is adopted to represent a typical RF component. Since the layout of the LTCC BPF formed with inductors and capacitors was known, it is thus possible to analyze the coupling effect using the EM software HFSS.

The BPF with size of 2.5 mm × 2.0 mm × 1 mm is arranged at six locations (denoted from A to F) inside the package as shown in Figure 5.9. Ports 1 and 2 are the input and output ports of the BPF, while port 3 represents the input port of the on-package PIFA. Locations E and F are at the same position, but with the BPF rotated 90 degree. Figure 5.10 (a) shows the simulation return loss ($-S_{11}$) and insertion loss ($-S_{21}$)

of the BPF at various locations. The results for the BPF without the package are also shown for comparison. It is seen that the performance of the BPF is not changed with the location. The insertion loss in the passband keeps under 2 dB. Figure 5.10 (b) and (c) depict the simulation isolations ($-S_{13}$ and $-S_{23}$) between the antenna port and the two BPF ports. First of all, it is seen that the isolations are all better than 30 dB in the passband. This high isolation level benefits the avoidance of signal oscillation, especially when a high-gain amplifier is embedded in the package. More close observation reveals that as the component is placed in front of the antenna port (location A), the coupling is highest. When the component is moved to the far end, such as locations C and D, the isolation can be greatly improved to be better than 45 dB in the passband. Although not shown here, it has been checked that the return loss response of the on-package PIFA has no change due to the placement of the BPF.

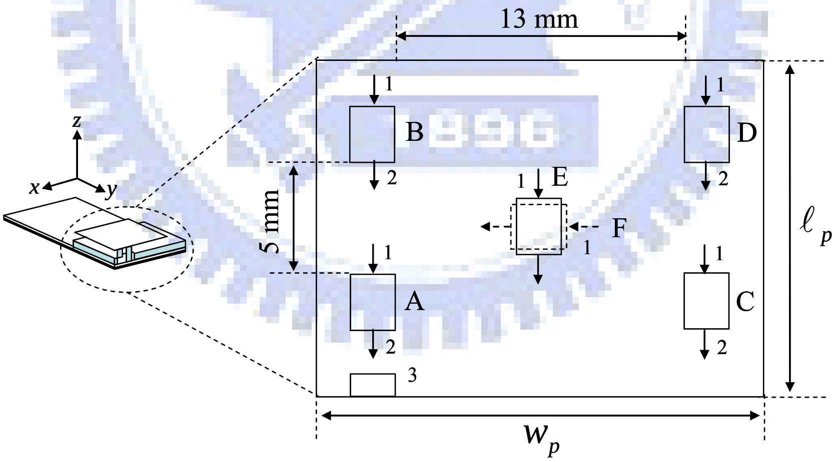

Figure 5.9 Illustration of BPF locations. $\ell_p \times w_p$ = 15 mm × 20 mm

With the BPF placed at location B and the output port connected to the input of the on-package PIFA through a 50 Ω microstrip line, a one-port antenna with BPF integrated is obtained. Figure 5.11 illustrates its simulated and measured return losses as functions of frequency. Both curves well agree to each other and have three poles, two from the BPF and one from the antenna. The measured radiation patterns at the three principal planes are presented in Figure 5.12. Those of the antenna without the BPF are also shown for comparison. The patterns are quite omni-directional, especially in the *xz*-plane. The peak gains (average gains) for the BFP integrated antenna are -1.34 (-3.38), 1.68 (-5.30), and -1.30 (-5.12) dBi in the *xz*, *yz*, and *xy*-planes, respectively. Due to the insertion loss of the BPF, the gains are about 2 dB lower than those of the antenna without BPF embedded.

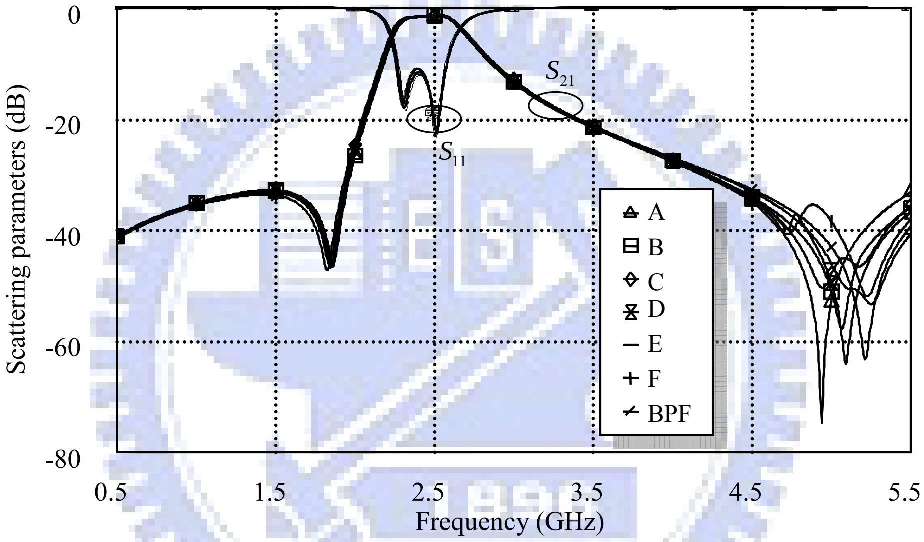

(a)

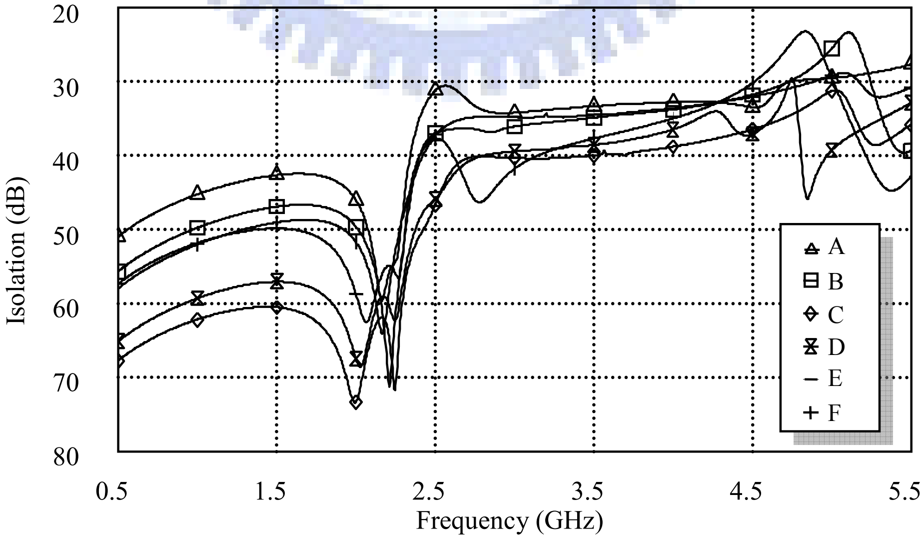

(b)

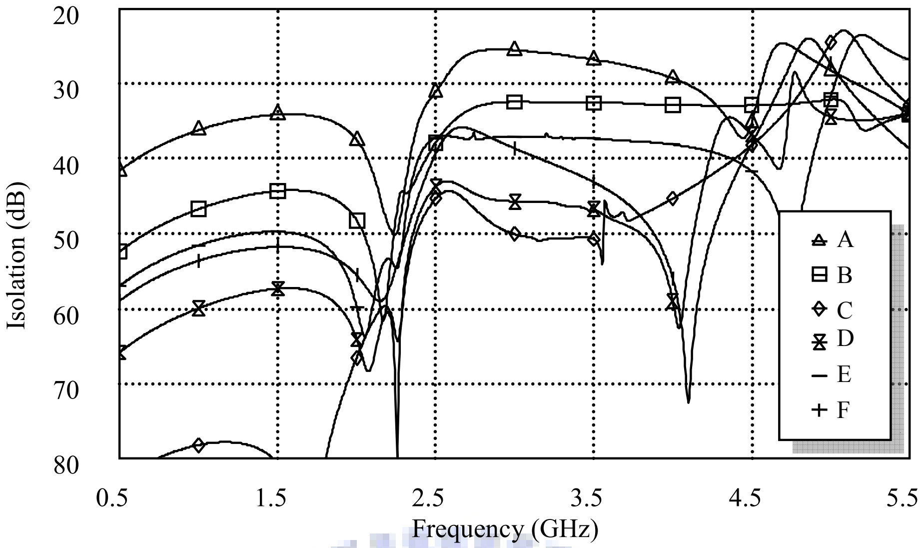

(c)

Figure 5.10 Simulation results of the scattering parameters with BPF at various locations. (a) Return loss ($-S_{11}$) and insertion loss ($-S_{21}$) of the BPF, (b) isolation ($-S_{13}$) between ports 1 and 3, and (c) isolation ($-S_{23}$) between ports 2 and 3. The geometrical parameters are the same as given in Figure 5.8.

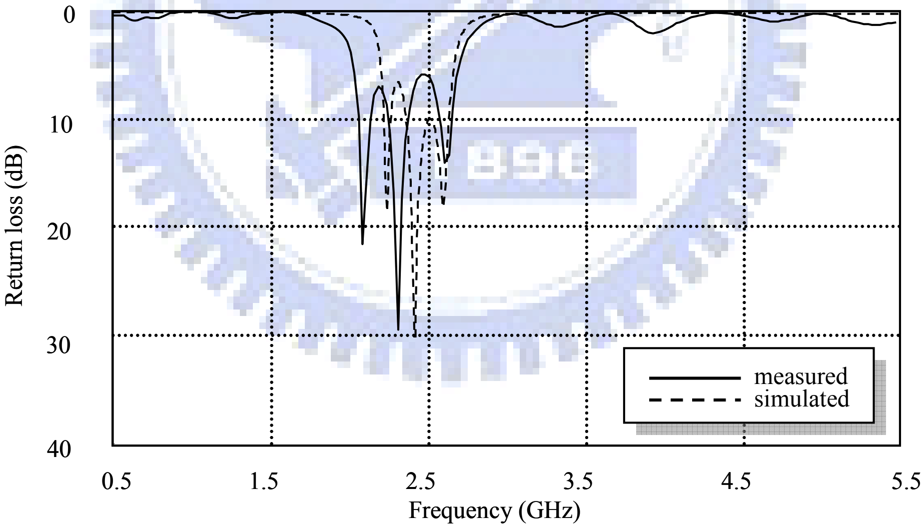

Figure 5.11 Return loss of the on-package PIFA with BPF integrated. The geometric parameters are the same as given in Figure 5.8.

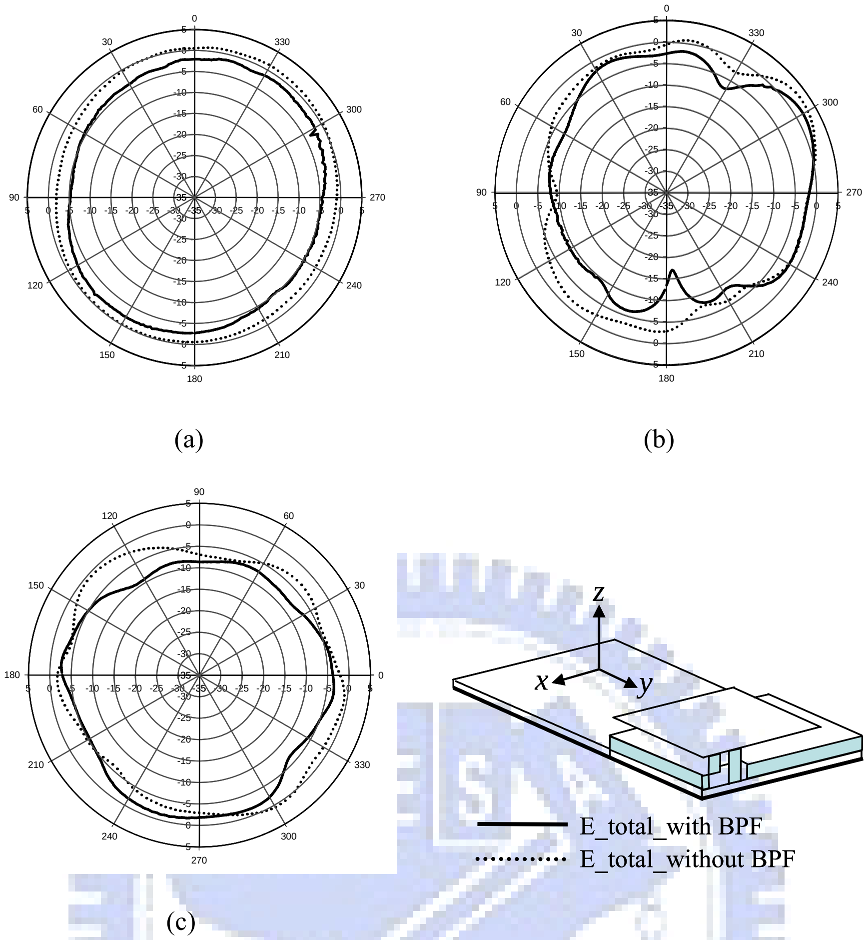

(a) (b)

(c)

Figure 5.12 Radiation patterns of the on-package PIFA with and without BPF at 2.45GHz for (a) *xz*- plane, (b) *yz*-plane, and (c) *xy*-plane. The geometric parameters are the same as given in Figure 5.8.

5.3 Integration of On-Package PIFA and WLAN Front-End Module

The designed on-package PIFA was integrated with the WLAN front-end module (FEM), forming an antenna embedded front-end module (AFEM). Figure 5.13 shows the block diagram of the module. The FEM includes a T/R switch (SW), an LTCC LPF, an LTCC BPF, and a PA. Table I lists the specifications of these RF components. The FEM was first built and measured. The results reveal that in the passband, the insertion loss on the RX path is 2.72 dB and the signal gain on the TX path is 25.83 dB. Both are chose to the ideal values (2.51 dB and 26.63 dB, respectively) calculated from Table 5.1. The fabricated FEM was placed inside the package of the antenna, with the switch output connected to the antenna input. To form a complete WLAN unit, we used cables to connect the TX and RX ports to a commercial WLAN card, which contains a RF transceiver and the baseband/MAC circuitry.

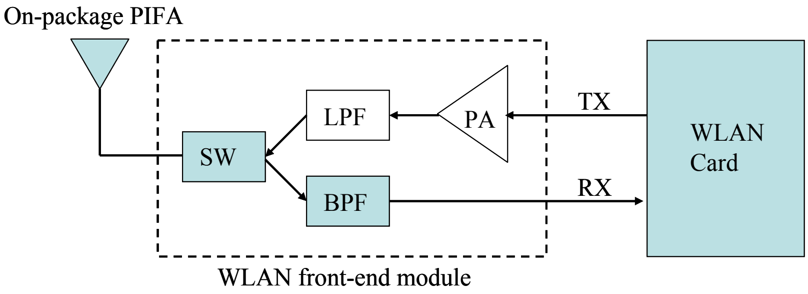

Figure 5.13 Block diagram of on-package PIFA integrated with WLAN front-end module and WLAN card.

Table 5.1

The Specifications of Each Component in the WLAN Front-end Module

	Return loss (dB)	Insertion loss/ Gain (dB)
SW	> 20	0.97
LPF	> 20	1.05
BPF	> 15	1.54
PA	> 10	28.65

Figure 5.14 (a)-(c) show the test results of the EVM and spectrum masks. The test distance is 3 m between the transmitter and the receiver antennas. The EVM is -30.99, -32.51, and -31.29 dB at 2.412, 2.442 and 2.472 GHz, respectively. All of these values are under -25 dB, which is the maximum EVM specified by the IEEE 802.11g. Also, the spectra are well controlled under the mask. Figure 5.15 shows the photograph of the circuit for testing.

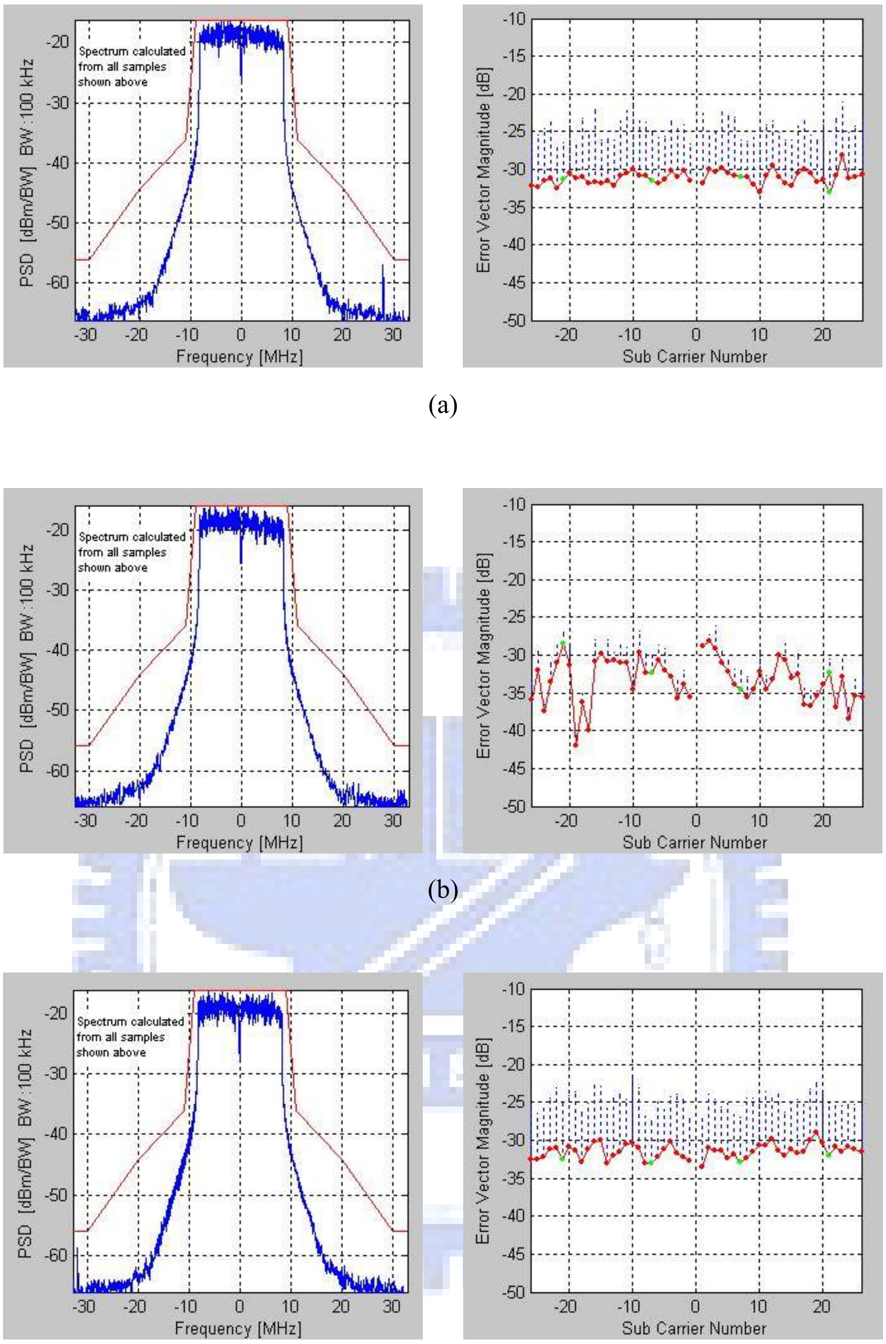

(a)

(b)

(c)

Figure 5.14 Test results of the EVM and spectrum masks at (a) 2.412 GHz, (b) 2.442 GHz, and (c) 2.472 GHz.

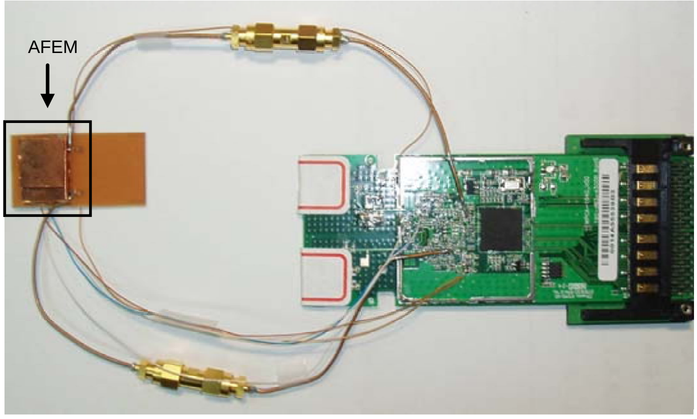

Figure 5.15 Photograph of the antenna embedded front-end module (AFEM) and a WLAN card.

5.4 Summary

An on-package PIFA made from a single folded metal plate for IEEE 802.11b/g WLAN band applications has been proposed and demonstrated. The prototype has a compact size of 15 mm × 20 mm × 3.5 mm. Several design parameters, such as the package dimensions and ground size, have been analyzed. The coupling between the antenna and the RF component embedded inside the package was studied. It has been found that high isolation can be obtained, especially when the components are placed away from the antenna input. An on-package PIFA integrated with a WLAN front-end module and a WLAN card was successfully implemented. Good agreement exists between the measured results and the ideal values. The EVM in the operating band is better than -30 dB, indicating the good performance of the architecture. From the tested result, it is seem that the on-package PIFA has good radiation characteristic and thus suitable for the WLAN communication applications.

Chapter 6

Conclusions and Suggestions for Future Works

A series of miniaturized antenna designs for UWB and high integration module application are designed and demonstrated in this dissertation. In this chapter, the distinguished results and conclusions are summarized. Several suggestions are also provided for the advanced research.

6.1 Conclusions

For developing the realizable miniaturized antenna designs, several technologies have been proposed in this dissertation. In Chapter 2, two planar UWB antenna designs are presented. First, by introducing the binomial function for characterized the edge curve of the antenna. Through the change with the different order of the binomial function and the gap width between the antenna and ground plane, the UWB (3.1-10.6 GHz) antenna can be achieved. A stable omnidirectional radiation pattern was also obtained for the whole impedance bandwidth. Besides, in order to obtain the band-notched function in the UWB antenna application, the concept of the parallel LC circuit is applied and proposed. At resonant frequency, the parallel LC circuit will cause high input impedance that leads to the desired high attenuation and impedance mismatching near the notch frequency. Hence, a parallel LC circuit formed by two T-shaped stubs inside an ellipse slot cut in the radiation patch and the elliptical slot, and the T-shaped stubs are equivalent to an inductor and a capacitor, respectively. By properly adjust the inductor and capacitor values, the notched band, covering the 5 GHz WiFi band, is obtained.

Chapter 3 presents a simple and compact monopole-like printed ultra-wideband antenna. The structure is quite simple and contains a conventional printed thin-wire monopole in addition to a quasi-transmission line section. The antenna is composed of a monopole section and a quasi-transmission line section. The input signal from the feed line first passes through the quasi-transmission line section then enters the monopole. The resonance mechanisms with four antenna resonances and the effect of the quasi-transmission line section on the antenna performance of the proposed ultra-wideband antenna are investigated. From the analyzed results, the quasi-transmission line section provides impedance matching or antenna radiation at different frequency bands. By properly designing the parameters of this quasi-transmission line section, several current resonances with continuous frequencies can happen in the antenna structure, which thus makes the whole antenna possessing wideband performance.

Furthermore, a low-profile UWB antenna with strong vertical field has been proposed and investigated in Chapter 4. According to embedded two L-shaped slits on the ground plane, which provides additional resonances and improves the input impedance matching, thus, wideband performance can be obtained. In addition, cause of the loop structure, the current direction on the feed and shorting strip are the same, hence, the proposed antenna has stronger vertical polarization field with a low profile of 5 mm as compared to the conventional printed antenna in horizontal plane. Besides, the antenna performance affect by the operating environment, especially when metal bodies are nearby the antenna. The proposed antenna still maintains good radiation characteristics even while a metal plane is placed parallel under the antenna closely. That is because of the current direction between the antenna and the image current on the metal plane has the same direction.

Finally, in Chapter 5, another miniaturized antenna design for high integration module application, an on-package PIFA, consisting of a single folded metal plate for WLAN applications is proposed. Fabricating an antenna directly on the package has the advantage of reducing feeder loss and the overall size of the circuitry. The shielding package can perform as part of the ground plane and block to eliminate the undesired coupling with nearby RF components. From the analysis results of the coupling between the antenna and the RF component embedded inside the package, it had been found that high isolation can be obtained, especially when the components are placed away from the antenna input. And the antenna performance is rarely changed and the isolation between the antenna and the RF components can be maximized by appropriately locating the components in the package. Moreover, an on-package PIFA integrated with a WLAN FEM and a WLAN card containing the baseband/MAC circuitry was successfully implemented. The EVM in the operating band is better than -30 dB, indicating the good performance of the architecture. From the evaluated result, it seems that the on-package PIFA has good radiation characteristic and thus suitable for the WLAN communication applications. The prototype has a compact size of 15 mm × 20 mm × 3.5 mm.

6.2 Suggestions for Future Works

Several antennas of the miniaturized antenna design had been proposed and implemented in this dissertation. These antennas have the merits of simple in geometry, easy for manufacture and integration, low-cost, and exhibit a good impedance matching in addition to having stable radiation patterns over the bandwidths. However, there are still some characteristics can be improved further.

In Chapter 2, a parallel LC circuit is utilized for achieving the band-notch function of the UWB antenna, which is the different method presented in [46]-[67]. But, in the view of filter characteristics, the sharper rejection curve can provided more excellent band-notch performance. Hence, the design of the band-notch function with the shape curve of the ideal filter property could be improved in the future.

In Chapter 3, a quasi-transmission line section is introduced and because of its different function varied with frequency, the wideband performance can be obtained. But, for the full band UWB of 3.1 to 10.6 GHz application, the fractional bandwidth is slightly insufficient. Hence, the future work is how to expand the bandwidth and then to be suitable for the full band communications.

In Chapter 5, an SOP antenna design is proposed. Fabricating an antenna directly on the package has the advantage of reducing feeder loss and the overall size of the circuitry. Thus, by utilizing this integration technology on other communication system application of the antenna design, it is an effective method to achieve the miniaturization results.

References

[1] J. M. Wilson, “Ultra-wideband/a disruptive RF technology?” *Intel Research & Development*, pp. 1-8, Sept. 2002. http://www.intel.com/technology/comms/uwb/download/Ultra-Wideband_Technology.pdf.

[2] *First Report and Order, Revision of Part 15 of the Commission’s Rule Regarding Ultra Wideband Transmission Systems*, Fed. Commun. Comm., FCC 02-48, Apr. 22, 2002.

[3] Batra et al., “Multi-band OFDM physical layer proposal for IEEE 802.15 task group 3a”, *IEEE Document number 802.15-04-0493r1*, Sep. 2003.

[4] R. Kohno, M. McLaughlin, and M. Welborn, “DS-UWB physical layer submission to 802.15 task group 3a”, *IEEE Document number 802.15-04-0137r4.*, Jan. 2005.

[5] Y. F. Ruan, V. X. Guo, K. W. Khoo, and X. Q. Shi, “Compact wideband antenna for wireless communications,” *IET Microw. Antennas Propag.*, vol. 1, no. 3, pp. 556-560, June 2007.

[6] C. Y. Huang and P. Y. Chiu, “Dual-band monopole antenna with shorted parasitic element,” *Electron. Lett.*, vol. 41, no. 21, pp. 1154-1155, Oct. 2005.

[7] K. Seol, J. Jung, and J. Choi, “Multi-band monopole antenna with inverted U-shaped parasitic plane,” *Electron. Lett.*, vol. 42, no. 15, pp. 844-845, July 2006.

[8] K. Chung, T. Yun, and J. Choi, “Wideband CPW-fed monopole antenna with parasitic elements and slots,” *Electron. Lett.*, vol. 40, no. 17, pp. 1038-1040, Aug. 2004.

[9] E. Antonino-Daviu, M. Cabedo-Fabres, M. Ferrando-Bataller, and A. Valero-Nogueira, “A discussion on the feed configuration of planar monopole antennas to obtain ultra wide band performance,” in *Proc. IEEE AP-S Int. Symp.*, June 2004, vol. 2, pp. 21867-1870.

[10] E. Antonino-Daviu, M. Cabedo-Fabres, M. Ferrando-Bataller, and A. Valero-Nogueir, “Wideband double-fed planar monopole antennas,” *Electron. Lett.*, vol. 39, no. 23, pp. 1635-1636, Nov. 2003.

[11] K. L. Wong, C. H. Wu, and S. W. Su, “Ultrawide-band square planar metal-plate monopole antenna with a trident-shaped feeding strip,” *IEEE Trans. Antennas Propag.*, vol. 53, no. 4, pp. 1262–1269, Apr. 2005.

[12] Q. Wu, R. Jin, J. Geng, and M. Ding, “Printed Omni-Directional UWB Monopole Antenna With Very Compact Size,” *IEEE Trans. Antennas Propag.*, vol. 56, no. 3, pp. 896-899, Mar. 2008.

[13] T. Yang and W. A. Davis, “Planar half-disk antenna structures for ultra-wideband communications,” in *Proc. IEEE AP-S Int. Symp.*, Jun. 2004, vol. 3, pp. 2508-2511.

[14] T. Yang and W. A. Davis, “Wearable ultra-wideband half-disk antennas,” in *Proc. IEEE AP-S Int. Symp.*, Jul. 2005, vol. 3A, pp. 500-503.

[15] J. Liang, C. C. Chiau, X. Chen, and C. G. Parini, “Printed circular disc monopole antenna for ultra-wideband applications”, *Electron. Lett.*, no. 26, vol. 40, pp. 1246-1247, Sep. 2004.

[16] M. Hammoud, P. Poey, and F. Colombel, “Matching the input impedance of a broadband disc monopole,” *Electron. Lett.*, vol. 29, pp. 406-407, Feb. 1993.

[17] N. P. Agrawall, G. Kumar, and K. P. Ray, “Wide-band planar monopole antennas,” *IEEE Trans. Antennas Propag.*, vol. 46, no. 2, pp. 294-295, Feb. 1998.

[18] C. Y. Huang and W. C. Hsia, “Planar elliptical antenna for ultra-wideband communications”, *Electron. Lett.*, vol. 41, no. 6, pp. 296-297, Mar. 2005.

[19] W. C. Liu and P. C. Kao, “CPW-fed triangular monopole antenna for ultra-wideband operation,” *Microwave Opt. Technol. Lett.*, vol. 47, no. 6, pp 580-582, Dec. 2005.

[20] C. C. Lin, Y. C. Kan, L. C. Kuo, and H. R. Chuang, “A planar triangular monopole antenna for UWB communication,” *IEEE Microwave Wireless Compon. Lett.*, vol. 15, no. 10, pp. 624-626, Oct. 2005.

[21] J. R. Verbiest and G. A. E. Vandenbosch, “Small-size planar triangular monopole antenna for UWB WBAN applications,” *Electron. Lett.*, vol. 42, no. 10, pp. 566-567, May 2006.

[22] M. J. Ammann, “Square planar monopole antenna,” in *Proc. IEE Antenna Propag. Nat. Conf.*, Mar. 1999, pp.37-40.

[23] P. V. Anob, K. P. Ray, and G. Kumar, “Wideband orthogonal square monopole antennas with semi-circular base,” in *Proc. IEEE AP-S Int. Symp.*, Jul. 2001, vol. 3, pp. 294-297.

[24] M. J. Ammann and Z. N. Chen, “A wide-band shorted planar monopole with bevel,” *IEEE Trans. Antennas Propag.*, vol. 51, no. 4, pp. 901-903, Apr. 2003.

[25] M. J. Ammann and Z.-N. Chen, “Wideband monopole antennas for multi-band wireless systems”, *IEEE Antennas Propag. Mag.*, vol. 45, no. 2, pp. 146-150, April 2003.

[26] K. Y. Yazdandoost and R. Kohno, “Bow-tie antenna for UWB communication frequency,” in *Proc. IEEE AP-S Int. Symp.*, June 2004, vol. 3, pp. 2520-2523.

[27] K. Kiminami, A. Hirata, and T. Shiozawa, “Double-sided printed bow-tie antenna for UWB communications,” *IEEE Antennas Wireless Propag. Lett.*, vol. 3, no.1, pp. 152-153, 2004.

[28] T. Karacolak and E. Topsakal, “A double-sided rounded bow-tie antenna (DSRBA) for UWB communication,” *IEEE Antennas Wireless Propag. Lett.*, vol. 5, no.1, pp. 446-449, Dec. 2006.

[29] D. H. Kwon and Y. Kim, “CPW-fed planar ultra-wideband antenna with hexagonal radiating elements,” in *Proc. IEEE AP-S Int. Symp.*, Jun. 2004, vol. 3, pp. 2947-2950.

[30] Z. N. Low, J. H. Cheong, and C. L. Law, “Low-cost PCB antenna for UWB applications,” *IEEE Antennas Wireless Propag. Lett.*, vol. 4, pp. 237-239, 2005.

[31] S. K. Padhi, S. Zagriatski, S. Crozier, and M. E. Bialkowski, “Planar ring monopole antennas for ultra-wideband applications”, *IEEE Int. Workshop on Antenna Technol.: Small Antennas and Novel Metamaterials*, pp. 333-336, Mar. 2005.

[32] J. Liang, C. C. Chiau, X. Chen, and C. G. Parini, “Printed circular ring monopole antenna,” *Microwave Opt. Technol. Lett.*, vol. 45, pp. 372-375, Sep. 2005.

[33] S. Y. Suh, W. L. Stutzman, W. A. Davis, “A new ultra wideband printed monopole antenna: the planar inverted cone antenna (PICA)”, *IEEE Trans. Antennas Propag.*, vol. 52, no. 5, pp. 1361-1364, May 2004.

[34] C. W. Ling, W. H. Lo, R. H. Yan, and S. J. Chung, “Planar binomial curved monopole antennas for ultrawideband communication,” *IEEE Trans. Antennas Propag.*, vol. 55, no. 9, pp. 2622-2624, Sept. 2007.

[35] C. Y. Hong, C. W. Ling, I. Y. Tarn, and S. J. Chung, “Design of a planar ultra-wideband antenna with a new band-notch structure,” *IEEE Trans. Antennas Propag.*, vol. 55, no. 12, pp. 3391-3397, Dec. 2007.

[36] J. Y. Sze and K. L. Wong, “Bandwidth enhancement of a microstrip-line-fed printed wide-slot antenna,” *IEEE Trans. Antennas Propagat.*, vol. 49, no. 7, pp. 1020-1024, Jul. 2001.

[37] X. Qing, M. Y. W. Chia, and X. Wu, “Wide-slot antenna for UWB Applications,” in *Proc. IEEE AP-S Int. Symp.*, Jun. 2003, vol. 1, pp. 834-837.

[38] R. Chair, A. A. Kishk, and K. F. Lee, “Ultrawide-band coplanar waveguide-fed rectangular slot antenna,” *IEEE Antennas Wireless Propagat. Lett.*, vol. 3, no. 1, pp 227-229, 2004.

[39] S. H. Hsu and K. Chang, “Ultra-thin CPW-fed rectangular slot antenna for UWB applications,” in *Proc. IEEE AP-S Int. Symp.*, Jul. 2006, pp. 2587-2590.

[40] H. D. Chen, “Broadband CPW-fed square slot antenna with a widened tuning stub,” *IEEE Trans. Antennas Propagat.*, vol. 51, no.8, pp. 1982-1986, Aug. 2003.

[41] Y. Liu, K. L. Lau, and C. H. Chan, “Microstrip-fed wide slot antenna with wide operating bandwidth,” in *Proc. IEEE AP-S Int. Symp.*, Jun. 2004, vol. 3, pp. 2285-2288.

[42] Y. W. Jang, "A circular microstrip-fed single-layer single-slot antenna for multi-band mobile communications," *Microwave Opt. Technol. Lett.*, vol. 37, no. 1, pp. 59-62, Apr. 2003.

[43] K. Do-Hoon K. Yongjin, M. Hasegawa, and T. Shimamori, "A small ceramic chip antenna for ultra-wideband systems," *IEEE Int. Workshop on Ultra Wideband Systems*, May 2004, pp. 307-311.

[44] C. Y. Wu, C. L. Tang, and A. C. Chen, "UWB chip antenna design using LTCC multilayer technology for mobile applications," in *Proc. APMC*, Dec. 2005, 3 pp.

[45] G. Brzezina, L. Roy, and L. MacEachern, "Planar antennas in LTCC technology with transceiver integration capability for ultra-wideband applications," *IEEE Trans. Microw. Theory Techn.*, vol. 54, no.6, pp. 2830-2839, Jun. 2006.

[46] S. H. Choi, J. K. Park, S. K. Kim, and J. Y. Park, "A new ultra-wideband antenna for UWB applications," *Microwave Opt. Technol. Lett.*, vol. 40, no. 5, pp. 399-401, Mar. 2004.

[47] W. Choi, J. Jung, K. Chung and J. Choi, "Compact microstrip-fed antenna with band-stop characteristic for ultra-wideband applications," *Microwave Opt. Technol. Lett.*, vol. 47, no. 1, pp. 89-92, Oct. 2005.

[48] J. N. Lee and J. K. Park, "Impedance characteristics of trapezoidal ultra-wideband antennas with a notch function," *Microwave Opt. Technol. Lett.*, vol. 46, no. 5, pp. 503-506, Sep. 2005.

[49] C. Jaehoon, K. Chung and Y. Roh, "Parametric analysis of a band-rejection antenna for UWB application," *Microwave Opt. Technol. Lett.*, vol. 47, no. 3, pp. 287-290, Nov. 2005.

[50] H. K. Lee, J. K. Park, and J. N. Lee, "Design of a planar half-circle-shaped UWB notch antenna," *Microwave Opt. Technol. Lett.*, vol. 47, no. 1, pp. 9-11, Oct. 2005.

[51] Y. Kim and D. H. Kwon, "Planar ultra wide band slot antenna with frequency band notch function," in *Proc. IEEE AP-S Int. Symp.*, Jun. 2004, vol. 2, pp. 1788-1791.

[52] K. L. Wong, Y. W. Chi, C. M. Su, F. S. Chang, "Band-notched ultra-wideband circular-disk monopole antenna with an arc-shaped slot," *Microwave Opt. Technol. Lett.*, vol. 45, no. 3, pp. 188-191, May 2005.

[53] C. Y. Huang, W. C. Hsia, J. S. Kuo, "Planar ultra-wideband antenna with a band-notched characteristic," *Microwave Opt. Technol. Lett.*, vol. 48, no. 1, pp. 99-101, Jan. 2006.

[54] C. Y. Huang and W. C. Hsia, "Planar ultra-wideband antenna with a frequency notch characteristic," *Microwave Opt. Technol. Lett.*, vol. 49, no. 2, pp. 316-320, Feb. 2007.

[55] H. Yoon, H. Kim, K. Chang. Y. J. Yoon, and Y. H. Kim, "A study on the UWB antenna with band-rejection characteristic," in *Proc. IEEE AP-S Int. Symp.*, Jun. 2004, vol. 2, pp. 1784-1787.

[56] I. J. Yoon, H. Kim, K. Chang, Y. J. Yoon, and Y. H. Kim, “Ultra wideband tapered slot antenna with band-stop characteristic,” in *Proc. IEEE AP-S Int. Symp.*, Jun. 2004, vol. 2, pp. 1780-1783.

[57] S. Y. Suh, W. L. Stutzman, W. A. Davis, A. E. Waltho, K. W. Skeba, and J. L. Schiffer, “A UWB antenna with a stop-band notch in the 5-GHz WLAN band,” in *Proc. IEEE ACES Int. Conf.*, Apr. 2005, pp. 203-207.

[58] Y. Gao, B.L. Ooi, and A.P. Popov, “Band-notched ultra-wideband ring-monopole antenna,” *Microwave Opt. Technol. Lett.*, vol. 48, no. 1, pp. 125-126, Jan. 2006.

[59] J. Kim, C. S. Cho and J. W. Lee, “5.2 GHz notched ultra-wideband antenna using slot-type SRR,” *Electronics Lett.*, vol. 42, no. 6, pp. 315-316, Mar. 2006.

[60] L. Liu, Y. Z. Yin, C. Jie, J. P. Xiong, and Z. Cui, “A compact printed antenna using slot-type CSRR for 5.2 GHz/5.8 GHz band-notched UWB application,” *Microwave. Opt. Technol. Lett.*, vol. 50, no. 12, pp. 3239-3242, Dec. 2008.

[61] K.H. Kim, Y.J. Cho, S.H. Hwang, and S.O. Park, “Band-notched UWB planar monopole antenna with two parasitic patches,” *Electronics Lett.*, vol. 41, no. 14, pp. 783-785, Jul. 2005.

[62] S. H. Lee, J. W. Baik and Y. S. Kim, “A coplanar waveguide fed monopole ultra-wideband antenna having band-notched frequency function by two folded-striplines,” *Microwave. Opt. Technol. Lett.*, vol. 49, no. 11, pp. 2747-2750, Nov. 2007.

[63] S. J. Kim, H. S. Lee and Y.S. Kim, “A CPW-fed staircase monopole UWB antenna with band-notched frequency in the WLAN band,” *Microwave. Opt. Technol. Lett.*, vol. 49, no. 10, pp. 2545-2547, Oct. 2007.

[64] W. J. Lui, C. H. Cheng, and H. B. Zhu, “Frequency notched printed slot antenna with parasitic open-circuit stub,” *Electronics Lett.*, vol. 41, no. 20, pp. 1094-1095, Sep. 2005.

[65] D. H. Kwon Y. Kim and N. P. Chubinsky, “A printed dipole UWB antenna with GPS frequency notch function,” in *Proc. IEEE AP-S Int. Symp.*, Jul. 2005, vol. 3A, pp. 520-523.

[66] C. H. Luo, C. M. Lee, W. S. Chen, C. H. Tu, and Y. Z. Juang, “Dual band-notched ultra-wideband monopole antenna with an annular CPW-feeding structure,” *Microwave Opt. Technol. Lett.*, vol. 49, no. 10, pp. 2376-2379, Oct. 2007.

[67] Y. Ding, G. M. Wang, and J. G. Liang, “Compact band-notched ultra-wideband printed antenna,” *Microwave Opt. Technol. Lett.*, vol. 49, no. 11, pp. 2686-2689, Nov. 2007.

[68] L. Ukkonen, D. Engels, L. Sydanheimo, and M. Kivikoski, “Planar wire-type inverted-F RFID tag antenna mountable on metallic objects,” in *Proc. IEEE AP-S Int. Symp.*, Jun. 2004, vol. 1, pp. 101-104.

[69] S. Bovelli, F. Neubauer, and C. Heller, "Mount-on-metal RFID transponders for automatic identification of containers," *European Microwave Conf.*, Sept. 2006, pp. 726-728.

[70] C. C. Lin, L. C. Kuo, and H. R. Chuang, "A horizontally polarized omnidirectional printed antenna for WLAN applications," *IEEE Trans. Antennas Propagat.*, vol. 54, no.11, pp. 3551-3556, Nov. 2006.

[71] Y. Y. Wang and Shyh-Jong Chung, "A new dual-band antenna for WLAN applications," in *Proc. IEEE AP-S Int. Symp.*, Jun. 2004, vol. 3, pp. 2611-2614.

[72] M. N. Suma, P. C. Bybi, and P. Mohanan, "A wideband printed monopole antenna for 2.4-GHz WLAN applications," *Microwave Opt. Technol. Lett.*, vol. 48, no. 5, pp. 871-873, May 2006.

[73] C. M. Su, K. L. Wong, W. S. Chen, and Y. T. Cheng, "A microstrip-coupled printed inverted-f monopole antenna," *Microwave. Opt. Technol. Lett.*, vol. 43, no. 6, pp. 470-472, Dec. 2004

[74] A. V. Praveen Kumar, V. Hamsakutty, J. Yohannan, and K. T. Mathew, "Microstripline-fed half-cylindrical dielectric resonator antenna for 2.4-GHz WLAN application," *Microwave. Opt. Technol. Lett.*, vol. 48, no. 4, pp. 724-726, Apr. 2006.

[75] H. Park, K. Chung, and J. Choi, "Design of a planar inverted-F antenna with very wide impedance bandwidth," *IEEE Microwave Wireless Compon. Lett.*, vol. 16, no. 3, pp. 113-115, Mar. 2006.

[76] Y. B. Kwon, J. I. Moon, and S. O. Park, "An internal triple-band planar inverted-F antenna," *IEEE Antennas Wireless Propag. Lett.*, vol. 2, no. 1, pp.341-344, 2003.

[77] F. Wang, Z. Du, Q. Wang, and K. Gong, "Enhanced-bandwidth PIFA with T-shaped ground plane," *Electron. Lett.*, vol. 40, no. 23, pp. 1504-1505, Nov. 2004.

[78] M. Steyaert, M. Borremans, J. Janssens, B. Muer, I. Itoh, J. Craninckx, J. Crols, E. Morifuji, S. Momose, and W. Sansen, "A single-chip CMOS transceiver for DCS-1800 wireless communications," in *Proc. IEEE Int. Solid-State Circuits Conf.*, Feb. 1998, pp. 48-49.

[79] K. Lim, A. Obatoyinbo, M. Davis, J. Laskar, and R. Tummala, "Development of planar antennas in multi-layer packages for RF system-on-a-package applications," *Electrical Perform. Electron. Package*, pp. 101-104, Oct. 2001.

[80] Y. P. Zhang, "Finite-difference time-domain analysis of integrated ceramic ball grid array package antenna for highly integrated wireless transceivers," *IEEE Trans. Antennas Propagat.*, vol. 52, no. 2, pp. 435-442, Feb. 2004.

[81] Y. P. Zhang, "Integrated circuit co-fired laminated ceramic package antenna," in *Proc. IEEE Int. Solid-State and Integrated-Circuit Technol. Conf.*, Oct. 2001, vol. 1, pp. 101-103.

[82] Y. P. Zhang, "Integrated circuit ceramic ball grid array package antenna," *IEEE Trans. Antennas Propagat.*, vol. 52, no. 10, pp. 2538-2544, Oct. 2004.

[83] Y. P. Zhang, “Integration of microstrip antenna on cavity-down ceramic ball grid array package,” *Electron. Lett.*, vol. 38,no. 22, pp. 1307-1308, Oct. 2002.

[84] Y. P. Zhang, “Design of on-package microstrip antennas for single-chip wireless transceivers,” in *Proc. IEEE Electron. Packag. Technol. Conf.*, Dec. 2002, pp. 40-44.

[85] C. T. P. Song, P. S. Hall, and H. Ghafouri-Shiraz, “Novel RF front end antenna package,” in *IEE Proc. Microw. Antennas Propag.*, Aug. 2003, vol. 150, pp. 290-294.

[86] M. M. Tentzeris, J. Laskar, J. Papapolymerou, S. Pinel, V. Palazzari, R. Li, G. DeJean, N. Papageorgiou, D. Thompson, R. Bairavasubramanian, S. Sarkar, and J. H. Lee, “3-D-integrated RF and millimeter-wave functions and modules using liquid crystal polymer (LCP) system-onpackage technology,” *IEEE Trans. Adv. Packag.*, vol. 27, no. 2, pp.332-340, May 2004.

[87] C. H. Lee, A. Sutono, S. Han, K. Lim, S. Pinel, E. M. Tentzeris, and J. Laskar, “A compact LTCC-based Ku-band transmitter module,” *IEEE Trans. Adv. Packag.*, vol. 25, no. 3, pp. 374-384, Aug. 2002.

[88] L. R. Zheng, X. Duo, M. Shen, T. Torrika, W. Michielsen, H. Tenhunen, L. Chen, G. Zou, and J. Liu, “Design and implementation of system-on-package for radio and mixed-signal applications,” in *Proc. IEEE High Density Microsystem Design and Packaging and Component Failure Analysis Conf.*, Jun. 2004, pp. 97-104.

[89] T. Sudo, H. Sasaki, N. Masuda, and J. L. Drewniak, “Electromagnetic interference (EMI) of system-on-package (SOP),” *IEEE Trans. Adv. Packag.*, vol. 27, no. 2, pp. 304-314, May 2004.

[90] *EM simulation tool HFSS*. Pittsburgh, PA: Ansoft Corporation.

Appendix

Abbreviation	Full name
AFEM	Antenna embedded Front-end Module
AP	Access Point
BPF	Band-pass Filter
CBGA	Ceramic Ball Grid Array
DCS	Digital Communication System
DRA	Dielectric Resonator Antenna
DS-UWB	Direct Sequence Ultra-wideband
EM	Electromagnetic
EVM	Error Vector Magnitude
FCC	Federal Communications Commission
FEM	Front-end Module
GSM	Global System for Mobile Communication
LPF	Low-pass Filter
LTCC	Low Temperature Co-fired Ceramic
MAC	Medium Access Control
MB-OFDM	Multi-band Orthogonal Frequency Division Multiplexing
NLOS	Non-line of Sight
PA	Power Amplifier
PCMCIA	Personal Computer Memory Card International Association
PIFA	Planar Inverted-F Antenna
SOP	System-on-Package
SRR	Split Ring Resonator
SW	Switch
UMTS	Universal Mobile Telecommunication System
UWB	Ultra-wideband
WiBro	Wireless Broadband
WLAN	Wireless Local Area Network

Vita

Ching-Wei Ling was born on January 2, 1980, in Nantou, Taiwan, R.O.C. She received the B.S. and M.S. degrees in physics from the National Kaohsiung Normal University, Kaohsiung, Taiwan, in 2004. In the same year, she entered the Ph.D. program in Department of Communication Engineering at National Chiao Tung University, Hsinchu, Taiwan, R.O.C.. Her current research interests include UWB systems and microwave circuits.

Publication List

- Journal Papers:
  - [1] C. Y. Hong, **C. W. Ling**, I. Y. Tarn, and S. J. Chung, “Design of a planar ultra-wideband antenna with a new band-notch structure,” *IEEE Trans. Antennas Propagat.*, vol.55, no. 12, pp. 3391-3397, Dec. 2007.
  - [2] **C. W. Ling**, W. H. Lo, R. H. Yan, and S. J. Chung, “Planar binomial curved monopole antennas for ultra-wideband communication,” *IEEE Trans. Antennas Propagat.*, vol.55, no. 9, pp. 2622-2624, Sept. 2007.
  - [3] **C. W. Ling**, C. Y. Lee, C. L. Tang, and S. J. Chung, “Analysis and application of an on-package planar inverted-F antenna,” *IEEE Trans. Antennas Propagat.*, vol.55, no. 6, pp. 1774-1780, Jun. 2007.
  - [4] **C. W. Ling** and S. J. Chung, “A simple monopole-like printed ultra-wideband antenna with a quasi-transmission line section,” *IEEE Trans. Antennas Propagat.* (in revision)
  - [5] **C. W. Ling** and S. J. Chung, “Low-profile ultra-wideband antenna with strong vertical polarization field,” presubmitted to *IEEE Trans. Antennas Propagat.*

- Conference Papers:
  - [1] J. C. Ke, **C. W. Ling** and S. J. Chung, “Implementation of a multi-beam wwitched parasitic antenna for wireless applications,” in *Proc. 2007 IEEE AP-S Int'l. Symp.*, pp.3368-3371, June 9-15, 2007.
  - [2] S. C. Chen, Y. S. Wang, **C. W. Ling** and S. J. Chung, “A new high isolation dual-antennas with miniature decoupling network design,” in *Proc. 2007 IEEE AP-S Int'l. Symp.*, pp. 3125-31278, June 9-15, 2007.
  - [3] **C. W. Ling** and S. J. Chung, “An on-package planar inverted-F antenna for WLAN application,” *IASTED*, Banff, Canada, July 3-5, 2006.

- Patents:
  - [1] S. J. Chung, **C. W. Ling** and Y.C. Cheng, “Planar inverted-F antenna with extended grounding plane,” European Patent No. 08009288.5-2220, May 20, 2008.
  - [2] **C. W. Ling**, S. J. Chung, and W. H. Lo, “Monopole Antenna for ultra-wideband applications,” U.S. Pregrant Patent No. 20070194990, Aug. 23, 2007.